NASA Technical Memorandum 78746

(NASA-CR-78746) AERODYNAMIC CHARACTERISTICS INDUCED ON A SUPERCRITICAL WING DUE TO VECTORING TWIN NOZZLES AT MACH NUMBERS FROM 0.40 TO 0.95 (NASA) 115 p HC A06/MF A01 CSCL 01A G3/02

N78-30039

Unclas 28583

AERODYNAMIC CHARACTERISTICS INDUCED ON A SUPERCRITICAL WING DUE TO VECTORING TWIN NOZZLES AT MACH NUMBERS FROM 0.40 TO 0.95

FRANCIS J. CAPONE

AUGUST 1978

SEP 1978
RECEIVED
NASA STI FACILITY

NASA
National Aeronautics and Space Administration

Langley Research Center
Hampton, Virginia 23665

AERODYNAMIC CHARACTERISTICS INDUCED ON A SUPERCRITICAL WING DUE TO VECTORING TWIN NOZZLES AT MACH NUMBERS FROM 0.4 TO 0.95

Francis J. Capone
Langley Research Center

SUMMARY

An investigation has been conducted in the Langley 16-foot transonic tunnel to determine the induced lift characteristics of a vectored-thrust concept in which jet-exhaust nozzles were located in the fuselage at the wing trailing edge. The wing had a supercritical airfoil section. The investigation was conducted at Mach numbers from 0.4 to 0.95, angles of attack up to 14°, and thrust coefficients up to 0.35, and nozzle deflection angles of 0° and 30°. Separate force balances were used to determine both total aerodynamic and thrust forces and thrust forces alone which allowed for a direct measurement of jet turning angle at forward speeds. The Reynolds number per meter varied from 8.20×10^6 to 12.80×10^6.

The results of this investigation show the configuration with the supercritical wing to have generally better performance with respect to both lift augmentation and drag reduction than the same configuration with a 64 series airfoil.

INTRODUCTION

A number of studies have indicated that thrust-induced supercirculation effects from thrust vectoring have a potential for not only increasing maneuverability of fighter aircraft but also improving cruise performance (refs. 1 to 6). These studies used a vectorable partial-span rectangular jet-exhaust nozzle located at the wing trailing edge to induce lift due to supercirculation similar to a jet flap. The configuration of references 1 and 2 had a highly swept wing, whereas that of references 3 and 4 used a wing more representative of current fighter aircraft. Reference 3 summarized a parametric investigation that included studying the effects on induced lift

and drag of nozzle deflection angle, nozzle exit location, nozzle shape (rectangular or round), and wing camber. References 4 and 5 present detailed information concerning the effects of varying nozzle deflection angle, nozzle exit location and nozzle shape.

This report presents results from that portion of the investigation where the wing installed on the model had a supercritical airfoil section. The investigation was conducted in the Langley 16-foot transonic tunnel at Mach numbers from 0.4 to 0.95, angles of attack up to 14°, and thrust coefficients up to 0.35. The test Reynolds number per meter varied from 8.20×10^6 to 12.80×10^6.

SYMBOLS

Model forces and moments are referred to the axis system shown in figure 1 with the model moment reference center located at $0.25\bar{c}$, which corresponds to FS 117.64 cm. A discussion of the data reduction procedure and definitions of the aerodynamic force and moment terms used herein are given in the appendix. All aerodynamic coefficients are based on $q_\infty S$ or $q_\infty S\bar{c}$ except at static conditions where p_a is substituted for q_∞.

A_{base} total cross-sectional area at nozzle exit including vane and nozzle base area, 78.51 cm^2

A_{max} maximum cross-sectional area of afterbody, 284.78 cm^2

A_{seal} cross-sectional area enclosed by seal strip, 266.00 cm^2

AR wing aspect ratio, 3.0

C_A axial-force coefficient (see fig. 1 and appendix)

C_D drag coefficient (see fig. 1 and appendix)

$C_{D,i}$ induced drag coefficient (see eq. (A13))

$C_{D,min}$	jet-off minimum drag coefficient
$C_{(F-A)}$	thrust-minus-axial-force coefficient (see fig. 1)
$C_{(F-D)}$	thrust-minus-drag coefficient (see fig. 1)
$C_{F,j}$	nozzle thrust coefficient along tailpipe center line (fig. 1)
C_L	total lift coefficient (fig. 1)
$C_{L,j}$	jet lift coefficient (fig. 1)
$C_{L,o}$	jet-off lift coefficient
$C_{L,\Gamma}$	jet-induced supercirculation lift coefficient
ΔC_L	incremental lift coefficient, $C_{L,\Gamma} + C_{L,j}$
C_m	total pitching-moment coefficient (fig. 1)
$C_{m,j}$	jet pitching-moment coefficient (fig. 1)
C_N	normal-force coefficient (fig. 1)
$C_{N,j}$	jet normal-force coefficient
$C_{N,o}$	jet-off normal-force coefficient
$C_{N,\Gamma}$	jet-induced supercirculation normal-force coefficient
$C_{p,aft}$	afterbody pressure coefficient
C_T	gross thrust coefficient along jet axis (fig. 1)

$\bar{c}$	mean geometric chord, 32.28 cm
e	wing efficiency factor at jet-off conditions
F_A	axial force, N
$F_{A,mom}$	momentum tare force due to bellows, N
$F_{A,Mbal}$	axial force measured by main balance along main balance axis, N
$F_{A,Tbal}$	axial force measured by thrust balance along thrust-balance axis, N
F_J	thrust component along tailpipe or body axis, N
FS	fuselage station, cm
M	Mach number
$\dot{m}_i$	ideal mass-flow rate, kg/sec
$\dot{m}_p$	measured mass-flow rate, kg/sec
N_{Re}	Reynolds number per meter
p_a	ambient pressure, N/m^2
$\bar{p}_{es}$	average static pressure at external seal, N/m^2
$\bar{p}_i$	average internal static pressure, N/m^2

$P_{t,j}$	average jet total pressure, N/m^2
p_∞	free-stream static pressure, N/m^2
q_∞	free-stream dynamic pressure, N/m^2
S	wing reference area including projection to model center line, 2599.89 cm^2
T_{rec}	thrust recovery (eq. (A12), appendix A)
T_t	free-stream stagnation temperature, K
w	half-width of body, 11.43 cm
X	afterbody length (fig. 9), 24.82 cm
x,y	body ordinate, cm
α	angle of attack (fig. 1), deg
α_{jo}	jet-off angle of attack, deg
α_n	angle of attack of tailpipe center line (fig. 1), deg
δ	effective jet turning angle, deg
δ_d	design or nominal nozzle deflection angle, deg

APPARATUS AND PROCEDURE

Model

A sketch showing the external geometry of the model is presented in figure 2; photographs are shown in figure 3. The wing had a leading-edge sweep of 50°, streamwise supercritical airfoil sections, an aspect ratio of 3.0, taper ratio of 0.3, and a reference area of 2599.89 cm^2. The wing had no twist or dihedral. Airfoil coordinates are given in Table I.

The fuselage had rectangular cross sections with rounded corners and had an effective fineness ratio of 7.28. As shown in figure 4, the body lines were chosen to enclose the internal propulsion system and to fair into the afterbody enclosing the nozzles. The afterbody boattail angle was 12.5°. The maximum width and height of the body were 22.86 cm and 12.7 cm, respectively, and the maximum body cross-sectional area was 284.78 cm^2. Table II presents ordinates for both the fixed nonmetric forebody and the metric afterbody. A 0.16-cm annular gap between the forebody and afterbody was required to prevent fouling between the nonmetric and metric portions of the model. A flexible Teflon strip inserted into slots was used as a seal to prevent internal flow in the model. (See fig. 4) The low coefficient of friction of Teflon minimized restraint between the metric and nonmetric portions of the model. Only that portion of the configuration aft of the metric break at fuselage station 99.06 cm was supported by the main-force balance and hereafter is referred to as the wind-tunnel model.

Twin-Jet Propulsion Simulation System and Exhaust Nozzles

Sketches of the twin-jet propulsion simulation system are presented in figures 4(a) and 4(b); photographs without the force balances are shown in figure 4(c). The propulsion system internal performance characteristics are presented in reference 4.

An external high-pressure air system provides a continuous flow of clean, dry air at a controlled temperature of about 306 K. This high-pressure air is brought through the support strut by six tubes into a high-pressure chamber. (See fig. 4(a).) Here the air is divided into two separate flows and is

passed through flow-control valves. These manually operated valves are used to balance the exhaust nozzle total pressure in each duct. As shown in figure 4(a) the air in each supply pipe is then discharged perpendicularly to the model axis through eight sonic nozzles equally spaced around the supply pipe. This method is designed to eliminate any transfer of axial momentum as the air is passed from the nonmetric to metric portion of the model. Two flexible metal bellows are used as seals and serve to compensate for the axial forces caused by pressurization. The cavity between the supply pipe and bellows is vented to the model internal pressure. The tailpipes are connected to the thrust balance, whose loads are then transmitted to the main balance through the wing and thrust-balance support block. (See fig. 4(a).)

The air is then passed through the tailpipes to the exhaust nozzles as shown in figure 5. A transition section, located between fuselage stations 122.44 cm and 124.97 cm, was used to transform the exhaust flow from axisymmetric to two dimensional. The nozzle internal cross-sectional area was held constant from fuselage stations 126.75 cm to 134.62 cm. Two sets of nozzles, each with a total exit area of 50.32 cm^2 at fuselage station 138.62 cm, were investigated with design turning angles of 0° and 30° as defined by δ_d in figure 5. The aspect ratio of the twin nozzles was 5.99; the nozzle aspect ratio is defined as the maximum nozzle width divided by the maximum depth including vanes. Nozzle mass-flow and static force and moment characteristics are shown in figures 6 and 7, respectively. The variation of measured thrust coefficient with nozzle pressure ratio is given in figure 8.

Thrust vectoring was obtained by using circular-arc turning vanes located in the nozzle exhaust flow. These turning vanes were arranged so that they would be completely washed by the jet flow in order to minimize the influence of the external flow on vectored nozzle performance.

Wind Tunnel and Support System

This investigation was conducted in the Langley 16-foot transonic tunnel, which is a single-return atmospheric wind tunnel with a slotted octagonal test section and continuous air exchange. The wind tunnel has continuously

variable airspeed up to a Mach number of 1.30. A complete description of the wind tunnel and operating characteristics can be found in reference 7.

The model was supported by a sting strut with the model center of rotation indicated in figure 2. The strut had a 45° leading-edge sweep, a 50.8-cm chord, and a 5-percent-thick hexagonal airfoil in the streamwise direction. The model blockage ratio was 0.0015 (ratio of model cross-sectional area to test-section area), and the maximum blockage ratio including the support system was 0.0020. Strut interference effects were considered to be small on this model afterbody because the boattail angle was 12.5°. Reference 8 indicates that strut interference may be large for models with boattail angles in excess of 15°, depending on the proximity to the strut trailing edge.

Instrumentation

External aerodynamic and internal nozzle forces and moments were each measured by internal, six-component strain-gage balances (fig. 4(a)). Eight external static pressures were measured at the sealed gap at approximately fuselage station 100.00 cm as shown in figure 9. Four of these pressure orifices were located on the nonmetric forebody and four were located on the metric afterbody at meridian angles of every 90°. These pressure measurements were used to correct the measured axial forces for pressure-area force tares as described in appendix A. Four internal pressures were measured in the vicinity of the sealed gap, and four internal pressures were located on the top and bottom of the nozzles approximately at fuselage station 125.00 cm. The internal pressures are also used for determining pressure area force tares. One internal pressure measurement was made near the nose of the model.

A turbine flowmeter (external to the wind tunnel) was used to measure the total mass-flow rate to the nozzles. In addition, the pressure and temperature in each supply pipe were measured prior to the discharge of the flow through the eight sonic nozzles; the measurements determined the mass-flow rate to each nozzle. These flow measurements were used independently to check the measurement determined by the flowmeter. Two total pressures and one total temperature were measured at one axial location

in each nozzle. These measurements were made at fuselage station 133.50 cm or 5.8 cm forward of the nozzle exit. All pressures were measured with individual pressure transducers. Temperatures were measured with iron-constantan thermocouples.

At each test condition, approximately 10 samples of data were recorded on magnetic tape over a period of about 10 seconds. The average of the 10 samples is used for computational purposes.

Tests

Two nozzles with geometric turning angles δ_d of 0° and 30° were tested at Mach numbers from 0 to 0.95 and at angles of attack from -2° to 14°. The average Reynolds number per meter, the free-stream dynamic pressure, and the stagnation temperature are summarized in the following table:

M	N_{Re} per meter	q_∞ kN/m^2	T_t, K
0.40	8.20×10^6	10.14	302.6
.70	11.68	24.96	316.5
.80	12.30	29.78	323.1
.90	12 63	33.92	328 7
.95	12.80	35.71	331.5

Balance load limits on the pitching moment restricted the maximum angle of attack at high Mach numbers; the maximum obtainable jet pressure ratio for the nozzles with the larger deflection angles was also restricted.

All tests were conducted with 0.25-cm-wide boundary-layer transition strips consisting of No. 100 silicon carbide grit sparsely distributed in a thin film of lacquer. In accordance with the recommendations of references 9

and 10, these strips were located 2.54 cm from the tip of the forebody nose and on both the upper and lower surfaces of the wings at 5 percent of the wing chord at the wing-fuselage juncture to 10 percent of the local streamwise chord at the wing tip.

PRESENTATION OF RESULTS

The results of this investigation are presented with limited discussion in plotted coefficient form in the following figures.

	Figure
Basic aerodynamic characteristics:	
$\delta_d = 0^\circ$	10
$\delta_d = 30^\circ$	11
Basic nozzle thrust characteristics:	
$\delta_d = 0^\circ$	12
$\delta_d = 30^\circ$	13
Afterbody pressure distributions:	
$\delta_d = 0^\circ$	14
$\delta_d = 30^\circ$	15
Jet lift and induced lift:	
$\delta_d = 0^\circ$	16
$\delta_d = 30^\circ$	17
Lift-augmentation factors:	
$\delta_d = 30^\circ$	18
Drag and aerodynamic lift characteristics:	
$\delta_d = 0^\circ$	19
$\delta_d = 30^\circ$	20
Drag polars	21
Thrust recovery characteristics:	
$\delta_d = 0^\circ$	22
$\delta_d = 30^\circ$	23

	Figure
Summary of incremental lift characteristics	24
Gross thrust coefficient characteristics	25
Summary of incremental drag characteristics	26
Summary of thrust recovery characteristics	27

DISCUSSION OF RESULTS

Thrust-induced supercirculation effects from thrust vectoring have indicated a potential for not only increasing maneuverability of fighter aircraft but also improving cruise performance. References 3 and 4 indicated that significant increases in thrust-induced lift along with substantial decreases in drag were achieved by thrust vectoring. Since the results shown herein are similar to those detailed in reference 4, only a brief discussion is presented.

Lift Characteristics

The incremental lift characteristics of the present investigations are compared to those of references 3 and 4 in figure 24. Incremental lift ΔC_L is shown as a function of Mach number (at scheduled pressure ratio) for the 30° nozzle and $\alpha = 0^\circ$. There is little or no effect of airfoil shape up to $M = 0.80$. Maximum lift gain factor for the supercritical wing was about 4.2 and occurred at $M = 0.95$. Scheduled nozzle pressure ratio varies from 1.5 at $M = 0.4$ to 3.5 at $M = 0.95$ and is shown in figure 25.

One effect of the interaction of the deflected jet with the wing flow field is illustrated at $M = 0.90$ by the insert on figure 24. Here, the variation of incremental lift with thrust coefficient for the 30° nozzle at $\alpha = 0^\circ$ is shown for the three wings. As thrust coefficient is increased, there is a sharp increase in incremental lift for the model with the 64A006 wing. A detailed comparison of afterbody pressure distributions shows an abrupt rearward movement of the wing shock wave occurring for the 64A006 wing at thrust coefficient near 0.15. It is felt that with the rearward shock movement, a smaller region of the wing is affected by flow separation and hence more lift is generated.

Drag and Thrust Recovery

Variation of incremental drag coefficient ΔC_D with lift coefficient for the three wings at M = 0.70 is shown in figure 26. Of the three wings, the supercritical showed the greatest drag reduction. This drag reduction may be a result of lower drag-due-to-lift for the supercritical wing with the 30° nozzle.

This reduction in drag-due-to-lift for the supercritical wing is probably also a result of improved leading-edge suction and may be occurring at a lower nozzle deflection angle because of the basic difference in the type of flow over the top of the airfoil. With the region of accelerated flow over the top reduced because of the flatness of the airfoil, it is now possible for the deflected jet to influence flow completely around the supercritical airfoil.

The variation of drag coefficient with Mach number at constant lift coefficient for the scheduled pressure ratio is also shown in figure 26. The poorer drag rise characteristics for the 64A406 wing may be attributed to a higher afterbody drag than for the other airfoils in combination with the afterbody.

Thrust recovery characteristics for the three wings are summarized in figure 27 at $\alpha + \delta = 30^\circ$ at the scheduled pressure ratio. In general, thrust recovery increases with increasing Mach number and the thrust recovery characteristics of the supercritical wing are better than the 64 series airfoils.

CONCLUDING REMARKS

An investigation has been conducted in the Langley 16-foot transonic tunnel to determine the induced lift characteristics of a vectored-thrust concept in which jet-exhaust nozzles were located in the fuselage at the wing trailing edge. The wing had a supercritical airfoil section. The investigation was conducted at Mach numbers from 0.4 to 0.95, angles of attack up to 14°, and thrust coefficients up to 0.35, and nozzle deflection angles of 0° and 30°. Separate force balances were used to determine both total aerodynamic and thrust forces and thrust forces alone which allowed

for a direct measurement of jet turning angle at forward speeds. The Reynolds number per meter varied from 8.20×10^6 to 12.80×10^6.

The results of this investigation show the configuration with the supercritical wing to generally have better performance with respect to both lift augmentation and drag reduction than the same configuration with a 64 series airfoil.

APPENDIX A

DATA REDUCTION PROCEDURE

Data Adjustments

External aerodynamic and internal nozzle forces and moments were each measured by separate internal six-component force balances as shown in figure 4. The main balance measured total lift, thrust-minus-axial force, and total pitching moment; the thrust balance sensed nozzle normal and axial forces and pitching moment. The center lines of these two force balances were located above and below the tailpipe center line (fig. 4(a)) and the bellows flow-transfer system (fig. 4(b)). Because of this offset, an interaction of loading one balance on the other existed; this interaction is primarily the result of the main balance acting on the thrust balance.

Consequently, single and combined loadings of the normal force and the pitching moment were made with and without the jets operating with the 0° nozzle. These calibrations were performed with the jets operating because this condition gave a more realistic effect of pressurizing the bellows rather than capping off the nozzles and pressurizing the flow system. Thus, in addition to the usual balance interaction corrections that are applied for a single force balance under combined loads, another set of corrections was made to the data from this investigation for the combined loading effects of one balance on the other. However, loadings were also made in the axial-force direction with the flow system capped off and pressurized; these loadings indicated no effect on the axial force measured by each balance.

In order to achieve desired thrust-minus-axial force (from main balance) and thrust (from thrust balance), the axial forces measured by both force balances must also be corrected for pressure-area tare forces acting on the model and for momentum tare forces caused by flow in the bellows. The external seal and internal pressure forces on the model were obtained by multiplying the difference between the average pressure (external seal or internal pressures shown in fig. 9) and free-stream static pressure by the affected projected area normal to the model axis. The momentum tare force was determined from calibrations prior to the wind-tunnel investigation

using standard calibration nozzles (ref. 4).

Gross thrust-minus-axial force was computed from the main balance axial force from the following relationship:

$$F_j - F_A = F_{A,Mbal} + (\bar{p}_{es} - p_\infty)(A_{max} - A_{seal}) + (\bar{p}_i - p_\infty)A_{seal} - F_{A,mom} \tag{A1}$$

where $F_{A,Mbal}$ (positive upstream) includes all pressure and viscous forces, internal and external, on both the afterbody and thrust system. The second and third terms account for the forward seal rim and interior pressure forces, respectively. In terms of an axial-force coefficient, the second term ranges from -0.0001 to -0.0007 and the third term varies ±0.0075 depending upon Mach number and pressure ratio. It was previously stated that internal pressure at any given set of test conditions was uniform throughout the inside of the model, thus indicating no flow. The fourth term is caused by the momentum tare correction and is a function of the average bellows internal pressure. At an internal pressure of 1380 kN/m^2 (corresponding to $p_{t,j}/p_\infty \approx 4.0$ at static conditions), this tare is approximately 5 percent of the maximum static thrust and its repeatability is 0.25 percent.

Gross thrust from the thrust balance is computed from a similar relationship:

$$F_j = F_{A,Tbal} - (\bar{p}_i - p_\infty)A_{base} - F_{A,mom} \tag{A2}$$

where $F_{A,Tbal}$ (positive upstream) includes nozzle thrust and the internal pressure forces acting on the thrust system.

Since both balances are offset from the model center line, similar adjustments are made to the pitching moments measured by both balances. These adjustments are necessary because both the pressure area and bellows momentum tare forces are assumed to act along the model center line. The pitching-moment tare is determined by multiplying the tare force by the appropriate moment arm and subtracting the value from the measured pitching moments.

APPENDIX A

External Forces Including Thrust

The adjusted forces and moments measured by the main balance are transferred from the main-balance axis to the body axis of the metric portion of the model where the body axis lies in the wing chord plane (fig. 1). Angle of attack α, which is the angle between the wing chord plane and the relative wind, was determined by applying deflection terms caused by model and balance bending under aerodynamic load to the sting pitch angle. Calibrations were made with the propulsion simulation system in place in order to account for any restraints that might occur across the force balances. It should also be noted that some difference in angle between the nonmetric and metric portions of the model exists because of balance deflection. No adjustment has been made for wind-tunnel flow angularity which is approximately 0.1° for most sting-supported models in the 16-foot transonic tunnel.

The total force and moment coefficients, including thrust about the body and stability axis, are shown in figure 1 where the moment reference center is at the quarter chord of the wing mean geometric chord (fuselage station 117.64 cm).

Nozzle Internal Forces

The adjusted forces and moments measured by the thrust balance are transferred from the thrust-balance axis to the parallel tailpipe center-line axis (fig. 1). The tailpipe center line will be at some angle with respect to the body axis because the thrust balance deflects, under load, relative to the body axis. Accordingly, α_n is defined as the angle between the tailpipe center line and the relative wind. This angle was determined by adding deflection terms to the previously determined value of angle of attack. Calibrations with the propulsion system in place were made in order to determine these deflection constants.

From the measured axial and normal components of the jet resultant thrust, the effective jet turning angle, thrust coefficient, and jet lift coefficient are defined, respectively, as

$$\delta = \tan^{-1} \frac{C_{N,J}}{C_{F,J}} \tag{A3}$$

$$C_T = \sqrt{C_{N,J}^{\ 2} + C_{F,J}^{\ 2}} \tag{A4}$$

$$C_{L,J} = C_T \sin (\delta + \alpha_n) = C_{N,J} \cos \alpha_n + C_{F,J} \sin \alpha_n \tag{A5}$$

Thrust Removal

Nozzle internal forces are transferred from the tailpipe center-line axis to the body axis and then subtracted from the external forces resulting in the following aerodynamic loads:

$$C_{N,o} + C_{N,\Gamma} = C_N - \left[C_{N,J} \cos (\alpha - \alpha_n) - C_{F,J} \sin (\alpha - \alpha_n)\right] \tag{A6}$$

$$C_A = -C_{(F-A)} + \left[C_{F,J} \cos (\alpha - \alpha_n) + C_{N,J} \sin (\alpha - \alpha_n)\right] \tag{A7}$$

and transferring to the wind axis

$$C_{L,o} + C_{L,\Gamma} = (C_{N,o} + C_{N,\Gamma}) \cos \alpha - C_A \sin \alpha \tag{A8}$$

$$C_D = C_A \cos \alpha + (C_{N,o} + C_{N,\Gamma}) \sin \alpha \tag{A9}$$

where the normal force or lift coefficient with the subscript o refers to jet-off values and the subscript Γ refers to the jet-on normal or lift force induced as a result of supercirculation on the wing. The quantity $C_{L,o} + C_{L,\Gamma}$ represents the total aerodynamic lift of the wings.

Lift Augmentation

Generally, the total lift component is broken down into three parts. (1) jet-off lift, (2) jet-reaction lift, and (3) jet-induced supercirculation lift. A gain factor is then defined as the ratio of supercirculation lift plus jet lift to the jet lift. Jet lift (not measured at forward speeds) is

then defined as $C_{T,i} \sin(\alpha + \delta_{static})$ where $C_{T,i}$ is an ideal thrust coefficient determined by measuring the total flow momentum at the nozzle exit (typical of two-dimensional tests). Other experimental setups usually have a single force balance and, thus, are only able to measure thrust and turning angle at static conditions. In this case, values of thrust coefficient at forward speeds can be determined based on these static thrust measurements. Since one of the purposes of the present investigation was to determine the components of the total lift, jet lift is measured directly with the thrust balance. However, first it was necessary to determine the jet-off or basic wing lift coefficient $C_{L,o}$. The basic wing lift varies with thrust coefficient and is different at each jet-on point since the model angle of attack is decreased with jet operation because of balance deflections. Figures 10 and 11 show the variation of α with C_T. Therefore, in order to determine $C_{L,o}$, the average jet-off lift variation with angle of attack at each Mach number was fitted to a third-order polynomial curve as a function of angle of attack; $C_{L,o}$ was then computed at each power-on point for the particular model angle of attack measured.

Incremental lift is then defined as

$$\Delta C_L = C_L - C_{L,o} = C_{L,\Gamma} + C_{L,j} \tag{A10}$$

and the lift-augmentation factor based on measured jet lift is simply

$$\frac{\Delta C_L}{C_{L,j}} = \frac{C_{L,\Gamma} + C_{L,j}}{C_{L,j}} \tag{A11}$$

Thrust Recovery

Thrust recovery has been defined as that portion of the total gross thrust, C_T recovered in the streamwise direction or as the amount of propulsive gross thrust converted to aerodynamic thrust (ref. 4) and is given as

$$T_{rec} = \frac{C_{D,min} + C_{D,i} + C_{(F-D)}}{C_T} \tag{A12}$$

where T_{rec} is a thrust ratio. The average jet-off minimum drag coefficient $C_{D,min}$ is determined by averaging the data for all the nozzles. The induced drag coefficient $C_{D,i}$ for a jet-flap airfoil is

$$C_{D,i} = \frac{C_{L,o} + C_{L,\Gamma}{}^{2}}{e\pi AR + 2C_T} \tag{A13}$$

where only the wing efficiency factor e determined at jet-off conditions is used to account for nonelliptic loading effects. Another efficiency factor can be applied to the entire denominator to account for jet effects; however, its value is not known.

In terms of the propulsive and aerodynamic thrust terms, thrust recovery is

$$T_{rec} = \frac{C_T \cos(\alpha + \delta) + C_{\Delta F}}{C_T} \tag{A14}$$

where $C_{\Delta F}$ is the aerodynamic thrust coefficient and represents the change in drag from the ideal jet-off drag polar. For zero thrust recovery, $C_{\Delta F} = 0$, and then

$$T_{rec} = \cos\ (\alpha + \delta) \tag{A15}$$

For complete thrust recovery, $T_{rec} = 1$ and then

$$C_{\Delta F} = C_T[1 - \cos\ (\alpha + \delta)] \tag{A16}$$

The aerodynamic thrust term can also be expressed as a ratio to C_T which then can be easily converted to percent thrust coefficient or, in ratio form,

$$\frac{C_{\Delta F}}{C_T} = T_{rec} - \cos\ (\alpha + \delta) \tag{A17}$$

REFERENCES

1. Corson, Blake W., Jr.; Capone, Francis J.; and Putnam, Lawrence E. Lift induced on a Swept Wing by a Two-Dimensional Partial-Span Deflected Jet at Mach Numbers From 0.20 to 1.30. NASA TM X-2309, 1971.
2. Capone, Francis J.: Exploratory Investigation of Lift Induced on a Swept Wing by a Two-Dimensional Partial-Span Deflected Jet at Mach Numbers From 0.20 to 1.30 NASA TM X-2529, 1972
3. Capone, Francis J.. Supercirculation Effects Induced by Vectoring a Partial-Span Rectangular Jet. J. Aircraft, vol. 12, no. 8, Aug 1975, pp. 633-638.
4. Capone, Francis J.. The effects on Propulsion-Induced Aerodynamic Forces of Vectoring a Partial-Span Rectangular Jet at Mach Numbers From 0 40 to 1.20. NASA TN D-8039, 1975.
5. Capone, Francis J. Effects of Nozzle Exit Location and Shape on Propulsion-Induced Aerodynamic Characteristics Due to Vectoring Twin Nozzles at Mach Numbers From 0.40 to 1.2. NASA TM X-3313, 1976.
6. Capone, Francis J . A Summary of Experimental Research on Propulsive-Lift Concepts in the Langley 16-Foot Transonic Tunnel. AIAA Paper No. 75-1315, Oct. 1975.
7. Corson, Blake W., Jr.; Runckel, Jack F., and Igoe, William B.: Calibration of the Langley 16-Foot Transonic Tunnel With Test Section Air Removal. NASA TR R-423, 1974
8. Reubush, David E., and Runckel, Jack F.: Effect of Fineness Ratio on Boattail Drag of Circular-Arc Afterbodies Having Closure Ratios of 0 50 With Jet Exhaust at Mach Numbers up to 1.30. NASA TN D-7192, 1972.
9. Braslow, Albert L., and Knox, Eugene C.: Simplified Method for Determination of Critical Height of Distributed Roughness Particles for Boundary-Layer Transition at Mach Numbers From 0 to 5. NACA TN-4363, 1958.
10. Braslow, Albert L.; Hicks, Raymond M.; and Harris, Roy V , Jr.: Use of Grit-Type Boundary-Layer-Transition Trips on Wind-Tunnel Models NASA TN D-3579, 1966.

TABLE I. - AIRFOIL ORDINATES

Note· Airfoil ordinates are nondimensionalized with respect to local chords perpendicular to the 50 percent chord line.

Chordwise ordinate	Upper surface ordinate	Lower surface ordinate
0.00	0.0000	0 0000
.02	.0136	- 0140
.04	.0167	-.0179
.06	.0188	-.0205
.08	.0204	-.0225
.10	.0218	-.0240
.15	.0246	-.0267
.18	.0259	- 0278
.25	.0281	- 0294
.30	.0292	-.0299
.40	.0300	-.0296
.50	0292	- 0275
.60	.0267	-.0230
.68	.0233	-.0176
.75	.0191	-.0124
.78	.0169	-.0103
.80	.0152	-.0091
.82	0134	-.0082
.84	.0114	-.0075
.86	.0091	-.0071
.88	.0067	-.0073
.90	.0040	- 0079
.92	.0010	-.0092
.94	-.0024	-.0111
.96	-.0061	-.0139
.98	-.0103	-.0175
1 00	-.0150	-.0220

TABLE II. - BODY ORDINATES

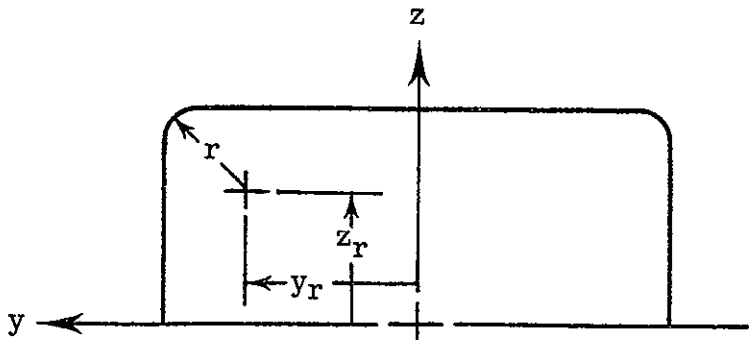

x, cm	y, cm	z, cm	r, cm	$\pm y_r$, cm	$\pm z_r$, cm
0	0	0	0	0	0
2.54	.914	.812	.812	.102	↓
5.08	1.816	1.603	1.603	.213	↓
7.62	2.695	2.360	2.360	.335	↓
10.16	3.551	3.078	3.078	.472	↓
15.24	5.192	4.379	4.379	813	↓
20.32	6.711	5.420	5.420	1.290	↓
22.86	7.417	5.814	5.814	1.603	↓
25.40	8.082	6.109	6.109	1.974	↓
30.48	9.268	6.350	6.350	2.918	↓
38.10	10.620	↓	↓	4.270	↓
45.72	11.338	↓	↓	4.988	↓
49.53	11.430	↓	↓	5.080	↓
55.88	↓	↓	4.618	6.812	1.732
63.50	↓	↓	2.540	8.890	3.810
98.90	↓	↓	2.540	8.890	3.810
99.16	↓	↓	2.540	8.890	3.810
119.38	↓	↓	2.540	8.890	3.810
120.65	↓	6.266	2.540	8.867	3.701
121.92	↓	5.994	2.403	9.027	3.592
127.00	↓	4.877	1.717	9.713	3.160
132.08	↓	3.749	1.026	10.404	2.723
138.68	↓	2.286	.127	11.303	2.159

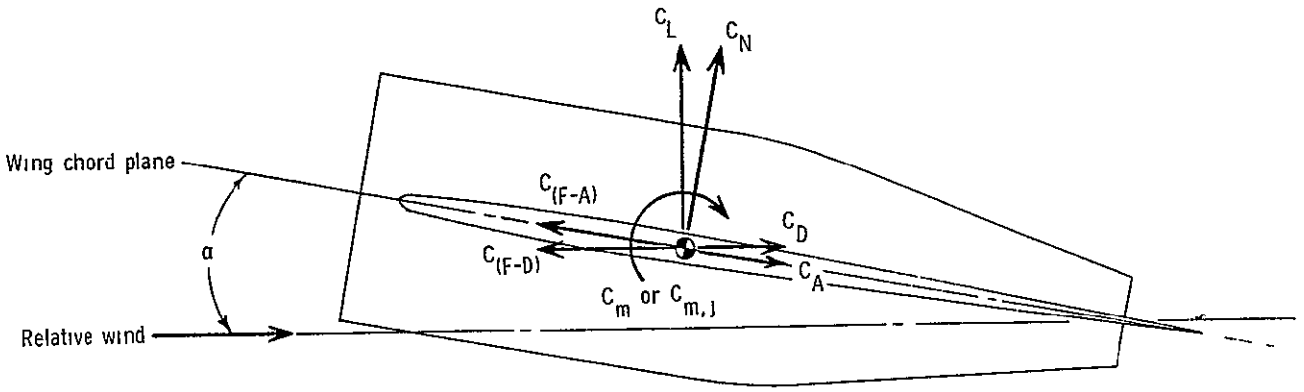

(a) External forces

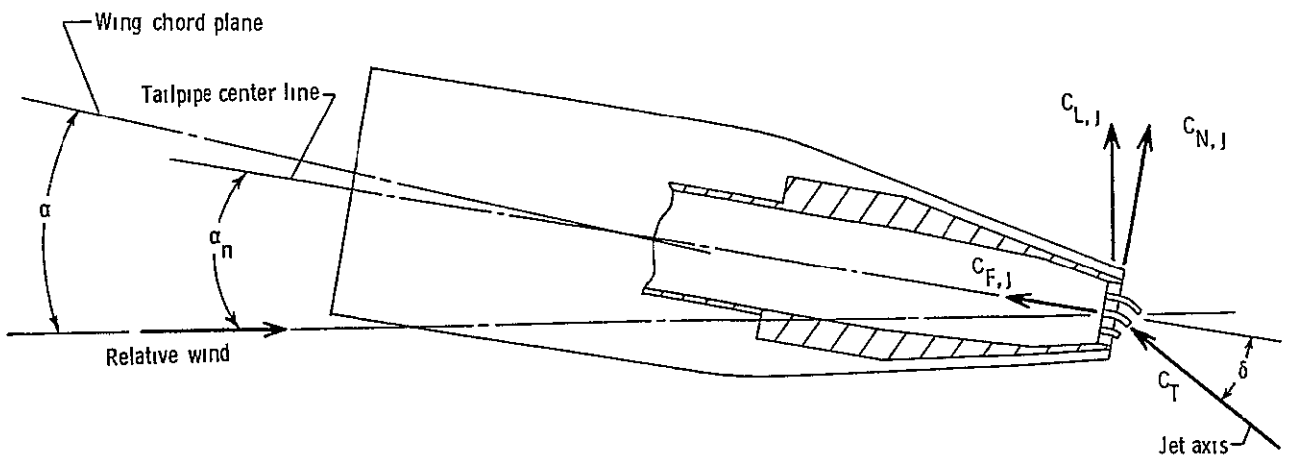

(b) Internal forces

Figure 1 - Definition of model forces showing positive directions

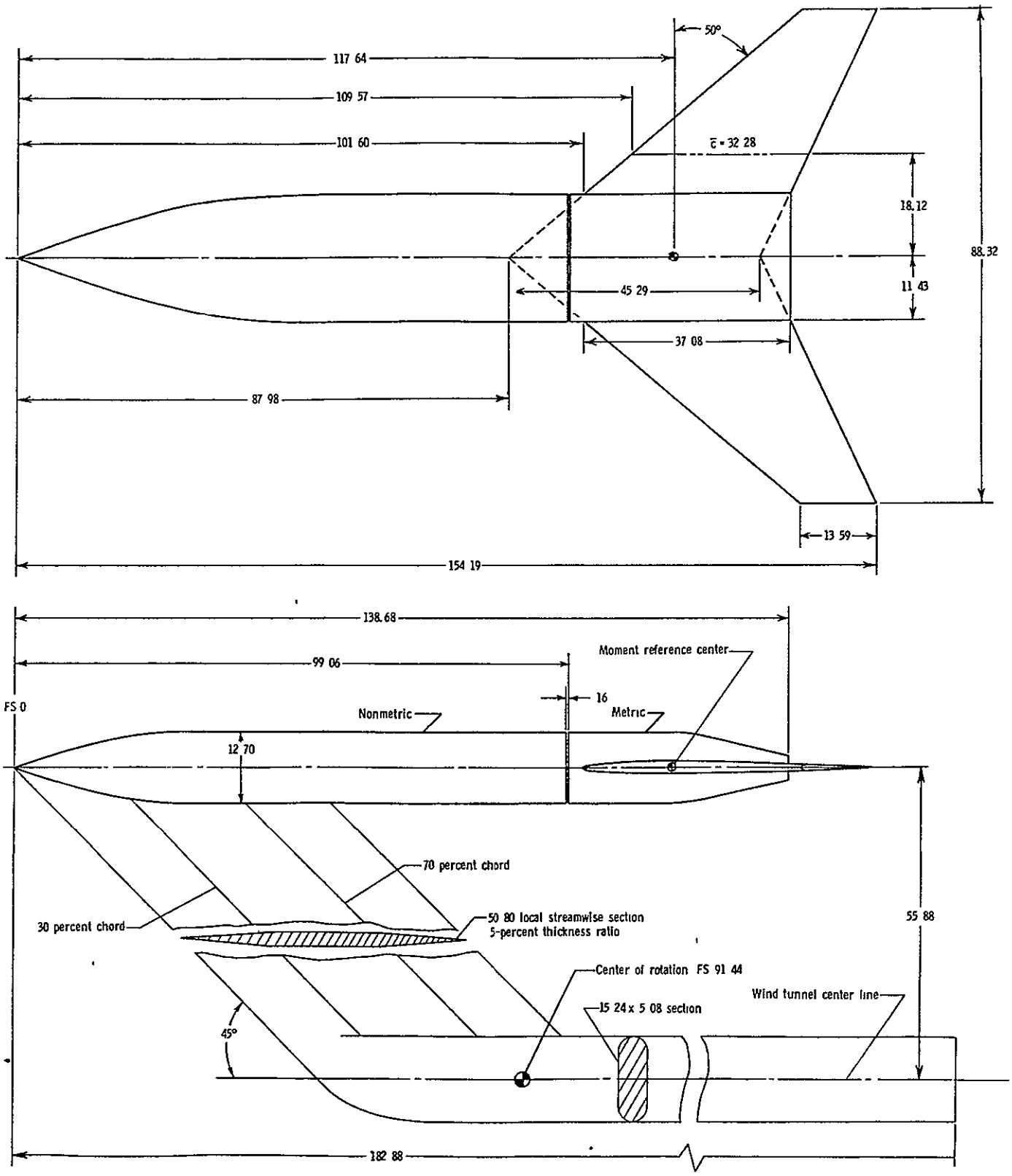

Figure 2 - Drawing of model All dimensions in centimeters unless otherwise noted.

ORIGINAL PAGE IS
OF POOR QUALITY

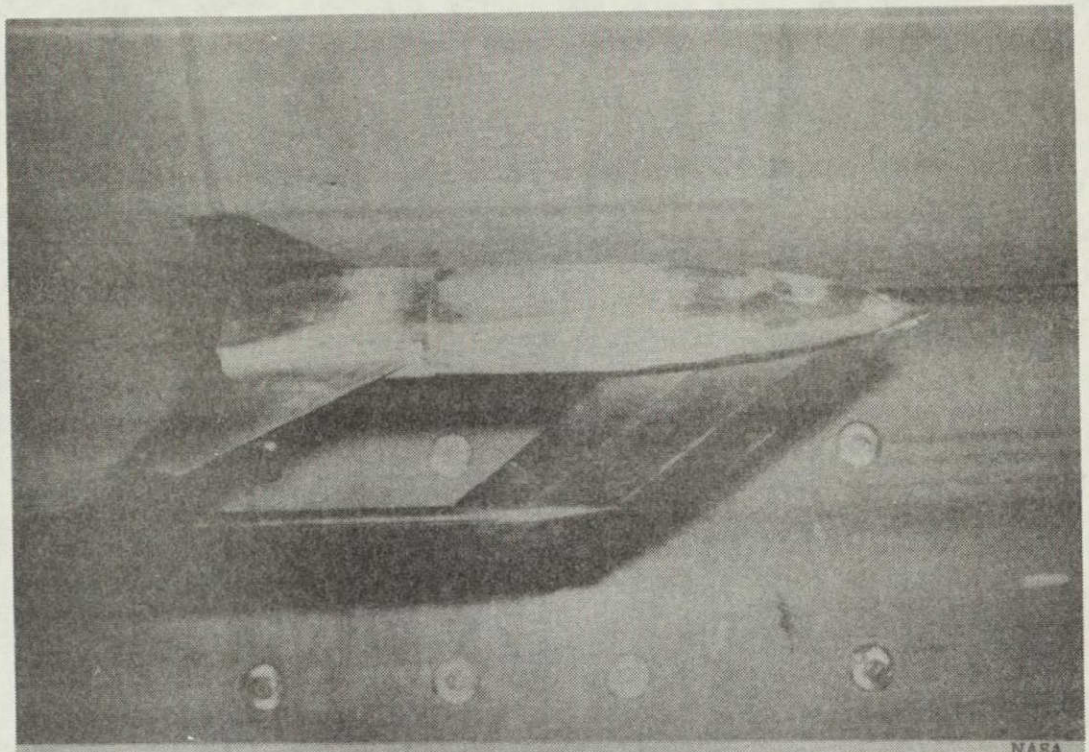

NASA
L-74-390

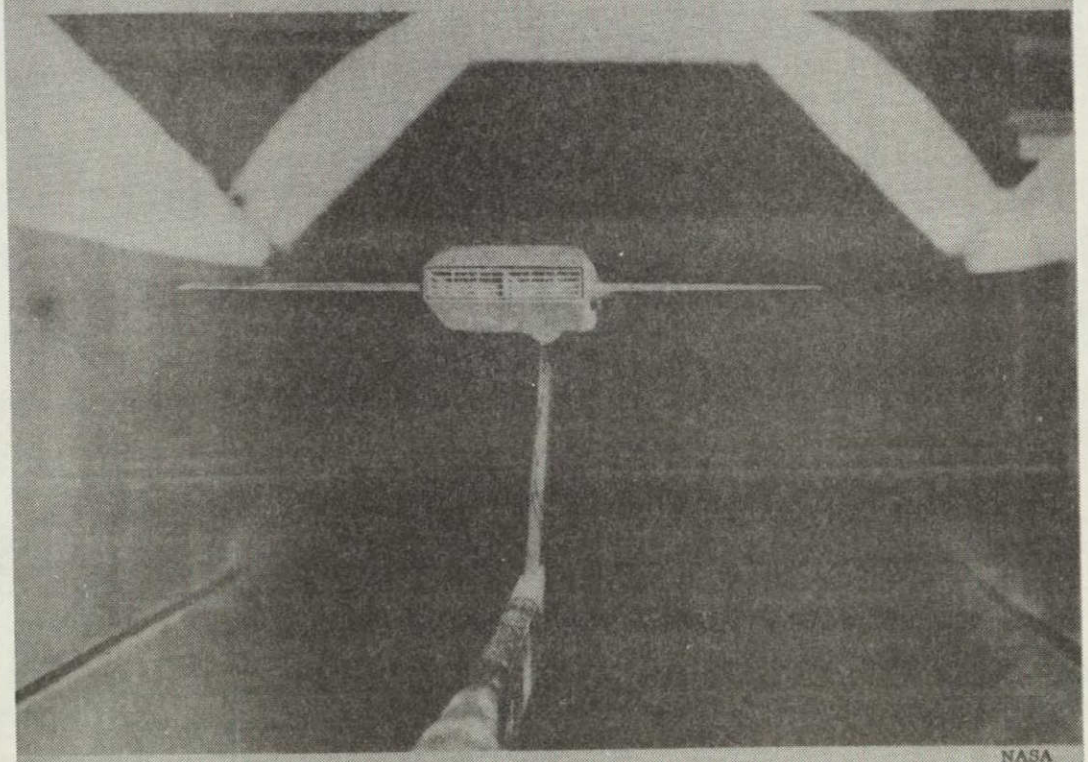

NASA
L-74-231

Figure 3. - Photographs of model.

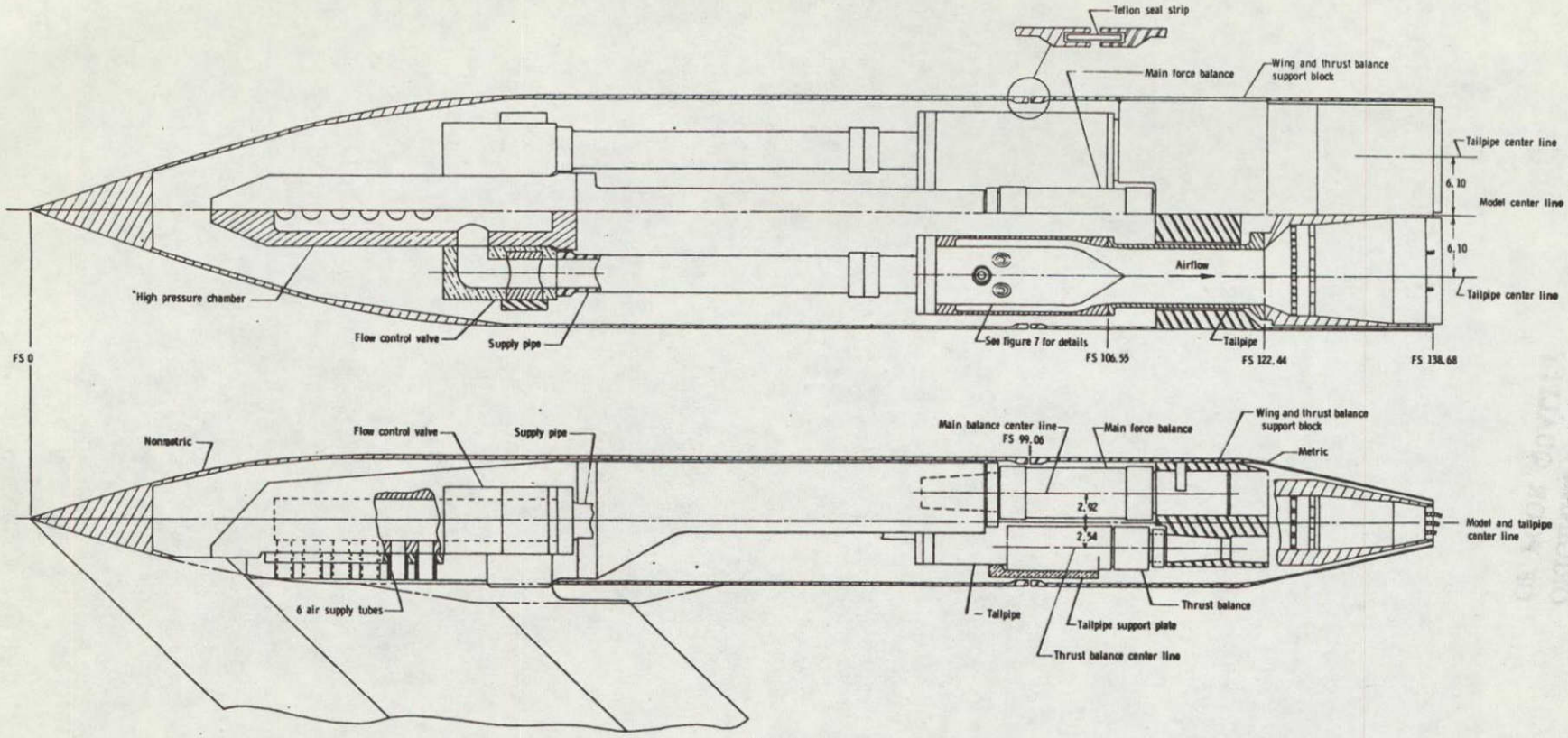

(a) Sketch of system.

Figure 4. - Details of twin-jet, exhaust-nozzle, simulation system. All dimensions in centimeters unless otherwise noted.

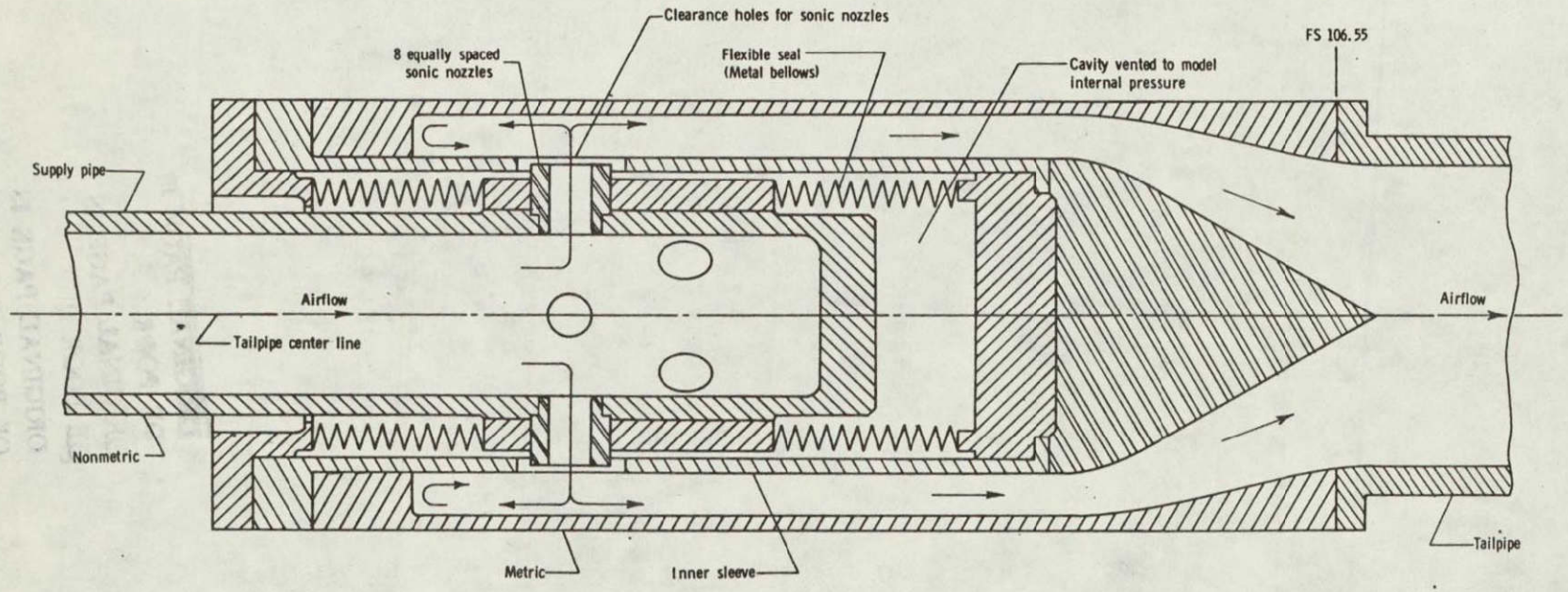

(b) Details of bellows arrangement used to transfer air from the non-metric to metric portions of the model.
Figure 4. -Continued.

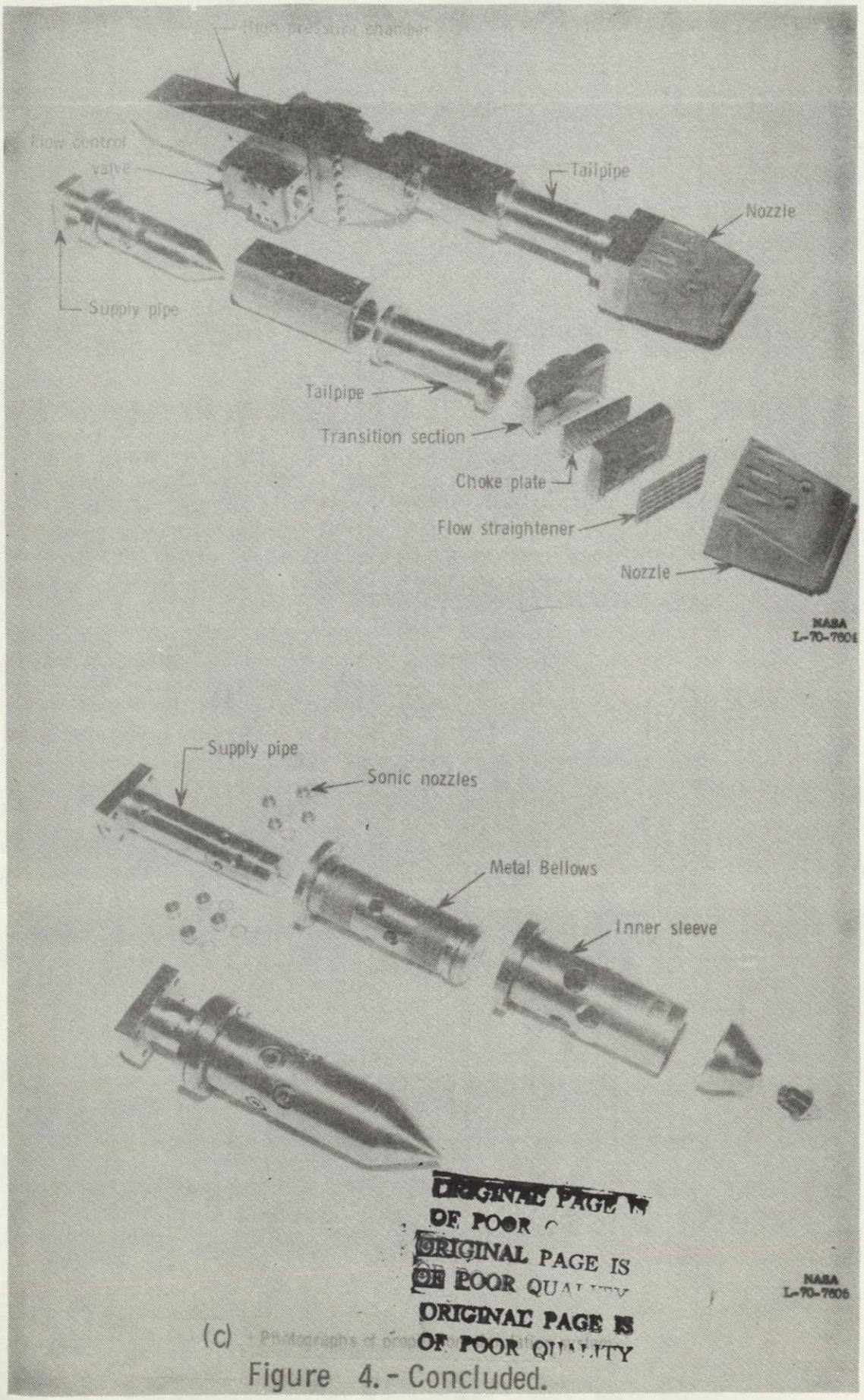

ORIGINAL PAGE IS
OF POOR QUALITY

(c) Photographs of [illegible]

ORIGINAL PAGE IS
OF POOR QUALITY

Figure 4. - Concluded.

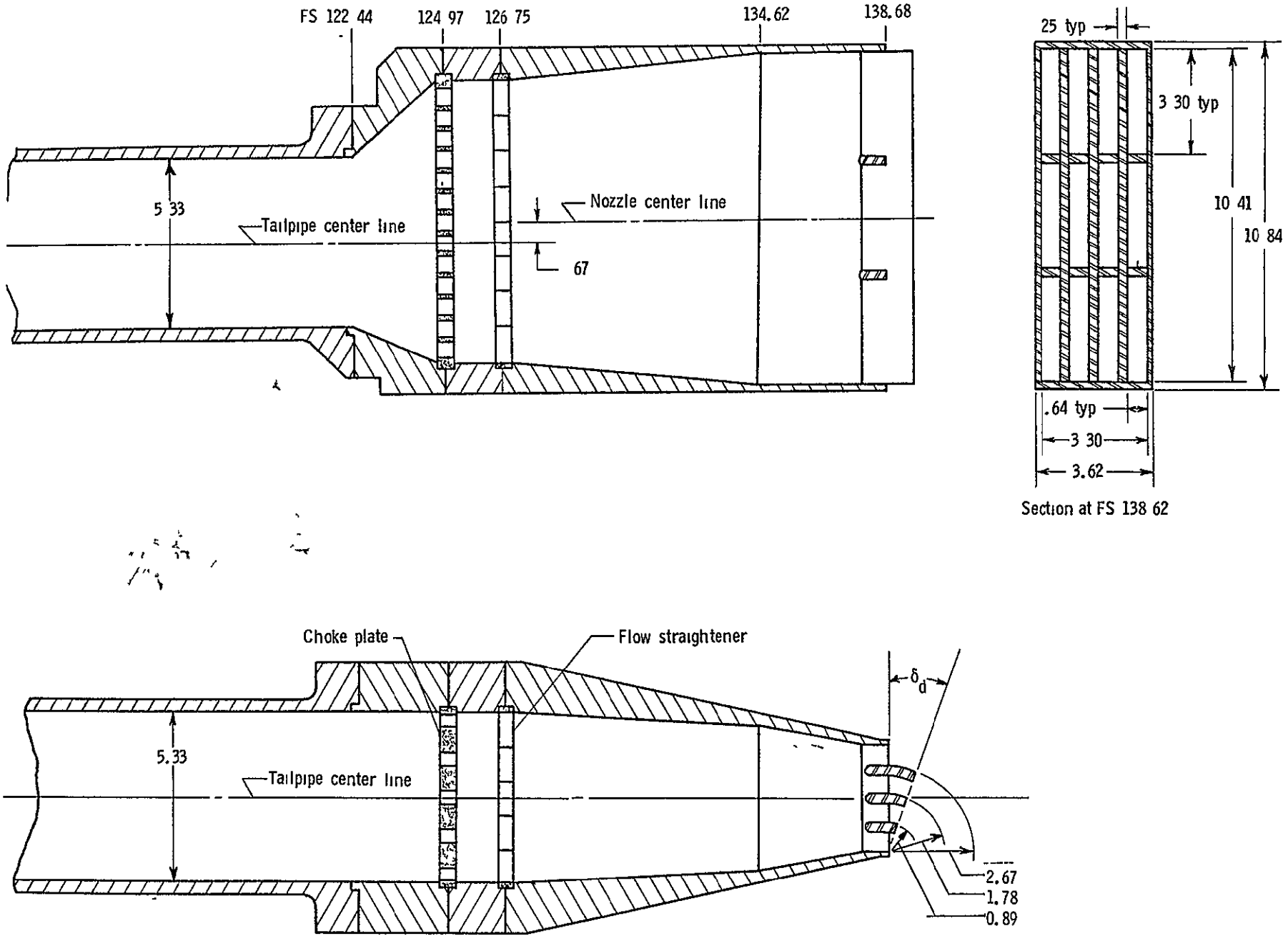

Figure 5.- Nozzle details All dimensions in centimeters except as noted

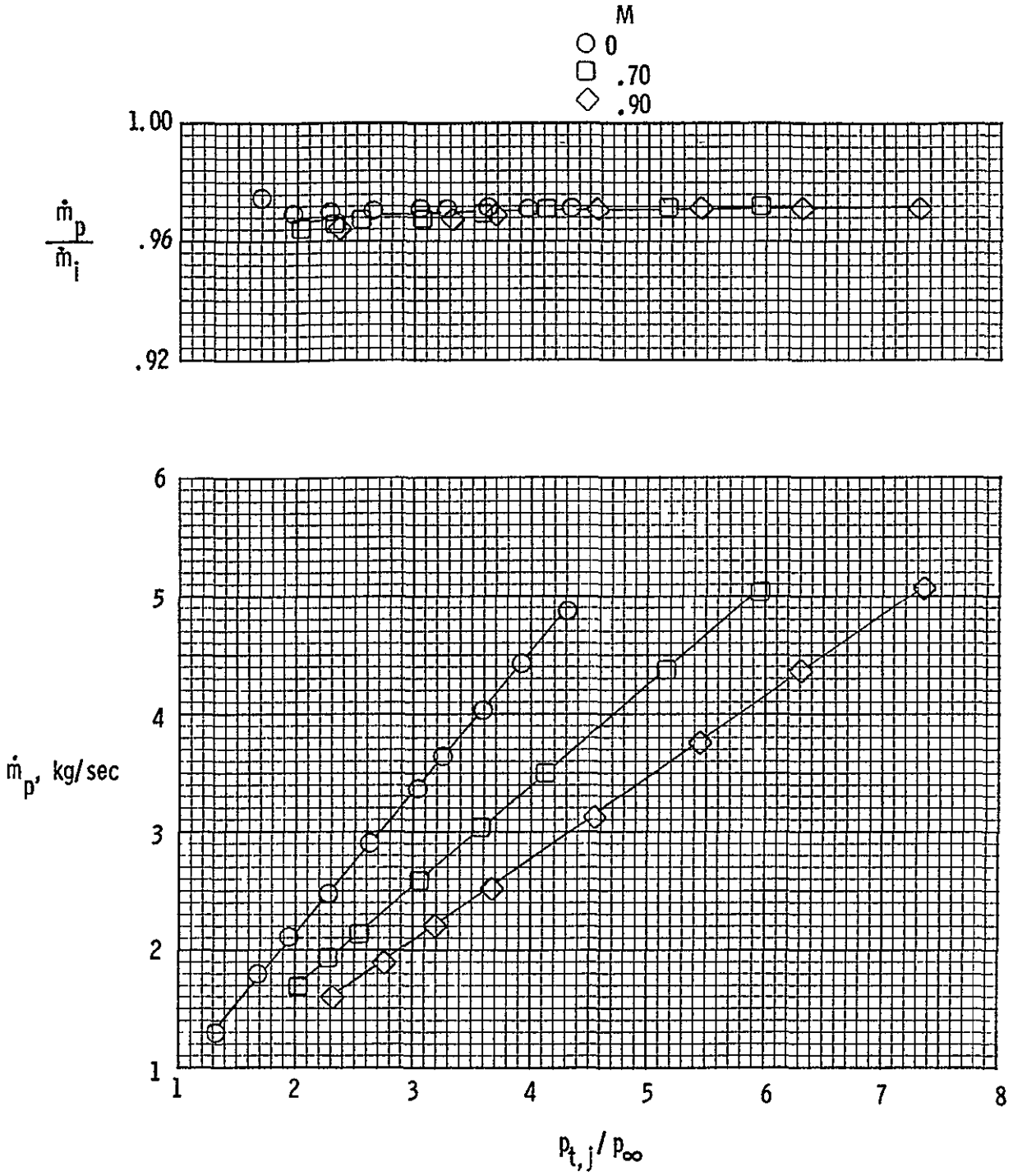

Figure 6.- Typical mass flow rate and discharge coefficient.

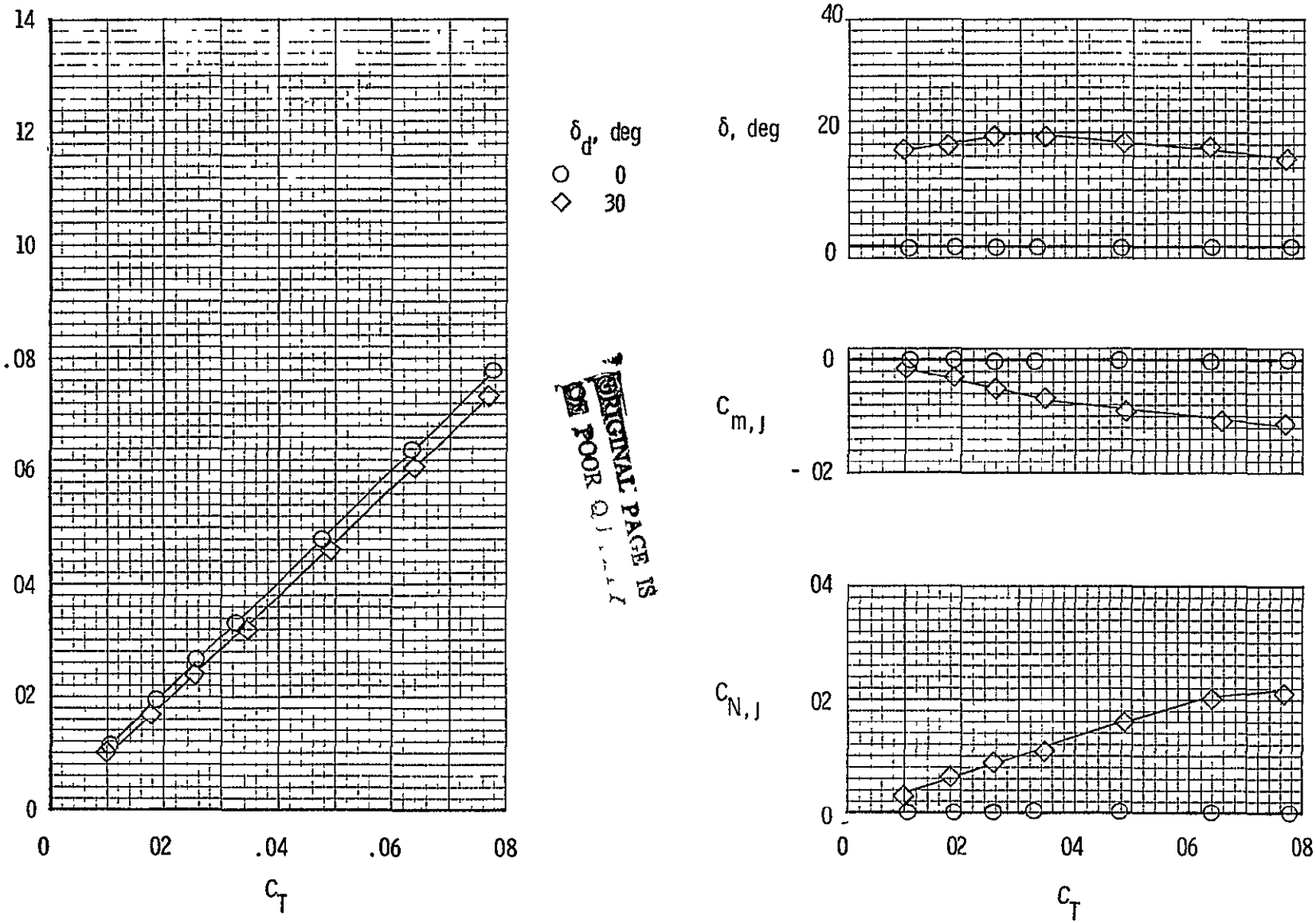

ORIGINAL PAGE IS OF POOR QUALITY

Figure 7. - Static thrust and effective turning angle characteristics.

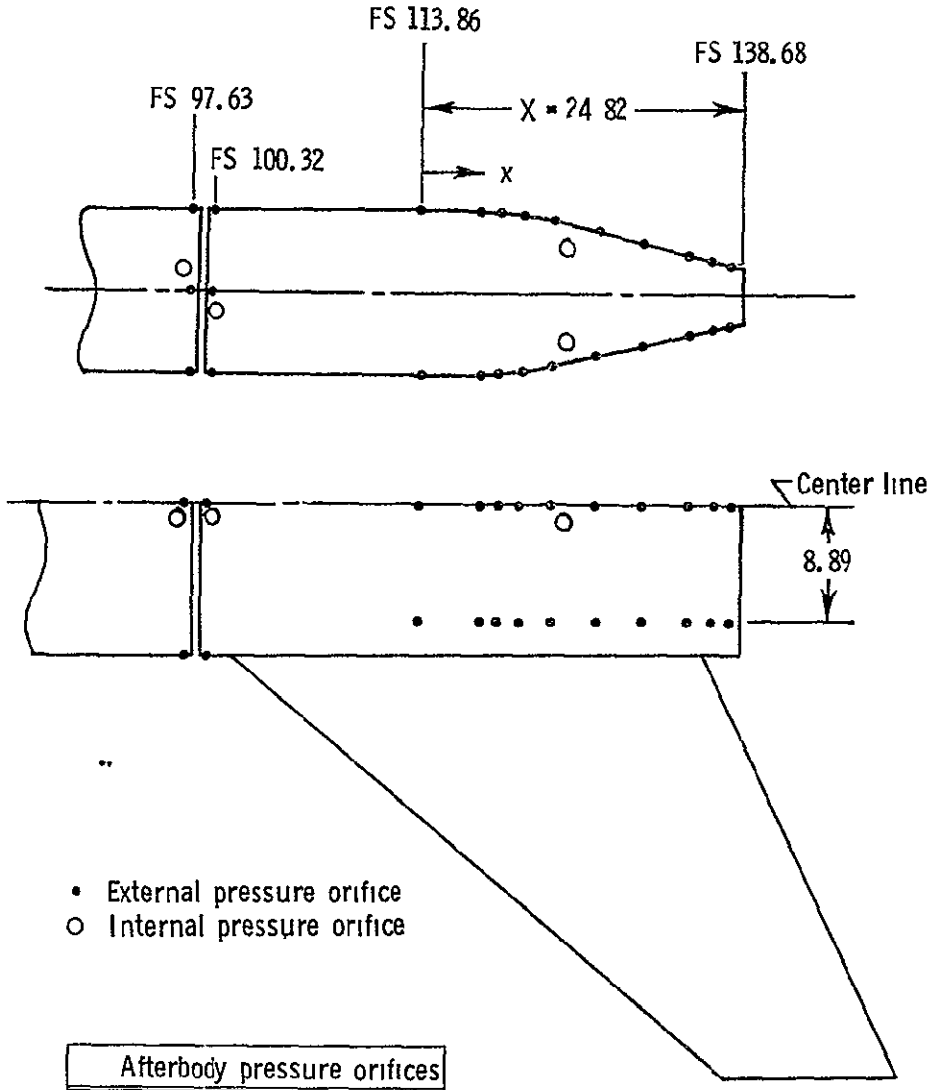

Afterbody pressure orifices	
x, cm	x/X
0	0
4.88	.200
6.25	.257
7.64	.315
10.41	.429
13.89	.572
17.35	.714
20 83	.858
22.88	.943
23 77	.980

Figure 9. - Sketch showing location of various pressure instrumentation. Typical internal pressures shown at approximate locations.

PRECEDING PAGE BLANK NOT FILMED

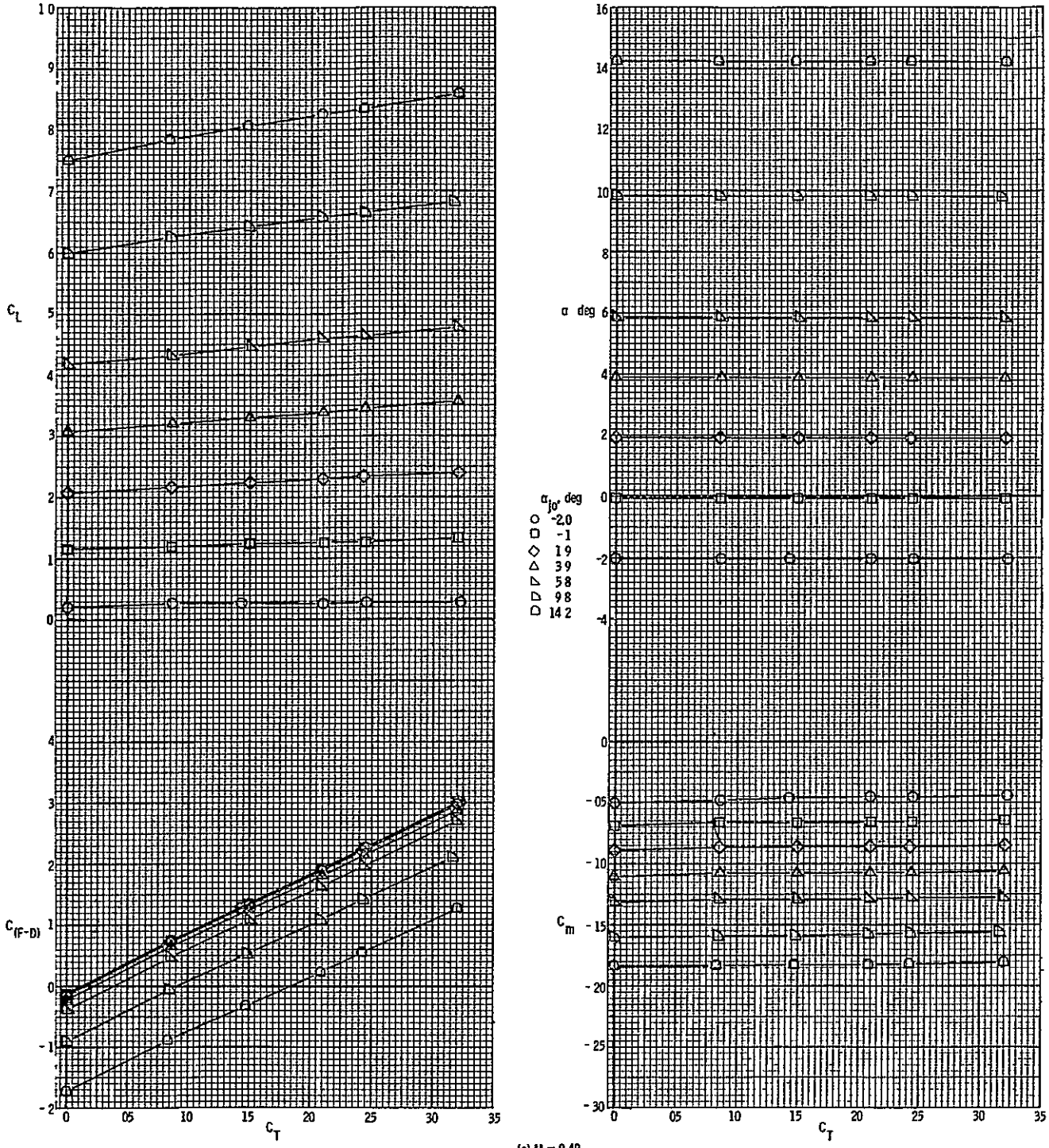

(a) M = 0.40

Figure 10 - Basic aerodynamic characteristics $\delta_d = 0^\circ$

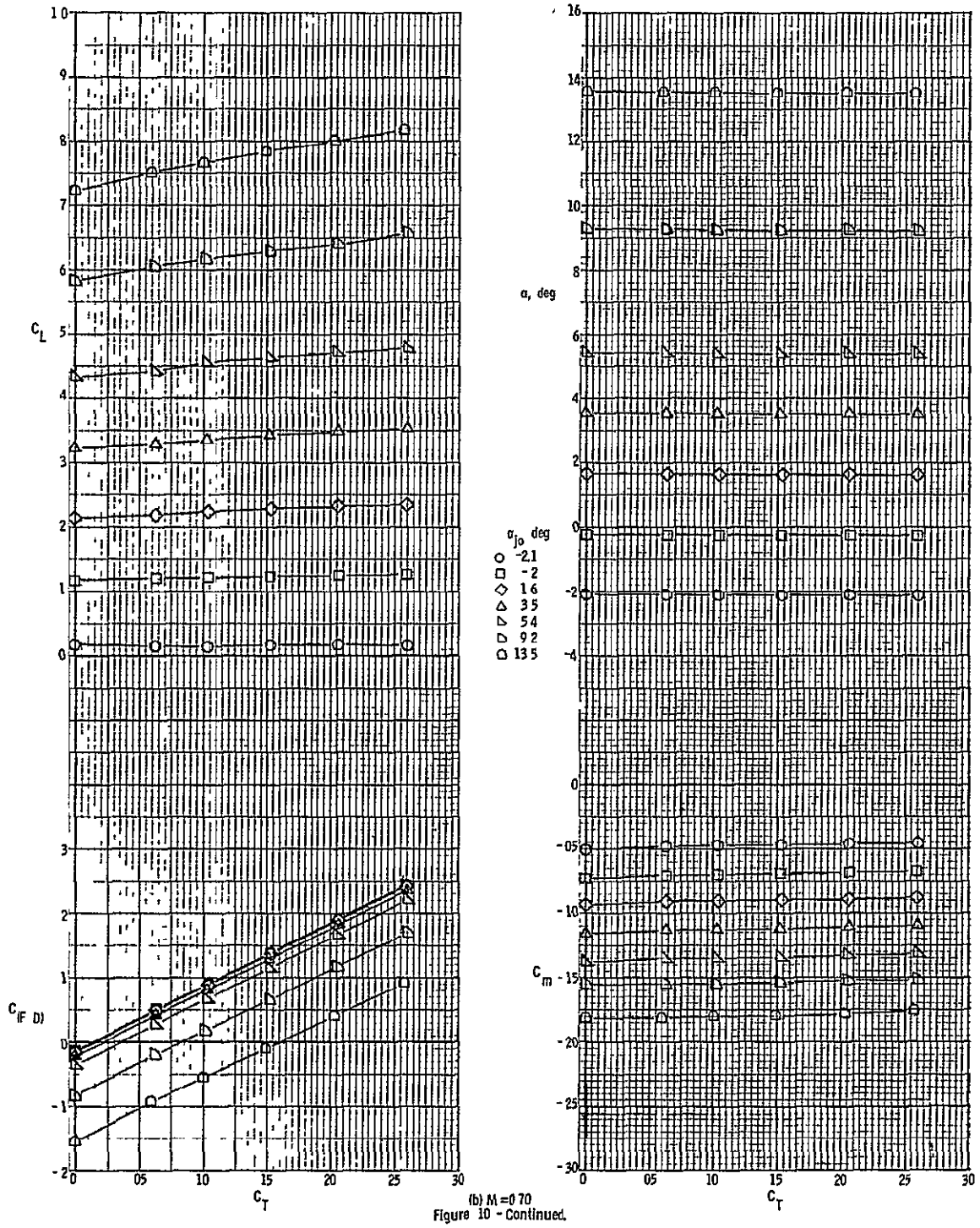

(b) M = 0.70

Figure 10 - Continued.

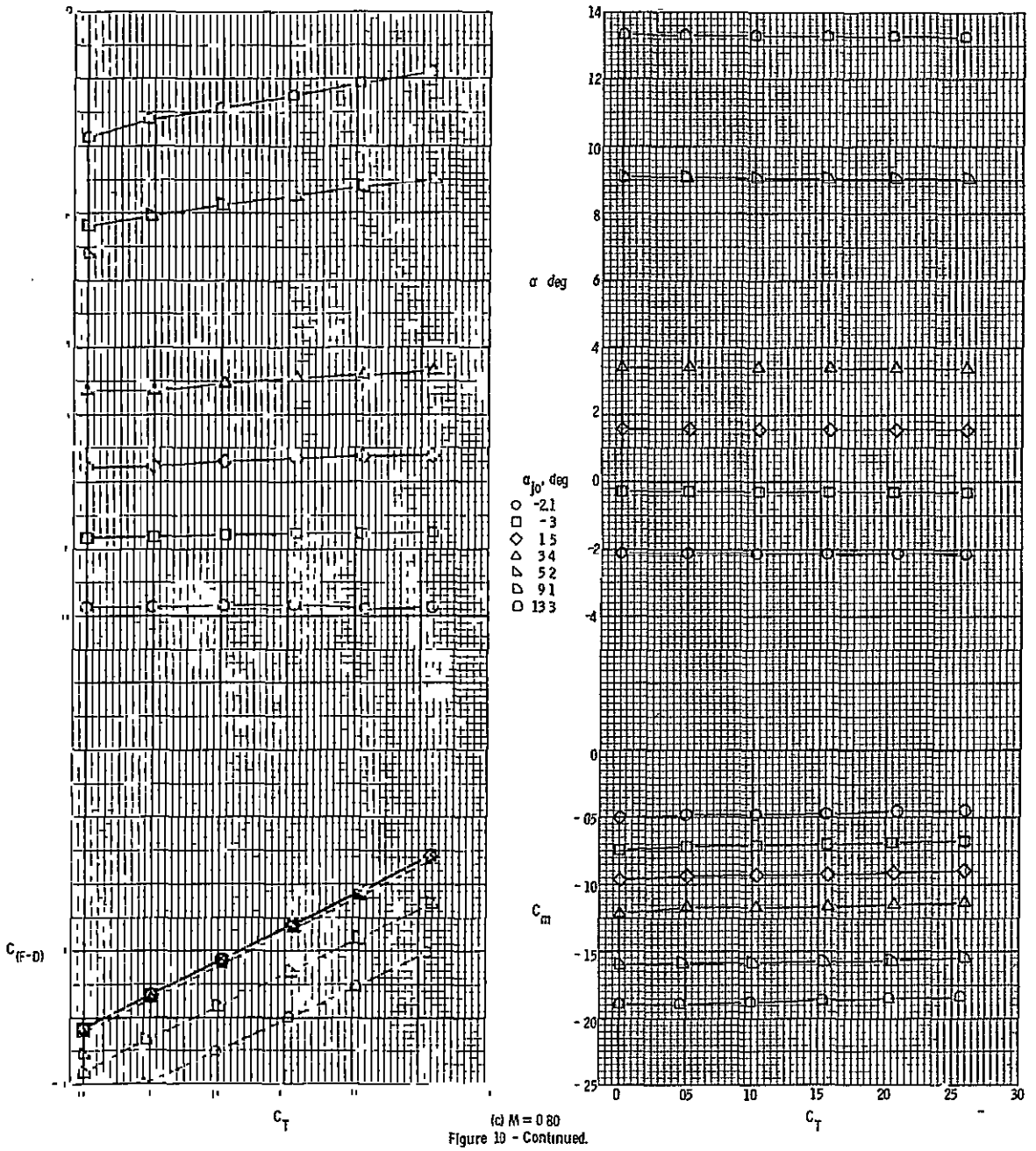

(c) M = 0.80

Figure 10 - Continued.

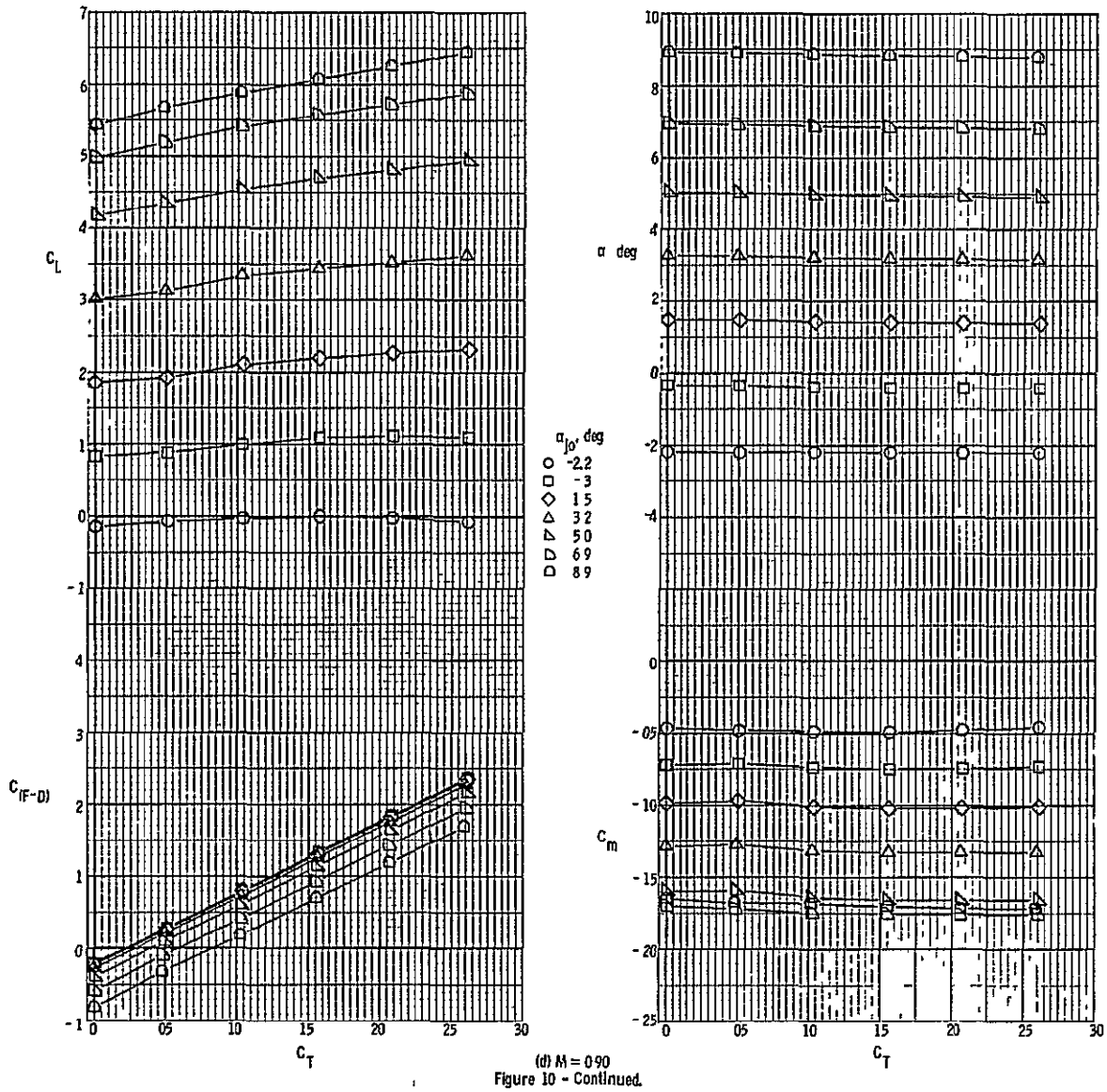

(d) M = 0.90

Figure 10 - Continued.

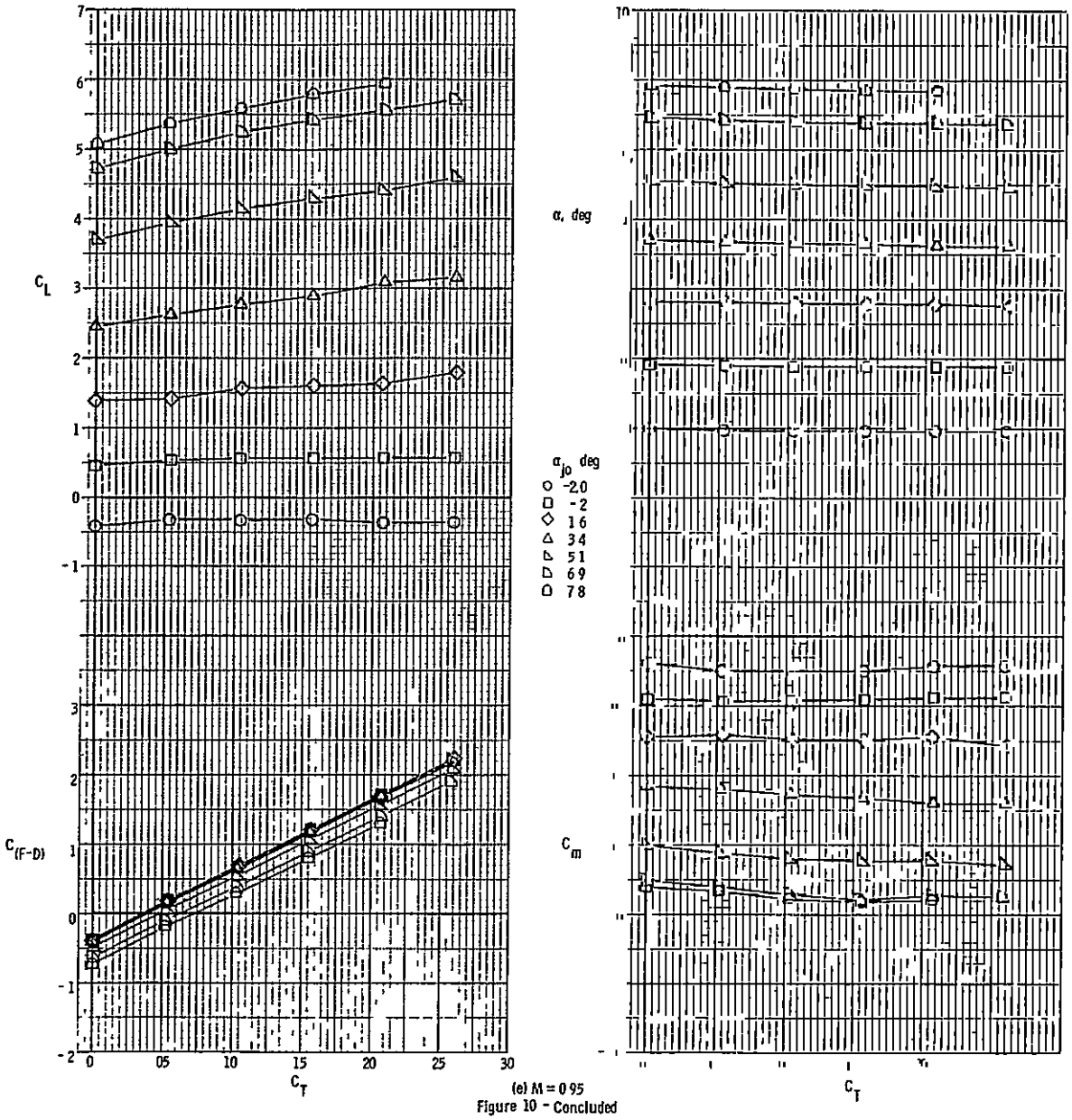

(e) M = 0.95

Figure 10 - Concluded

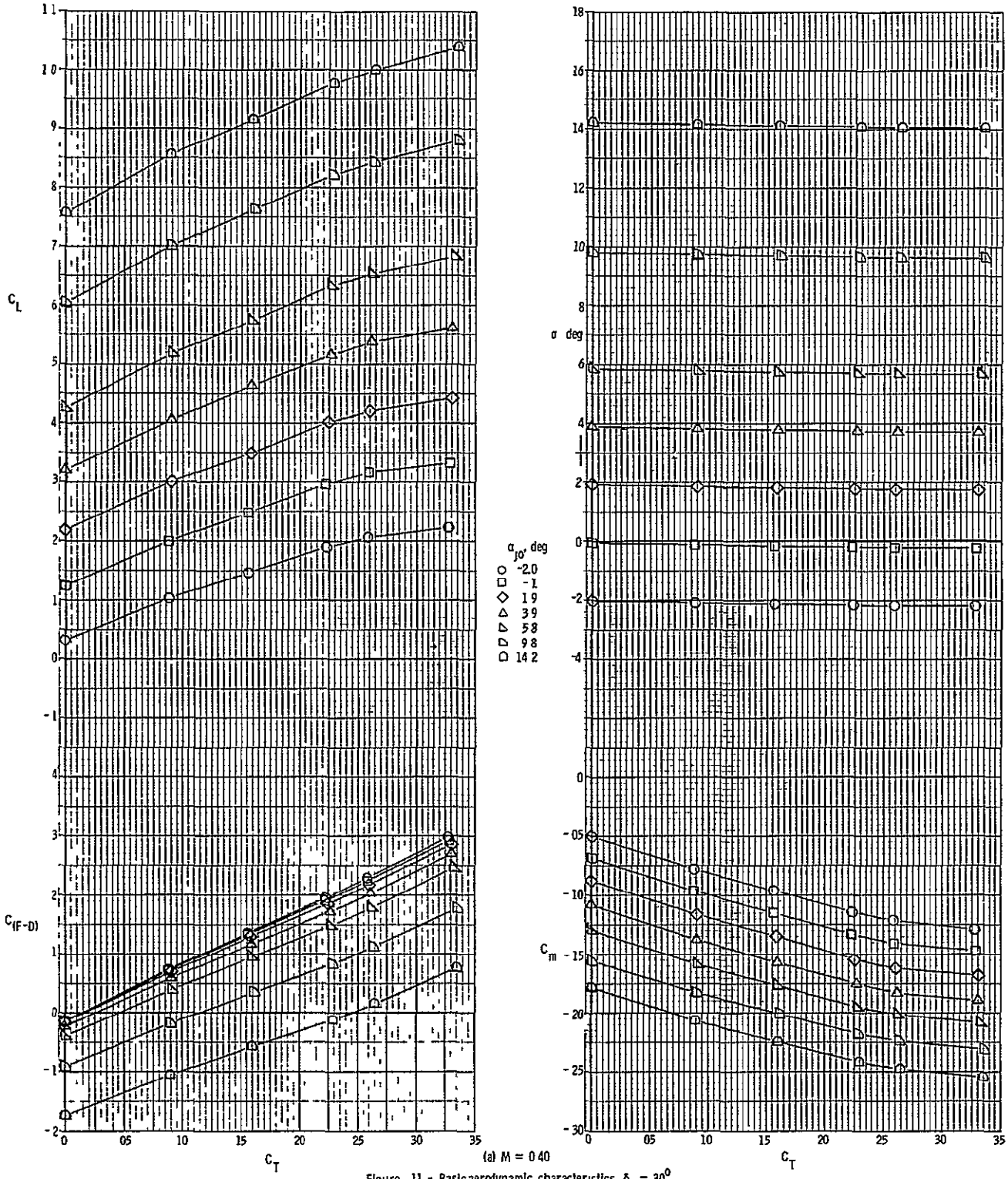

(a) M = 0.40

Figure 11 - Basic aerodynamic characteristics $\delta_d = 30^\circ$

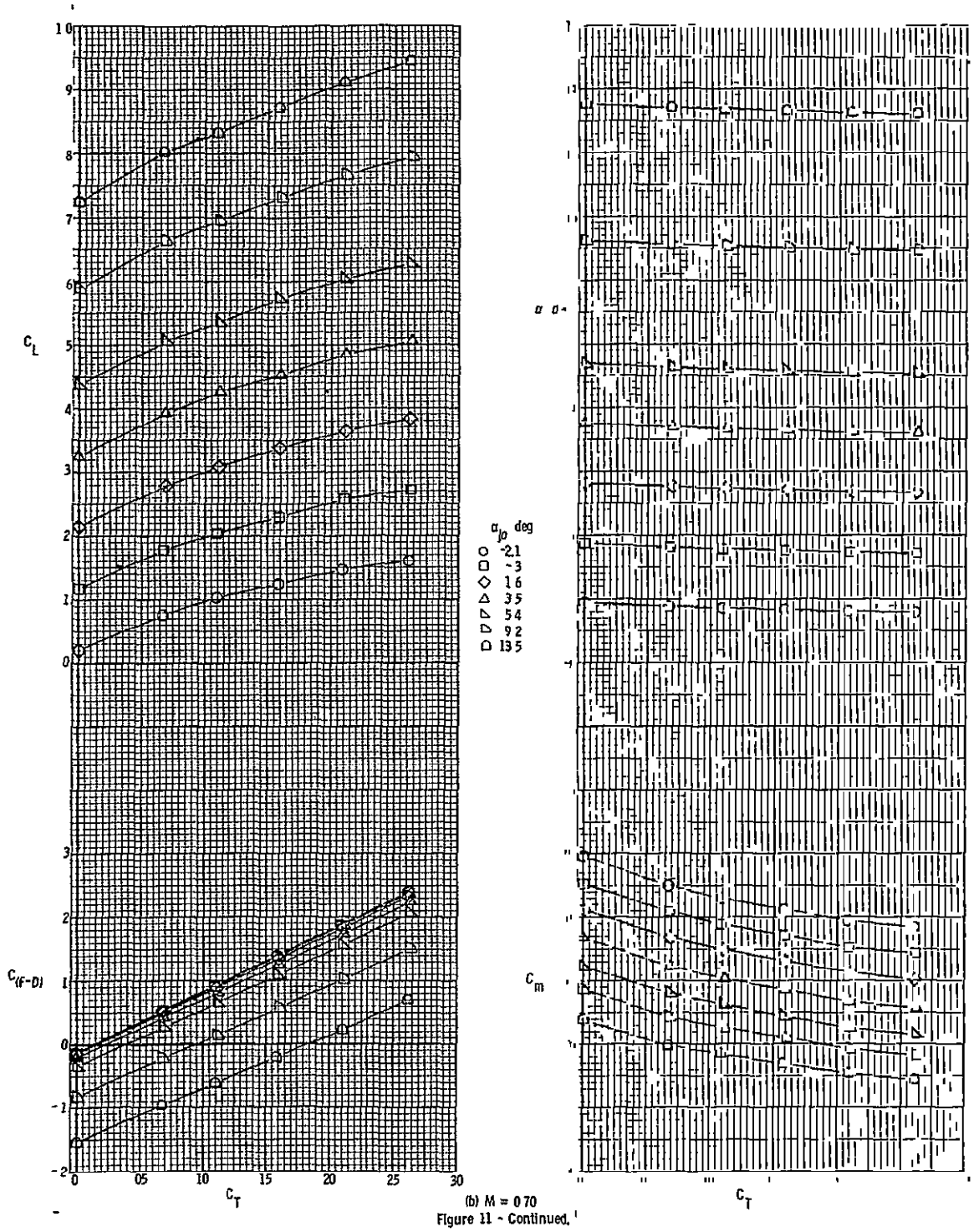

(b) M = 0.70

Figure 11 - Continued.

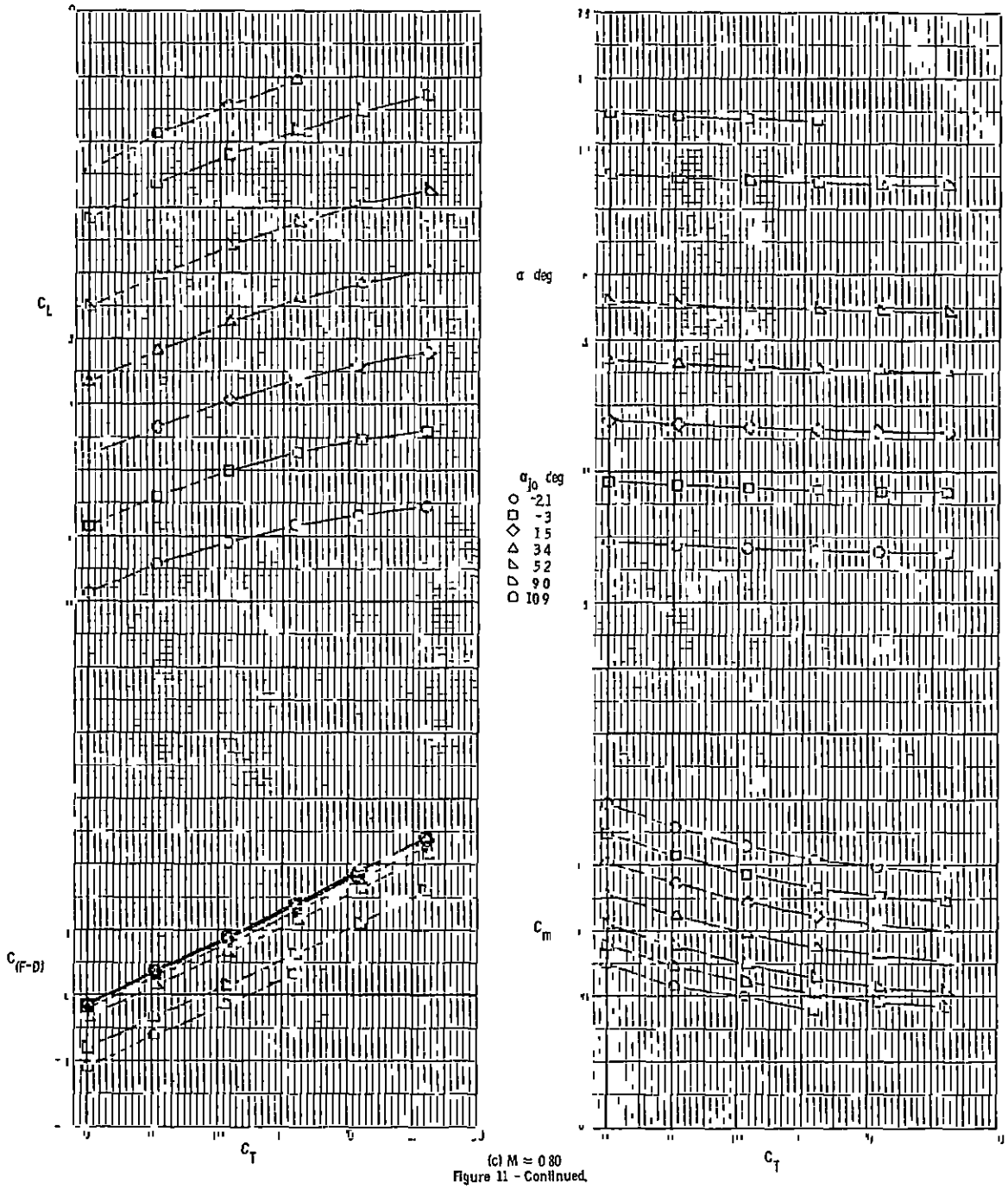

(c) M = 0.80
Figure 11 - Continued.

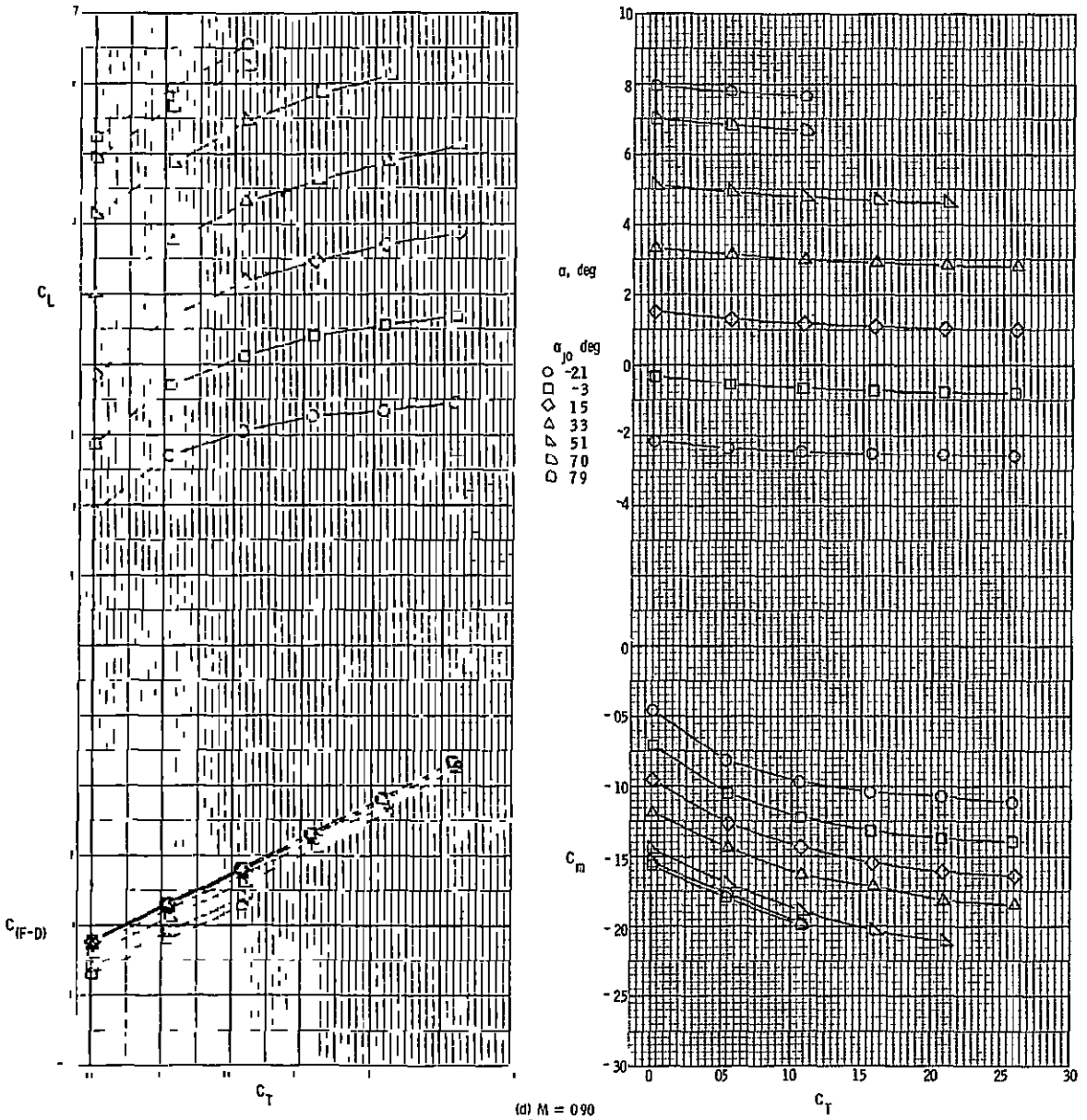

(d) M = 0.90

Figure 11 - Continued.

ORIGINAL PAGE IS
OF POOR QUALITY

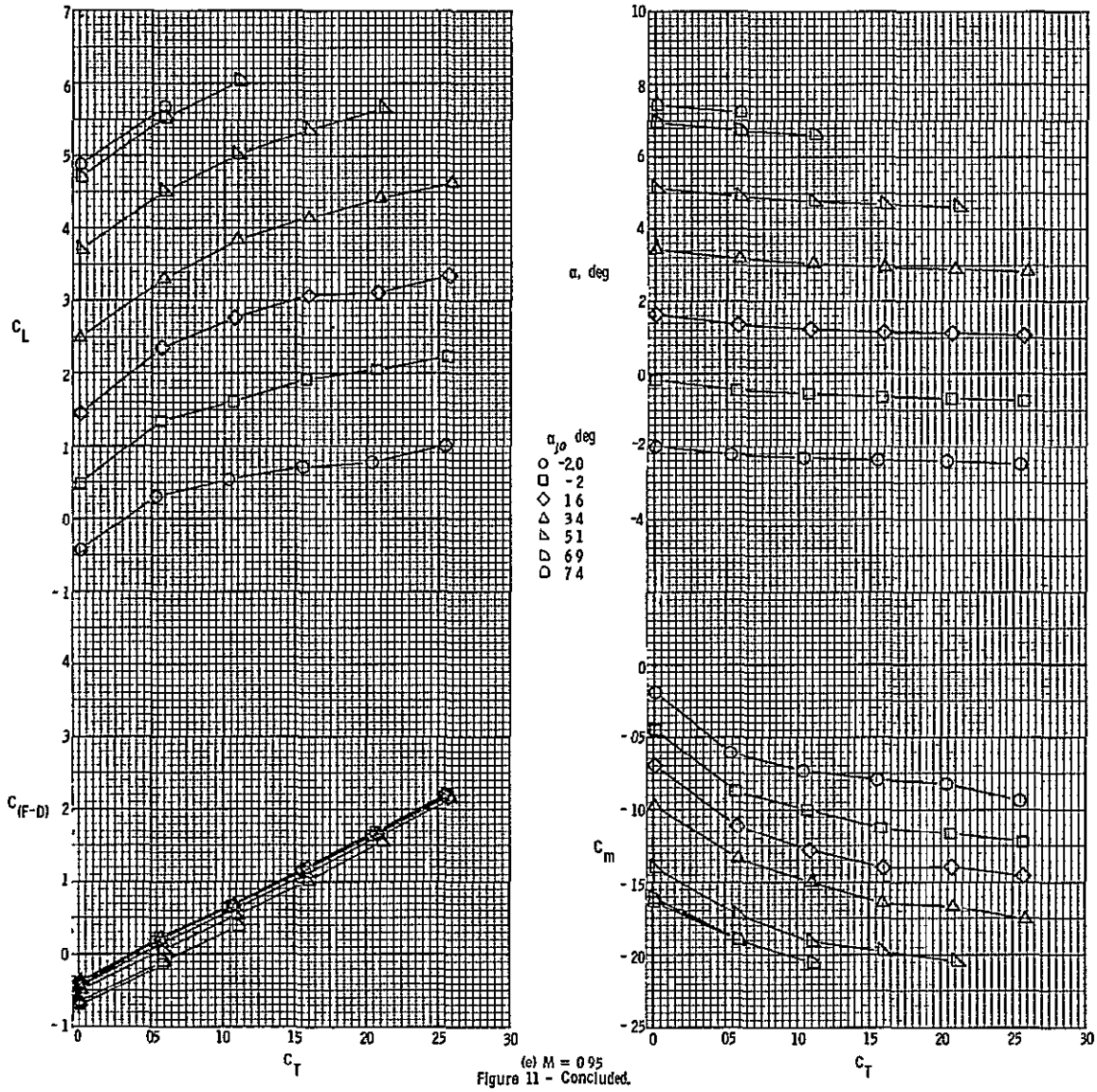

(e) M = 0.95
Figure 11 - Concluded.

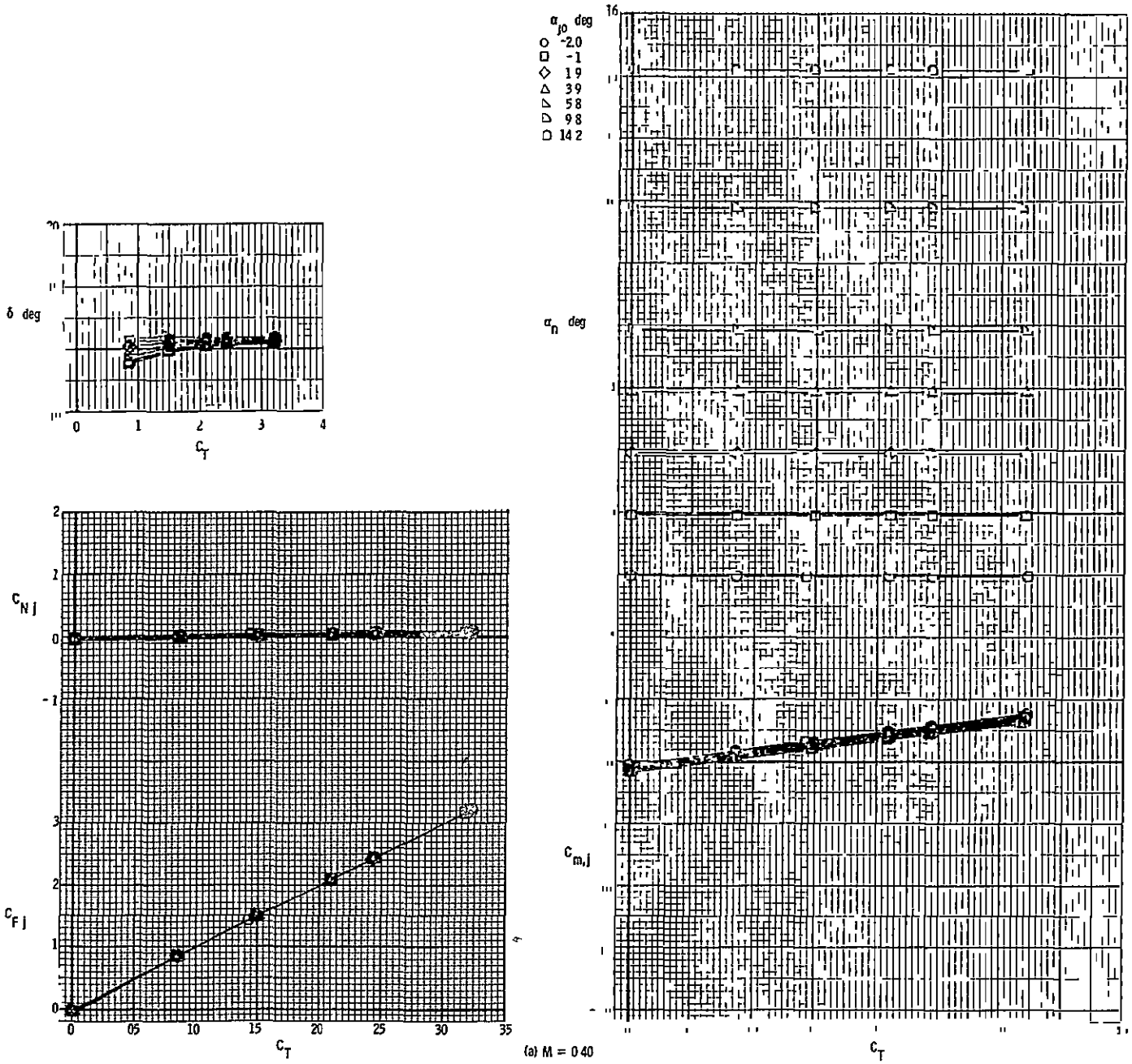

(a) M = 0.40

Figure 12 - Basic nozzle thrust characteristics $\delta_d = 0^\circ$

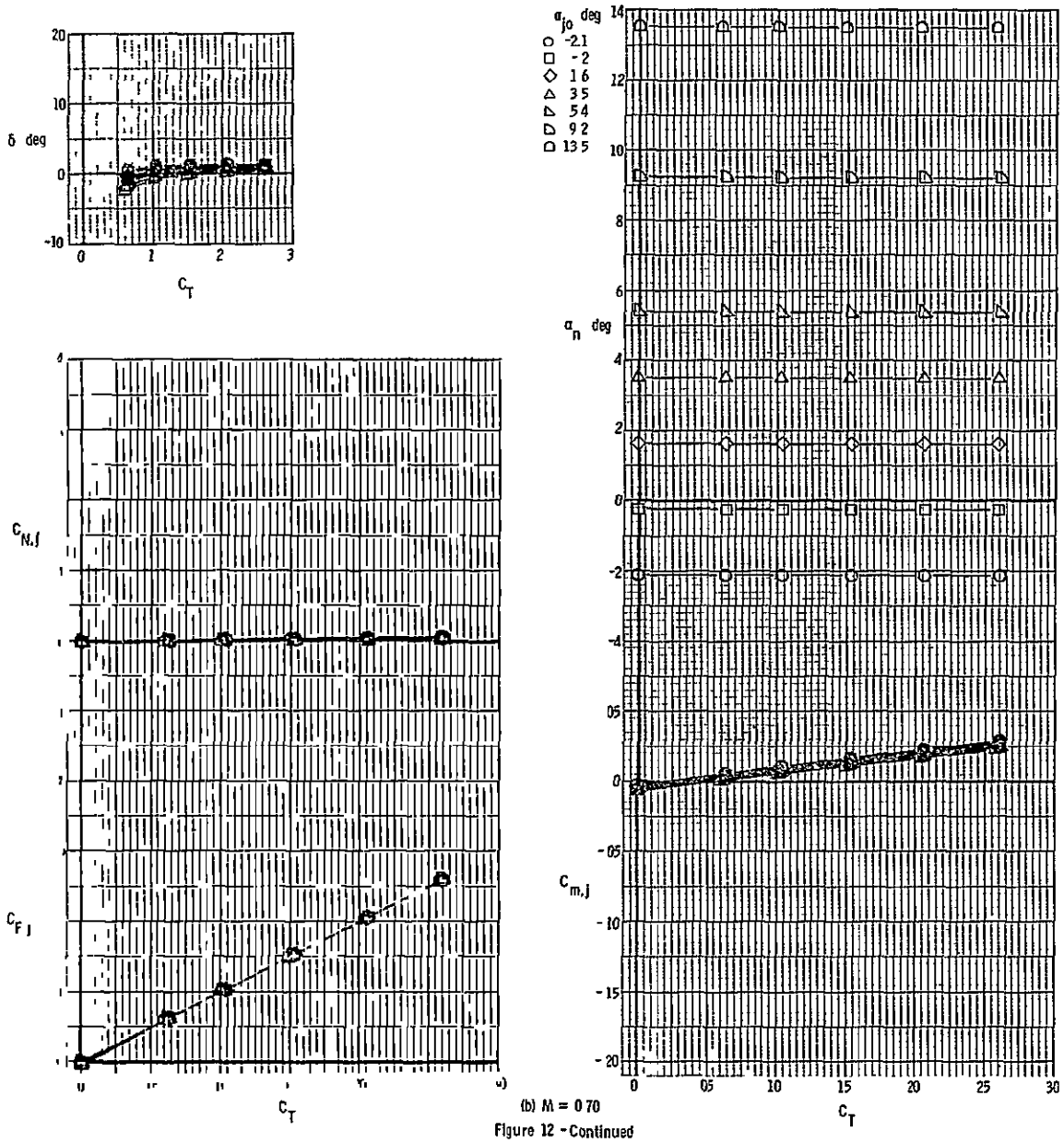

(b) M = 0.70

Figure 12 - Continued

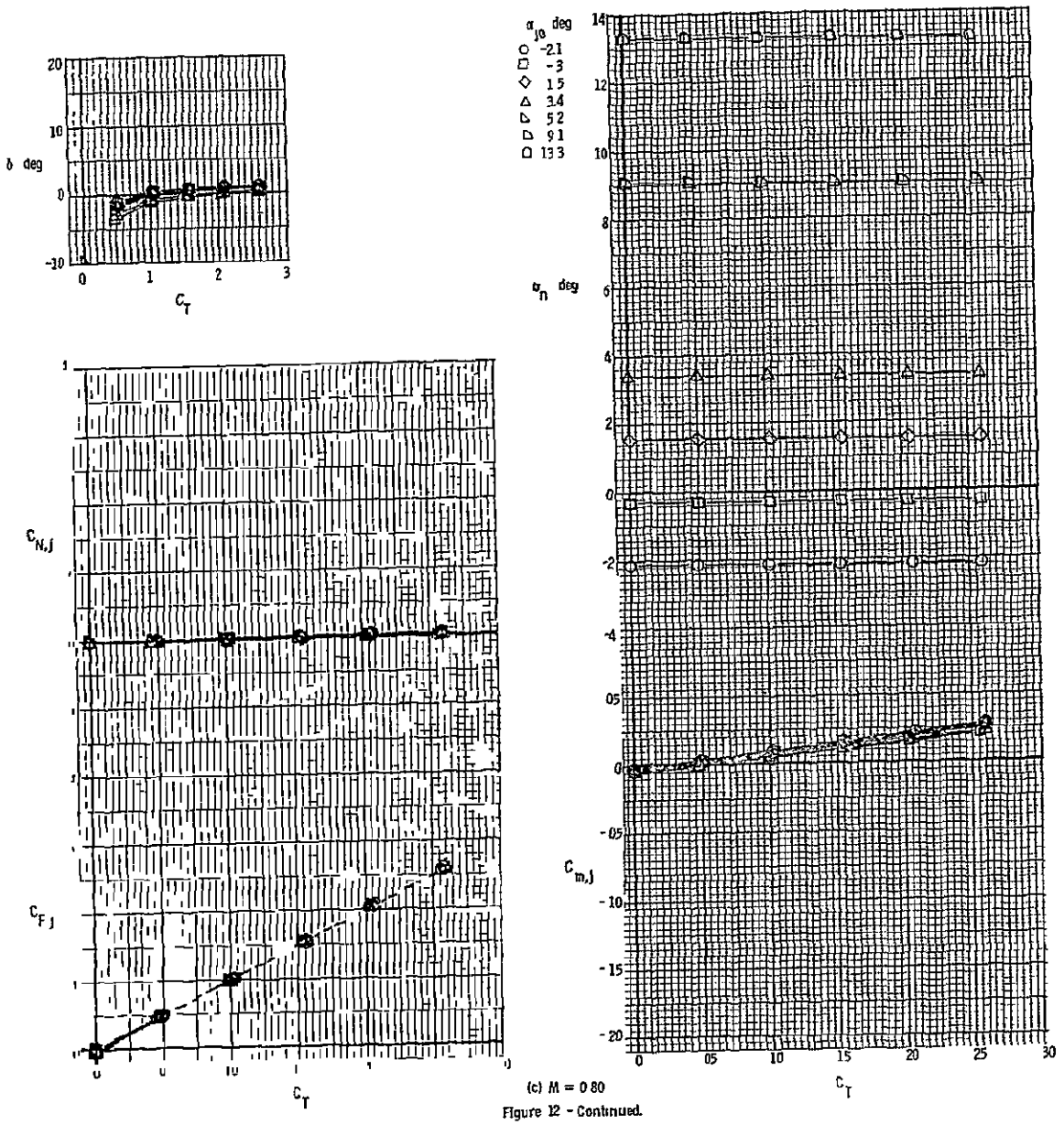

(c) M = 0.80

Figure 12 - Continued.

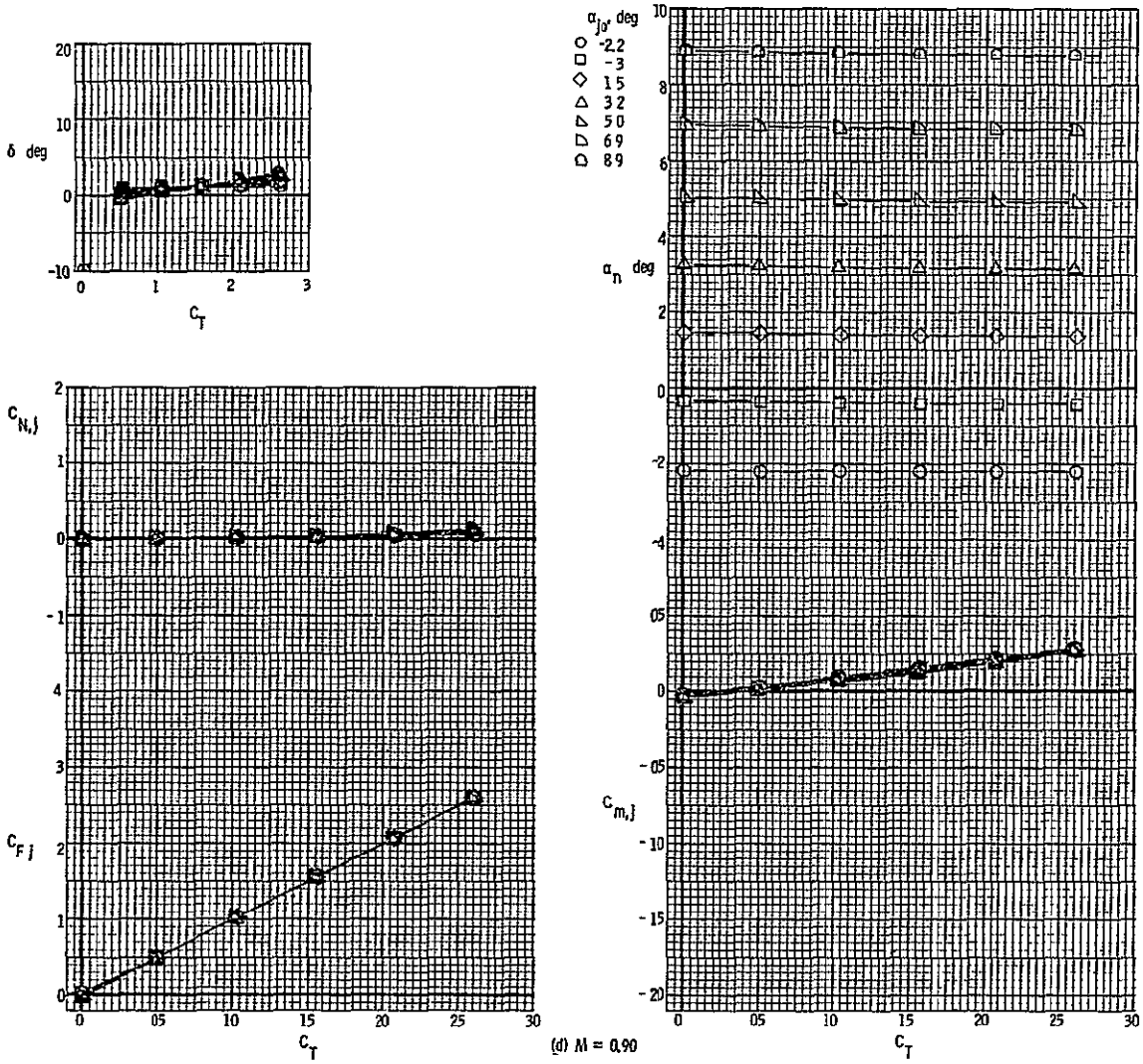

(d) M = 0.90

Figure 12 - Continued

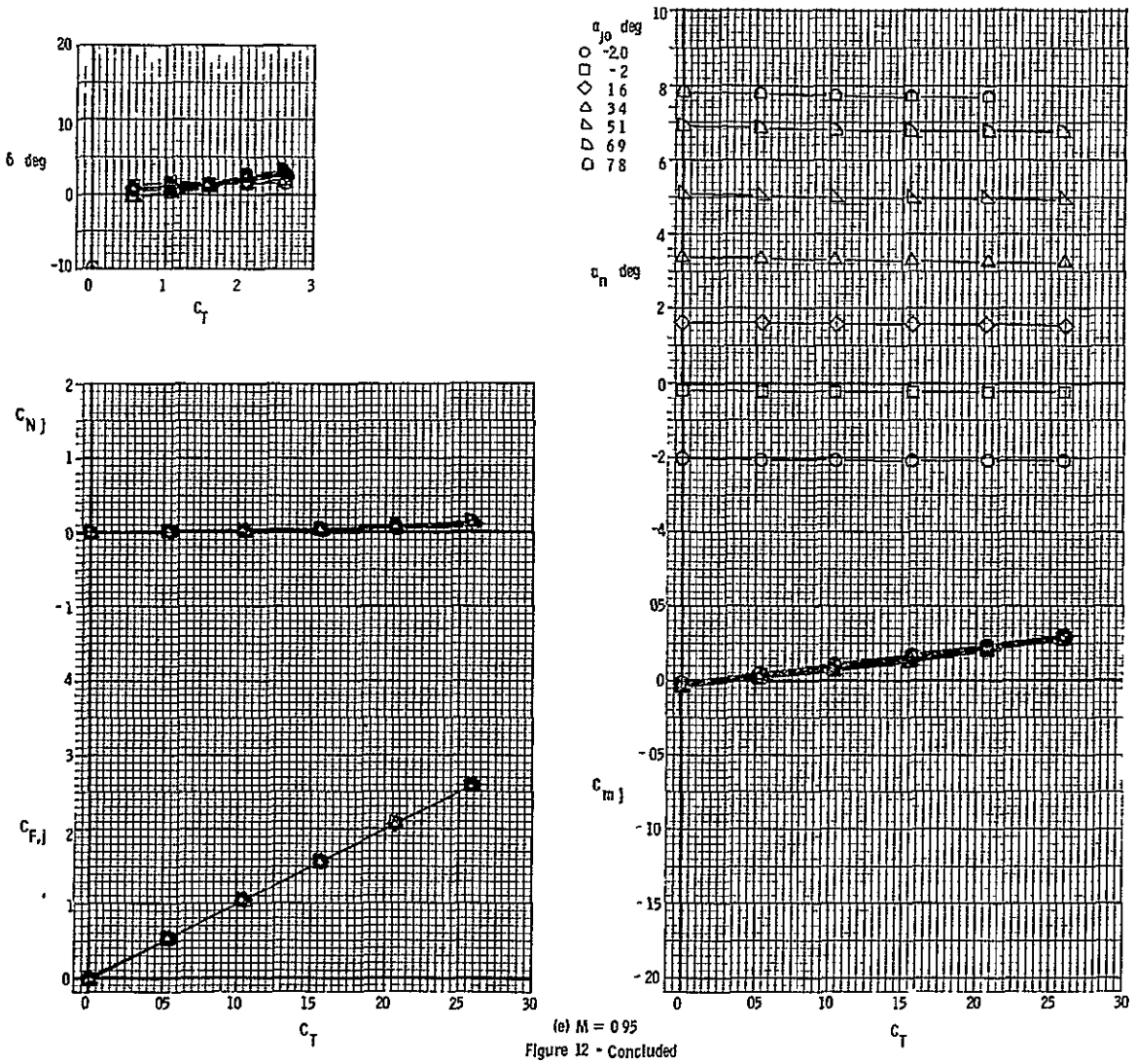

(e) M = 0.95

Figure 12 - Concluded

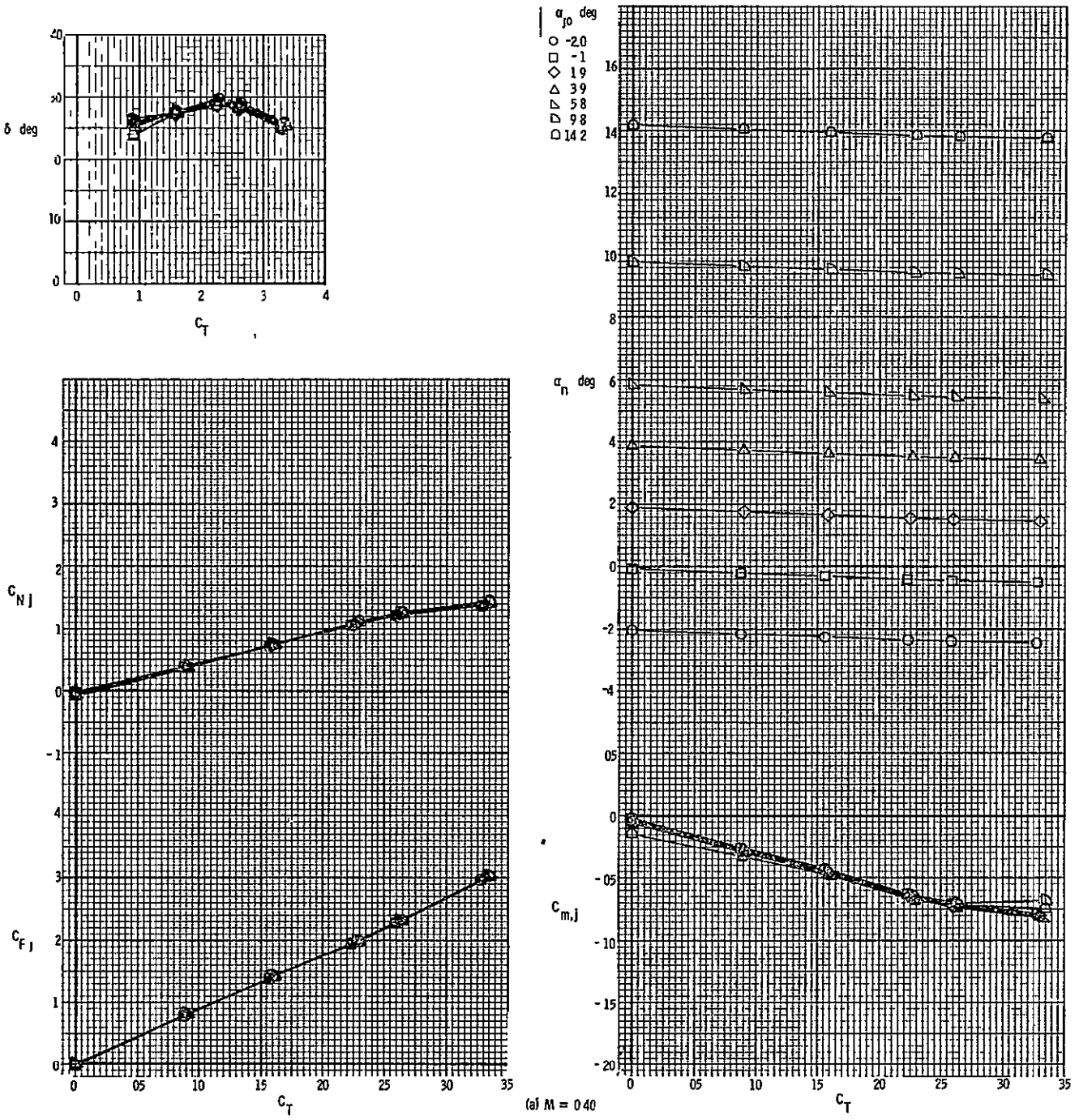

(a) M = 0.40

Figure 13 - Basic nozzle thrust characteristics $\delta_d = 30^0$

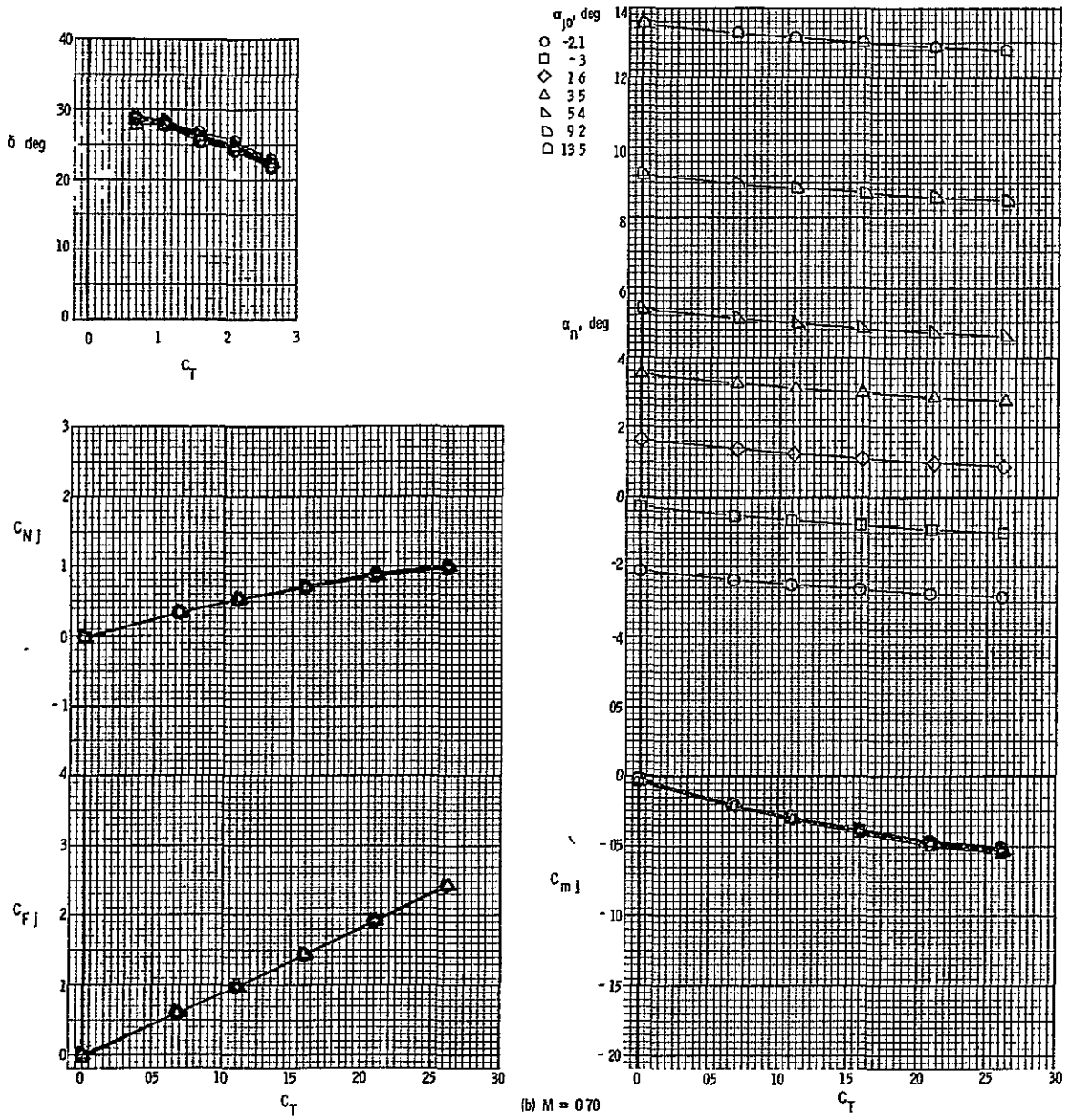

(b) M = 0.70

Figure 13 - Continued.

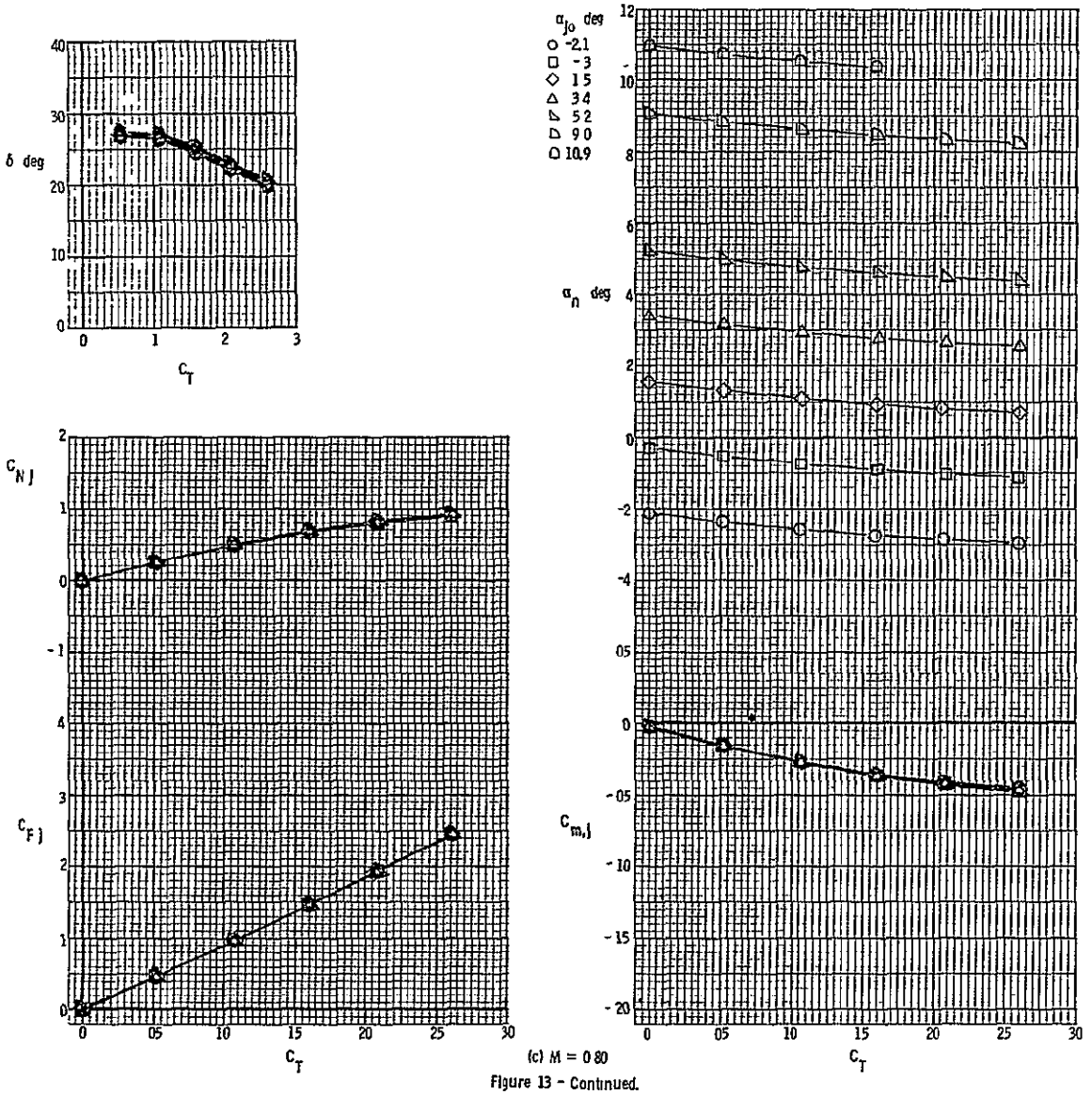

(c) M = 0.80

Figure 13 - Continued.

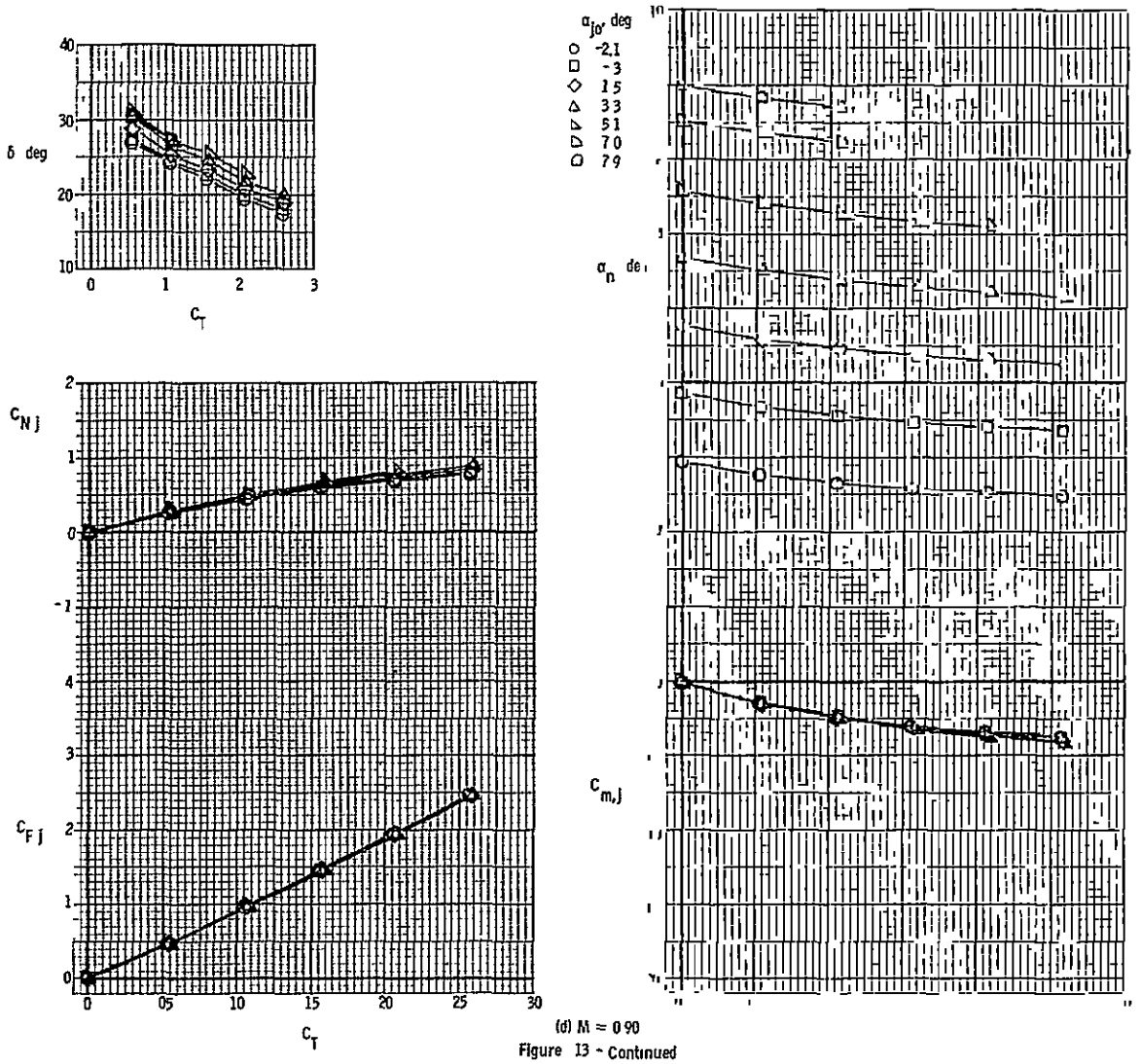

(d) M = 0.90

Figure 13 - Continued

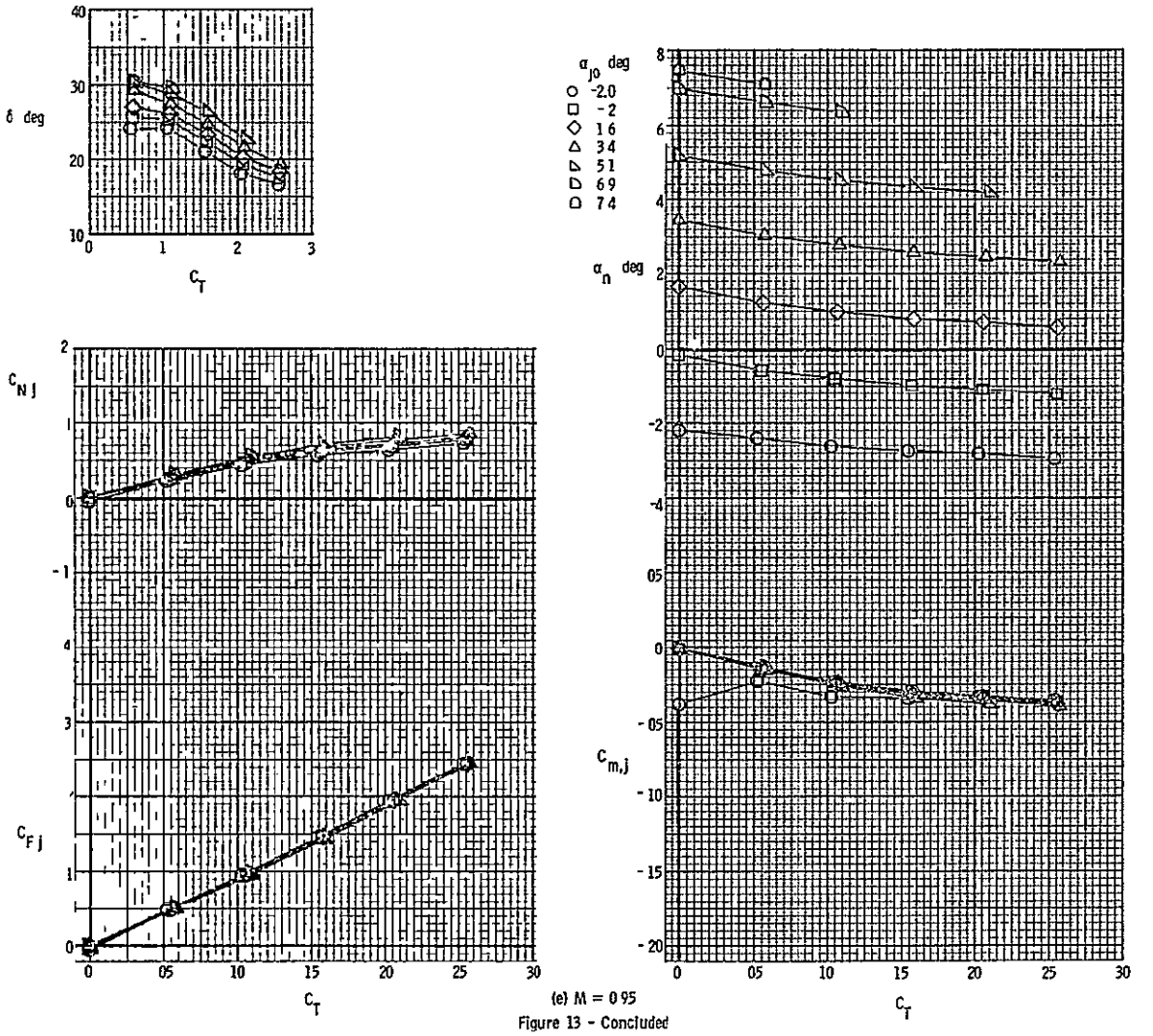

(e) M = 0 95

Figure 13 - Concluded

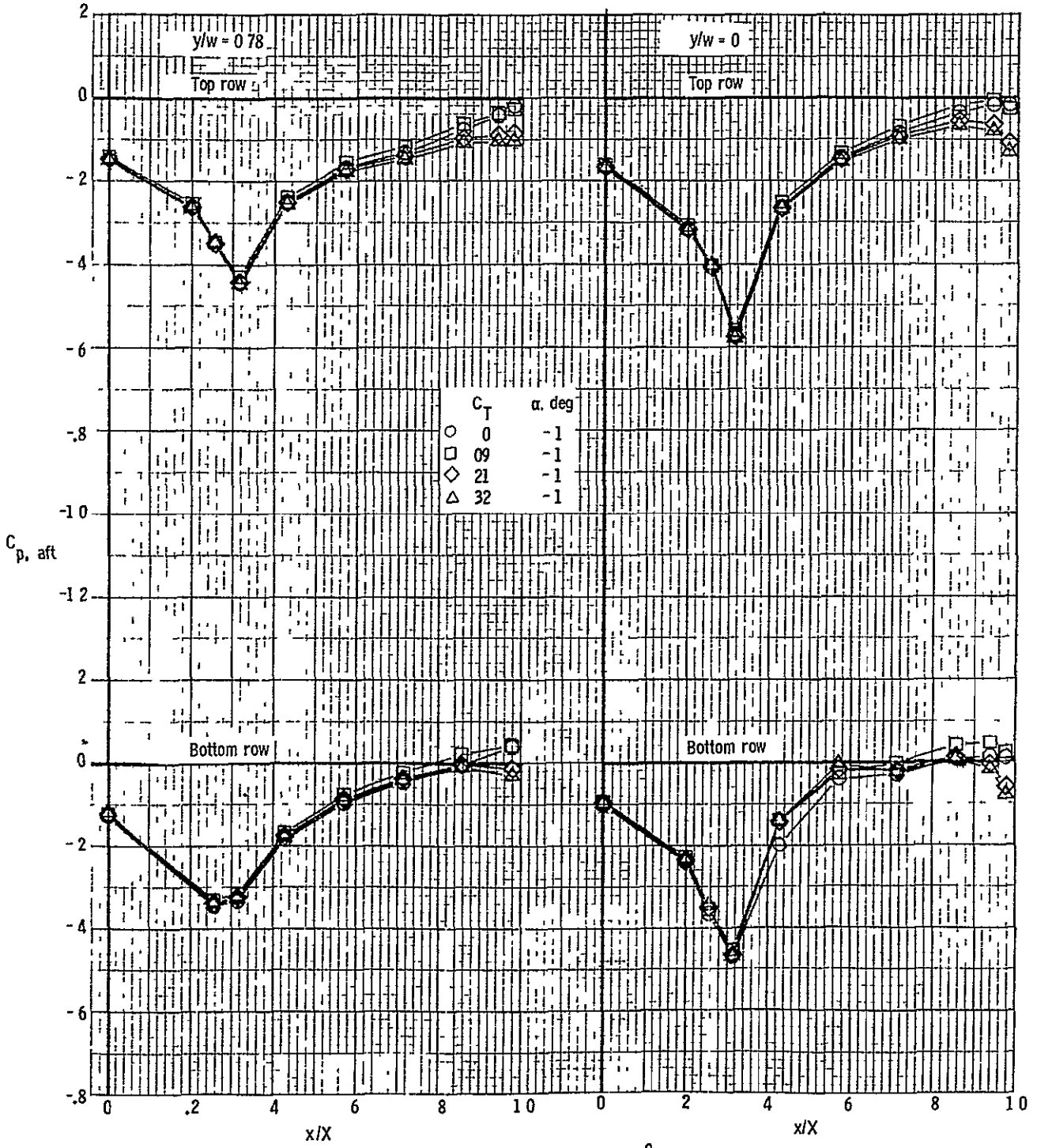

(a) M = 0 40, α = -1°

Figure 14.- Afterbody pressure distributions, $\delta_d = 0^\circ$

ORIGINAL PAGE IS
OF POOR QUALITY

ORIGINAL PAGE IS
OF POOR QUALITY

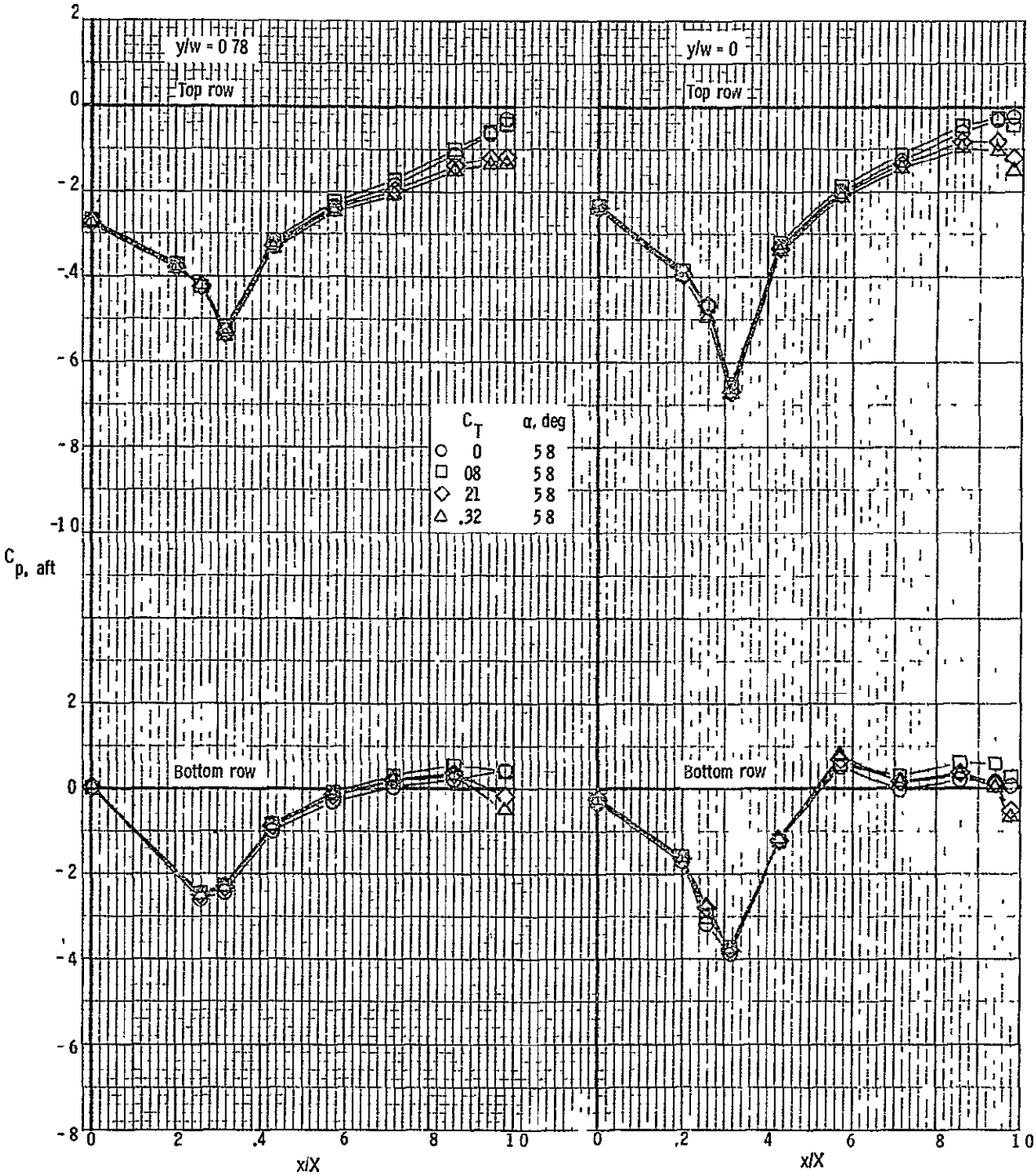

(b) M = 0 40, α = 5 8°

Figure 14 - Continued

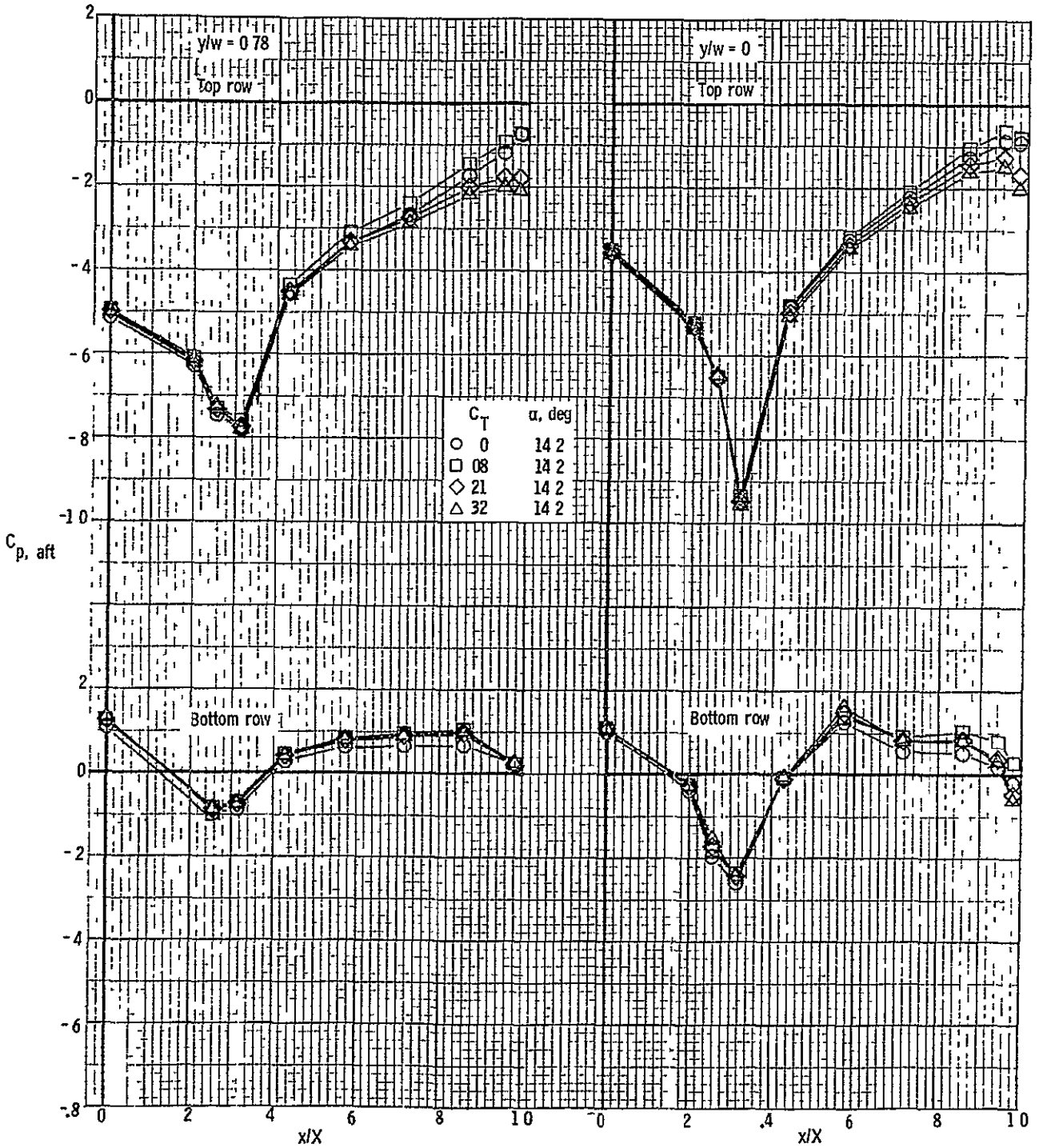

(c) M = 0 40, α = 14 2°

Figure 14 – Continued

ORIGINAL PAGE IS
OF POOR QUALITY

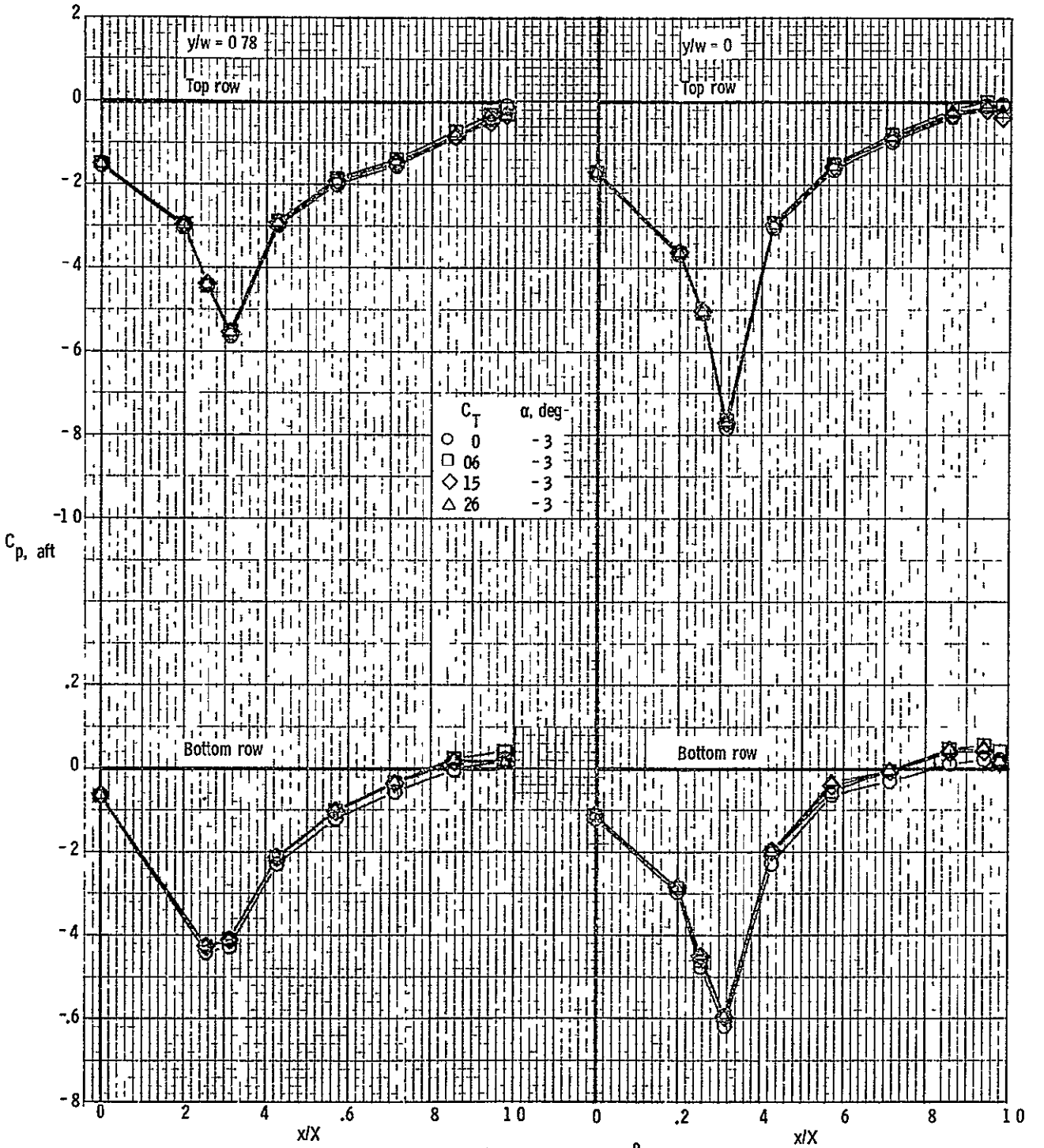

(d) M = 0 70, α = -3°

Figure 14 - Continued

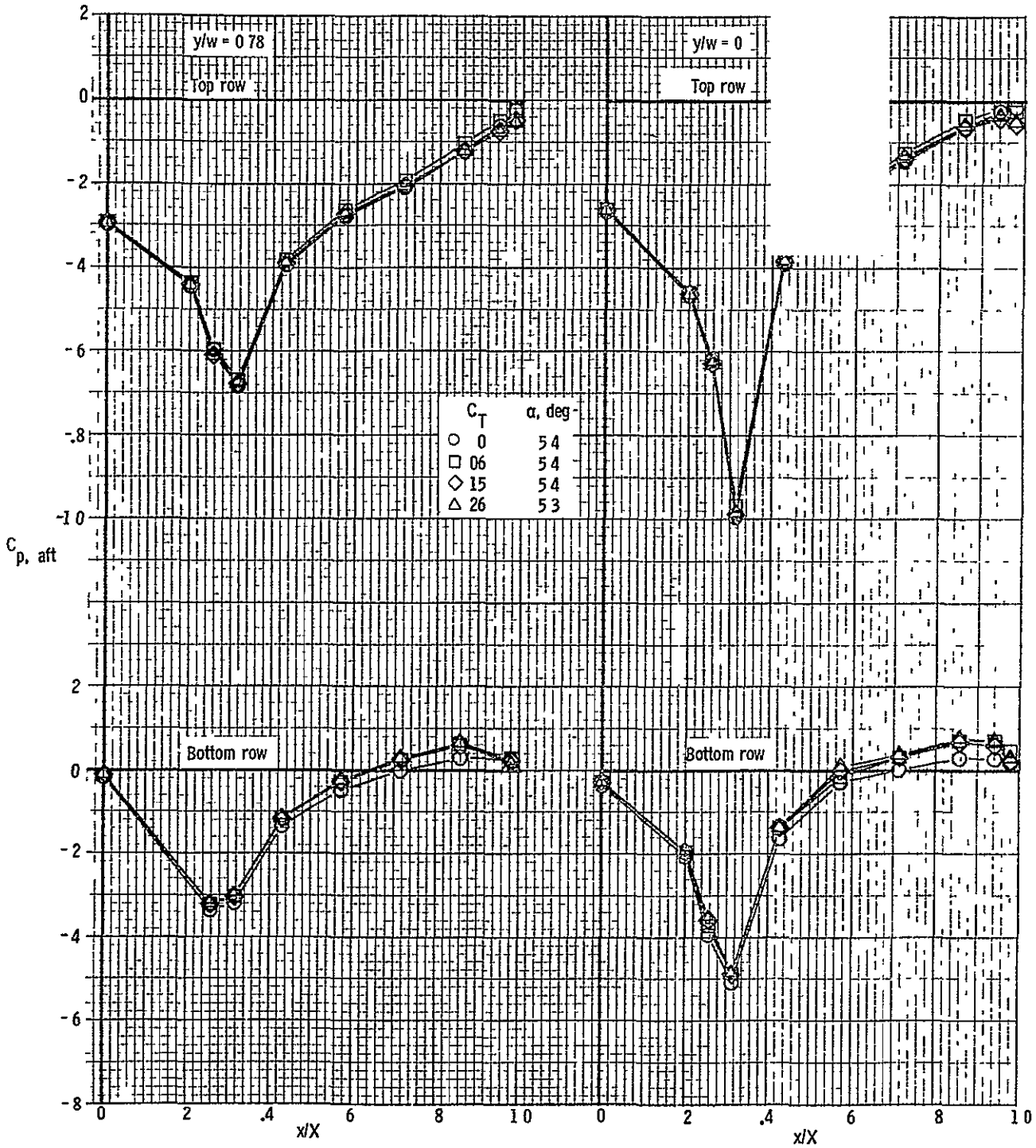

(e) M = 0 70, α ~ 5 4°

Figure 14 - Continued

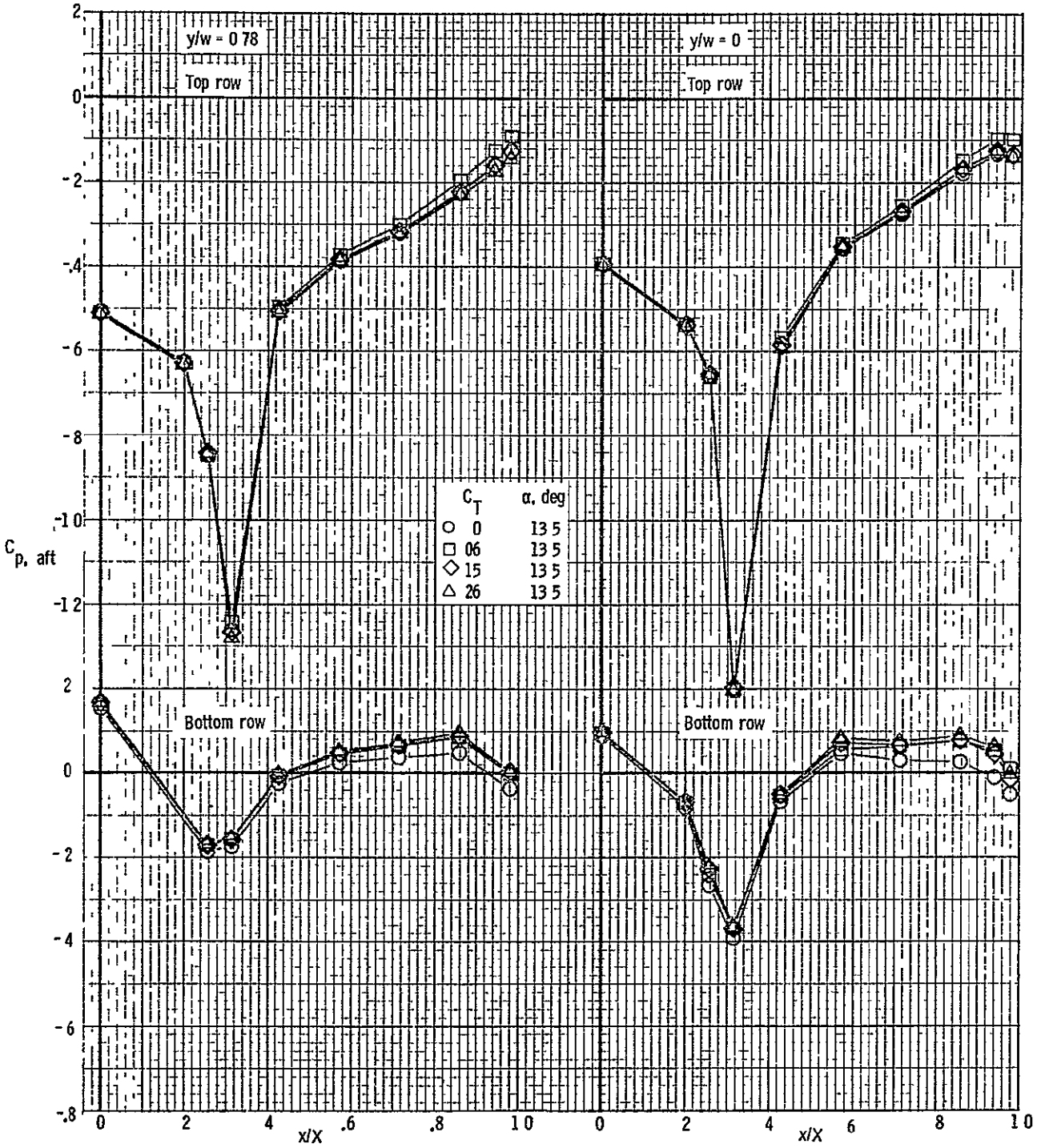

(f) M = 0 70, α = 13 5°

Figure 14 - Continued

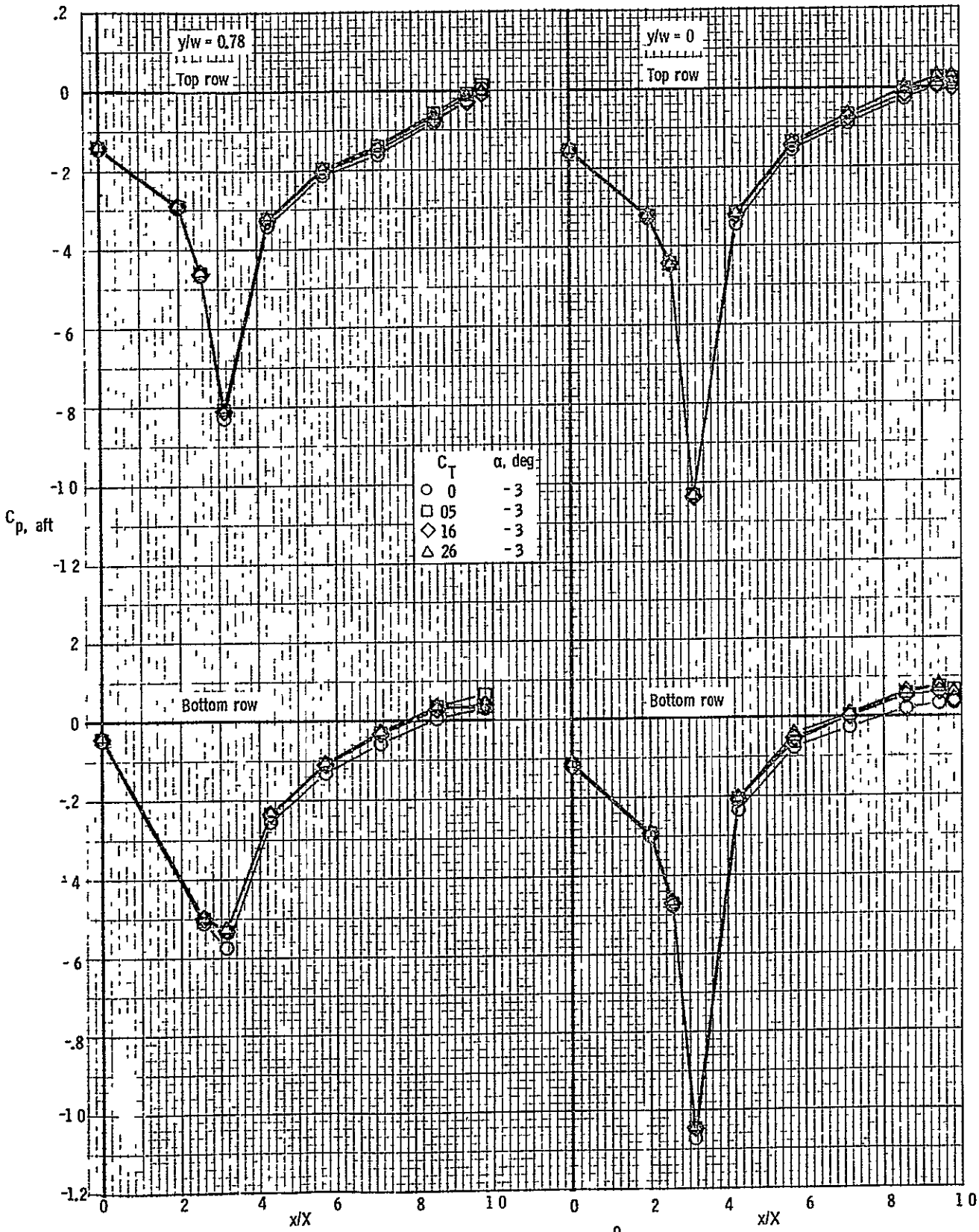

(g) M = 0 80, α = -3°

Figure 14 - Continued.

ORIGINAL PAGE IS
OF POOR QUALITY

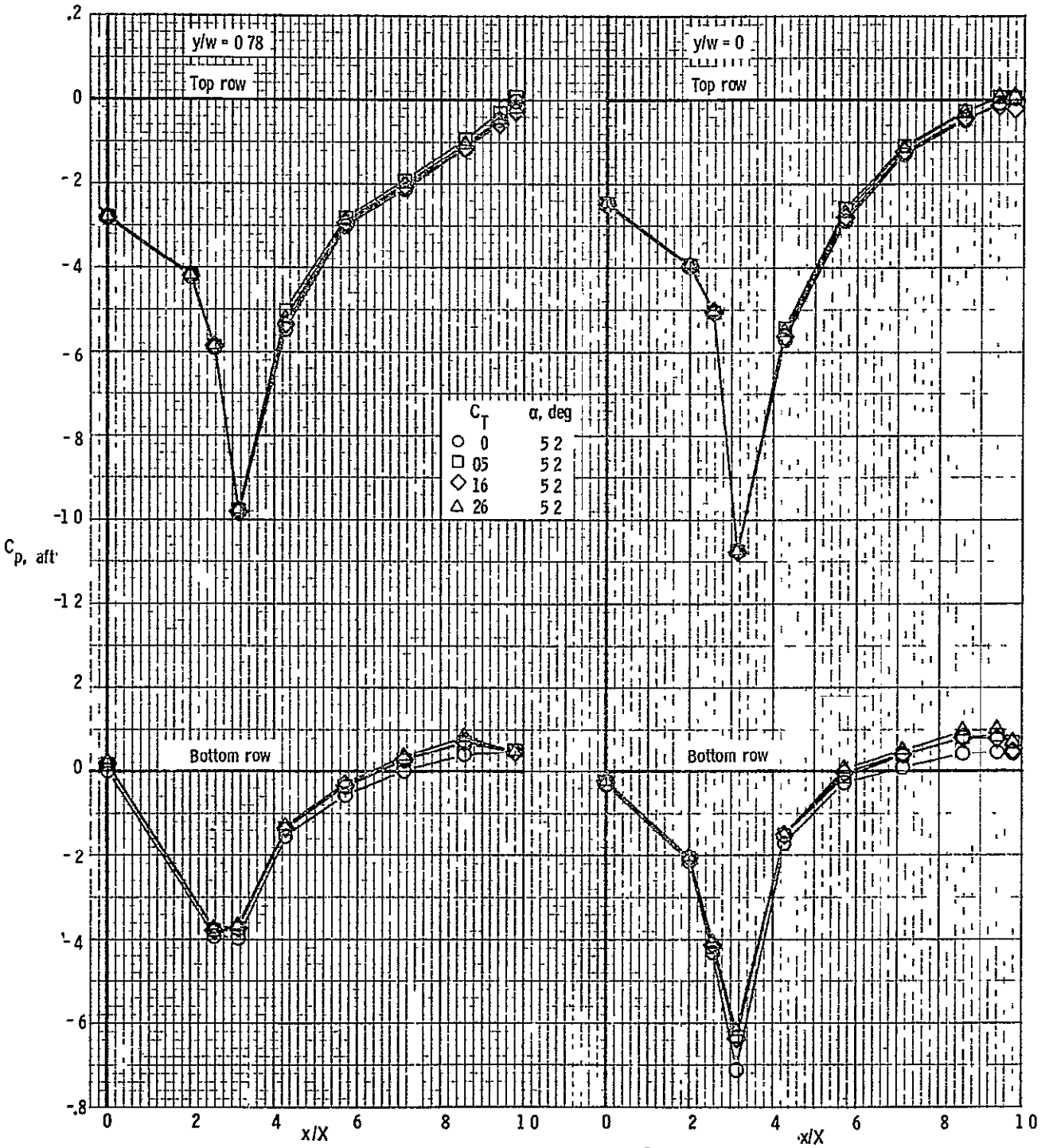

(h) M = 0 80, α = 5 2°

Figure 14 - Continued

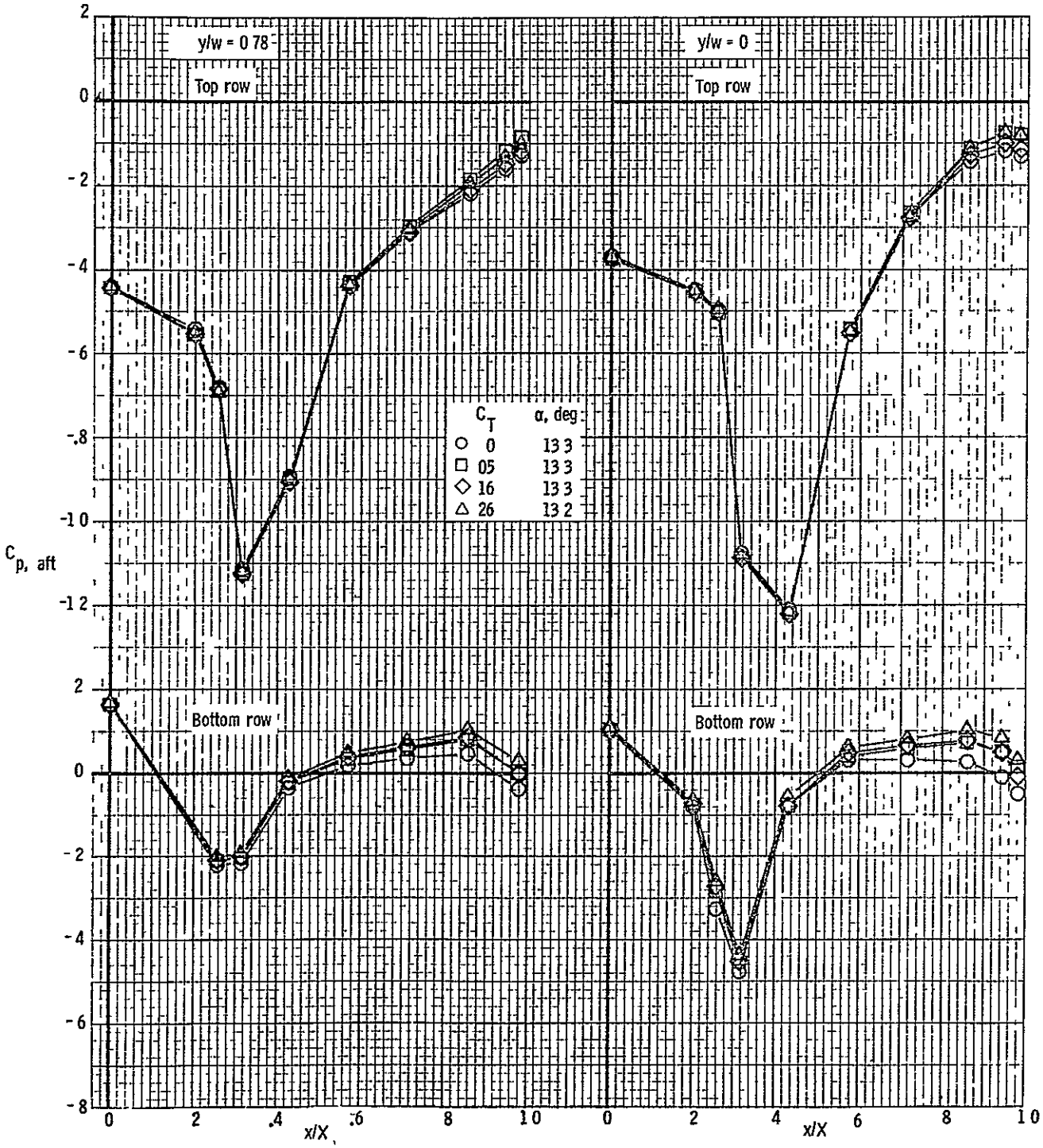

(i) M = 0 80, α ~ 13 3°

Figure 14.- Continued

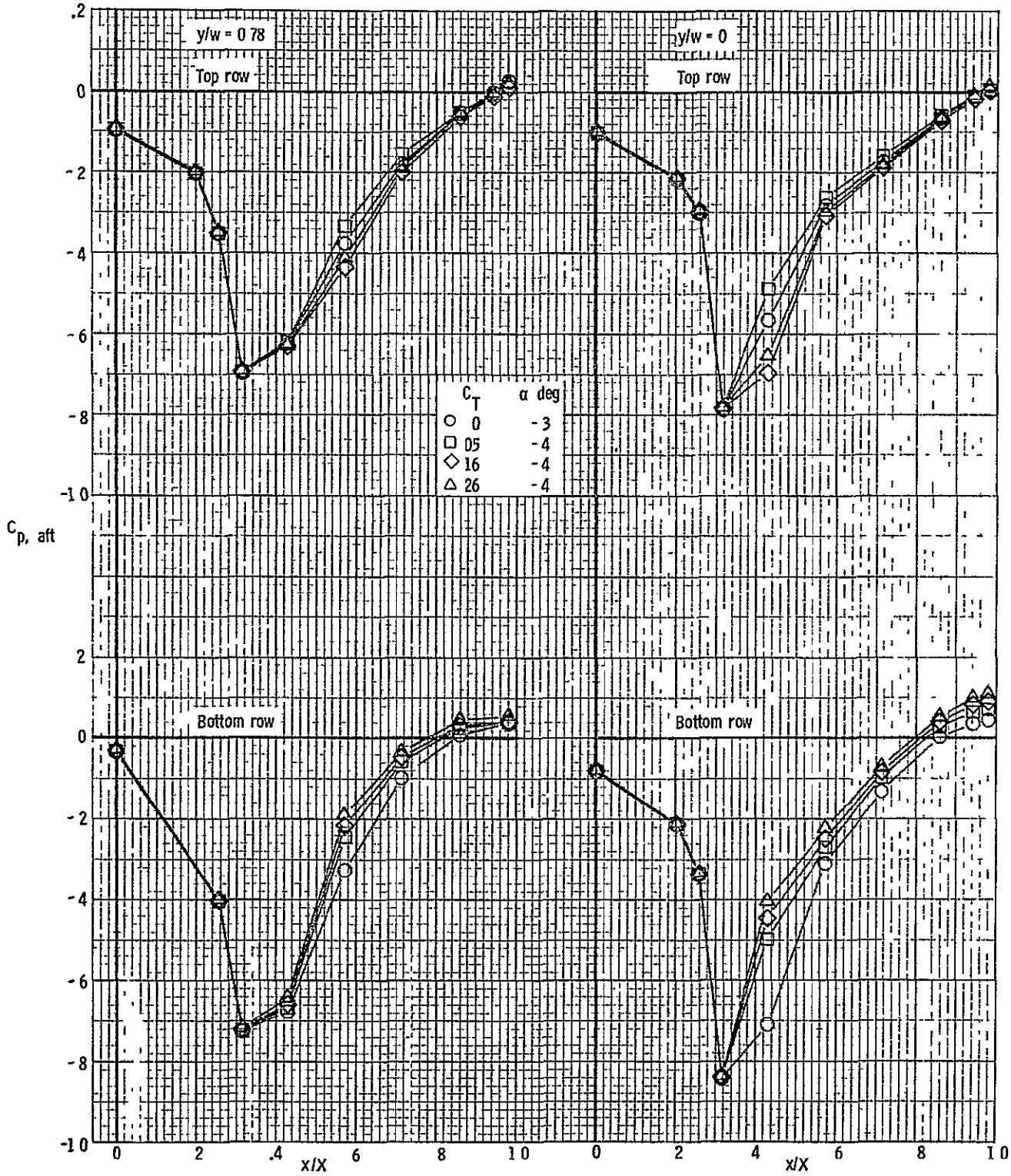

(j) M = 0 90, α ~ -4°

Figure 14 - Continued

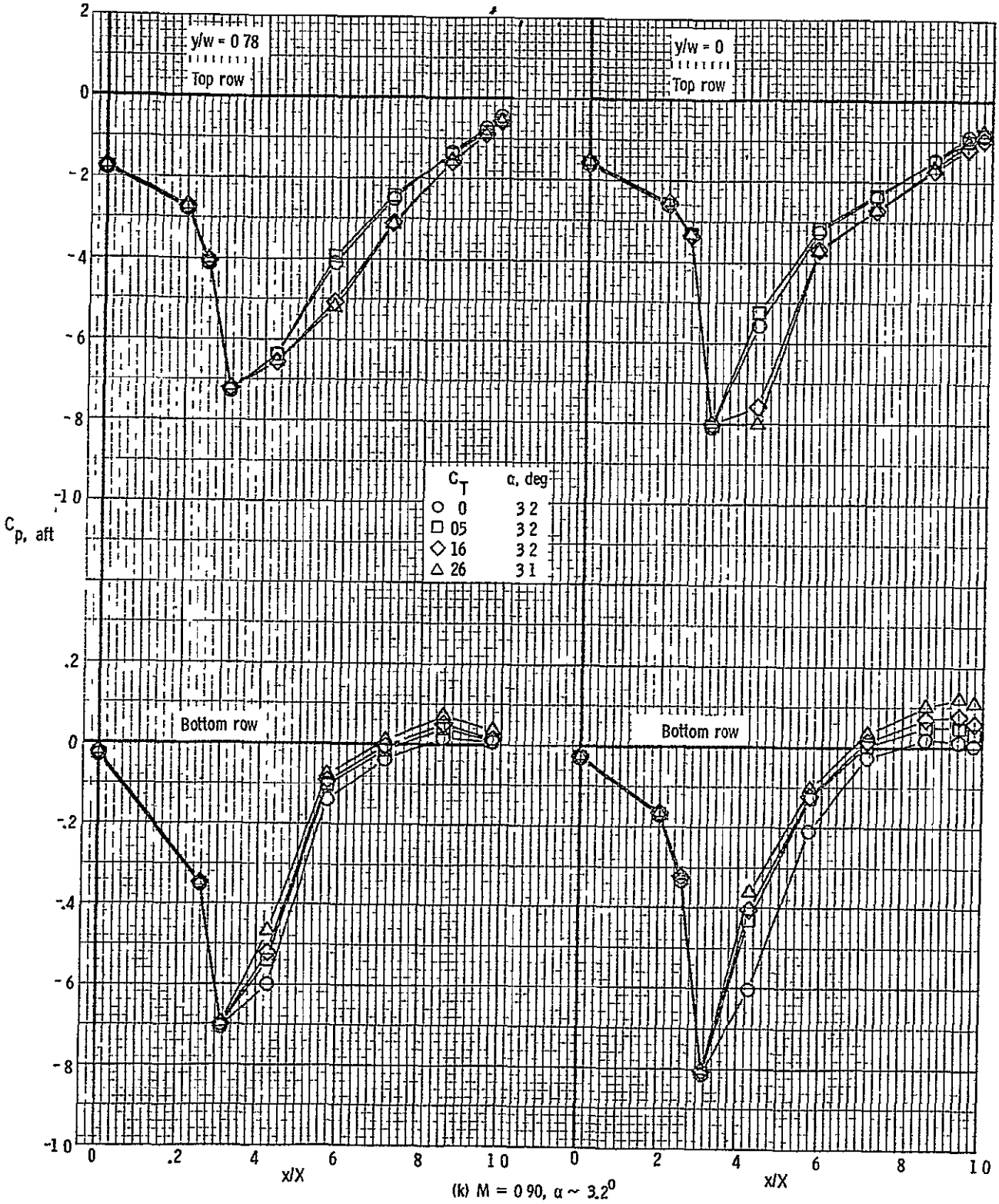

(k) M = 0 90, α ~ 3.2°

Figure 14 - Continued.

ORIGINAL PAGE IS
OF POOR QUALITY

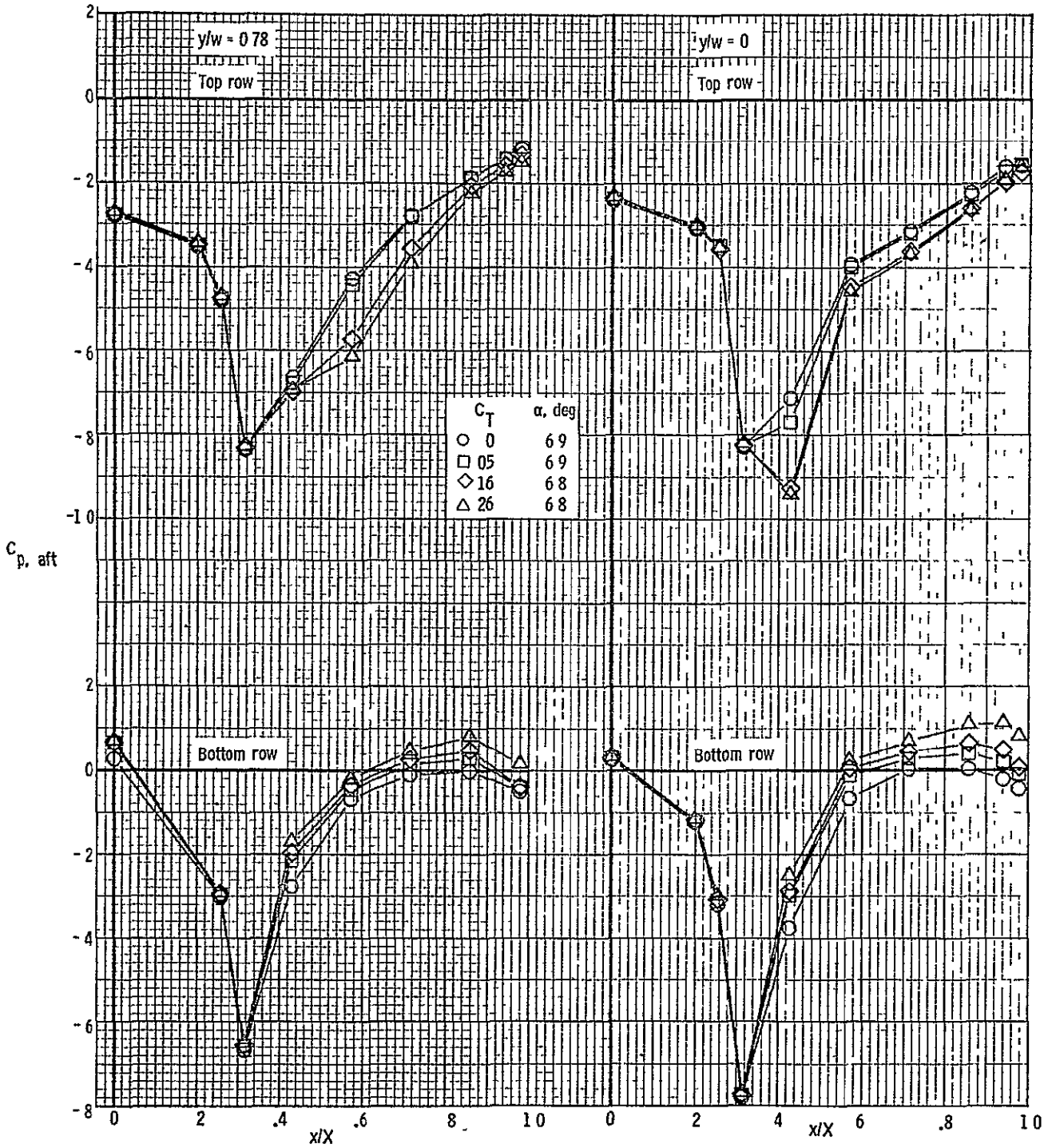

(l) M = 0 90, α ~ 6 8°

Figure 14 - Continued

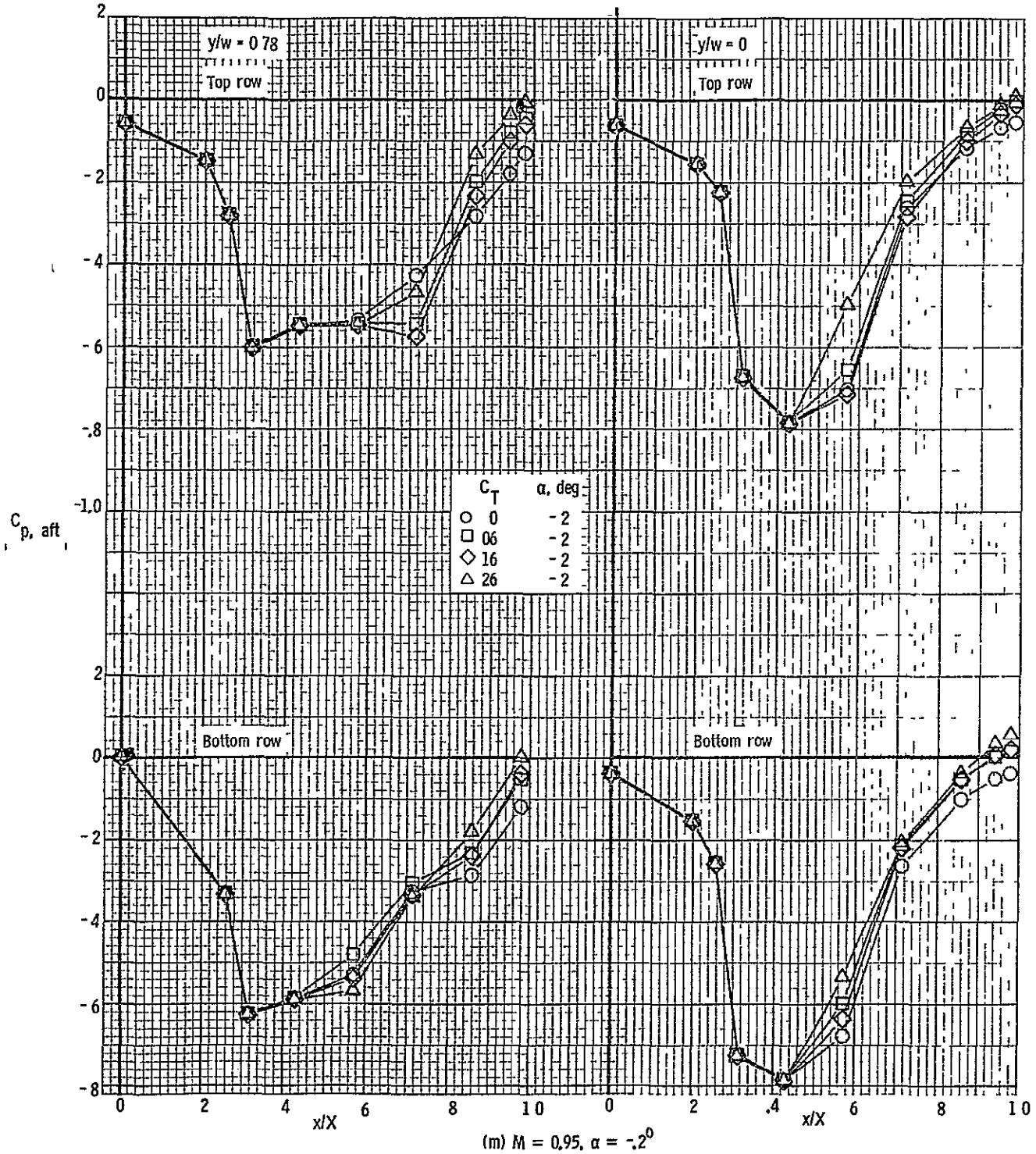

(m) M = 0.95, α = -.2°

Figure 14 - Continued

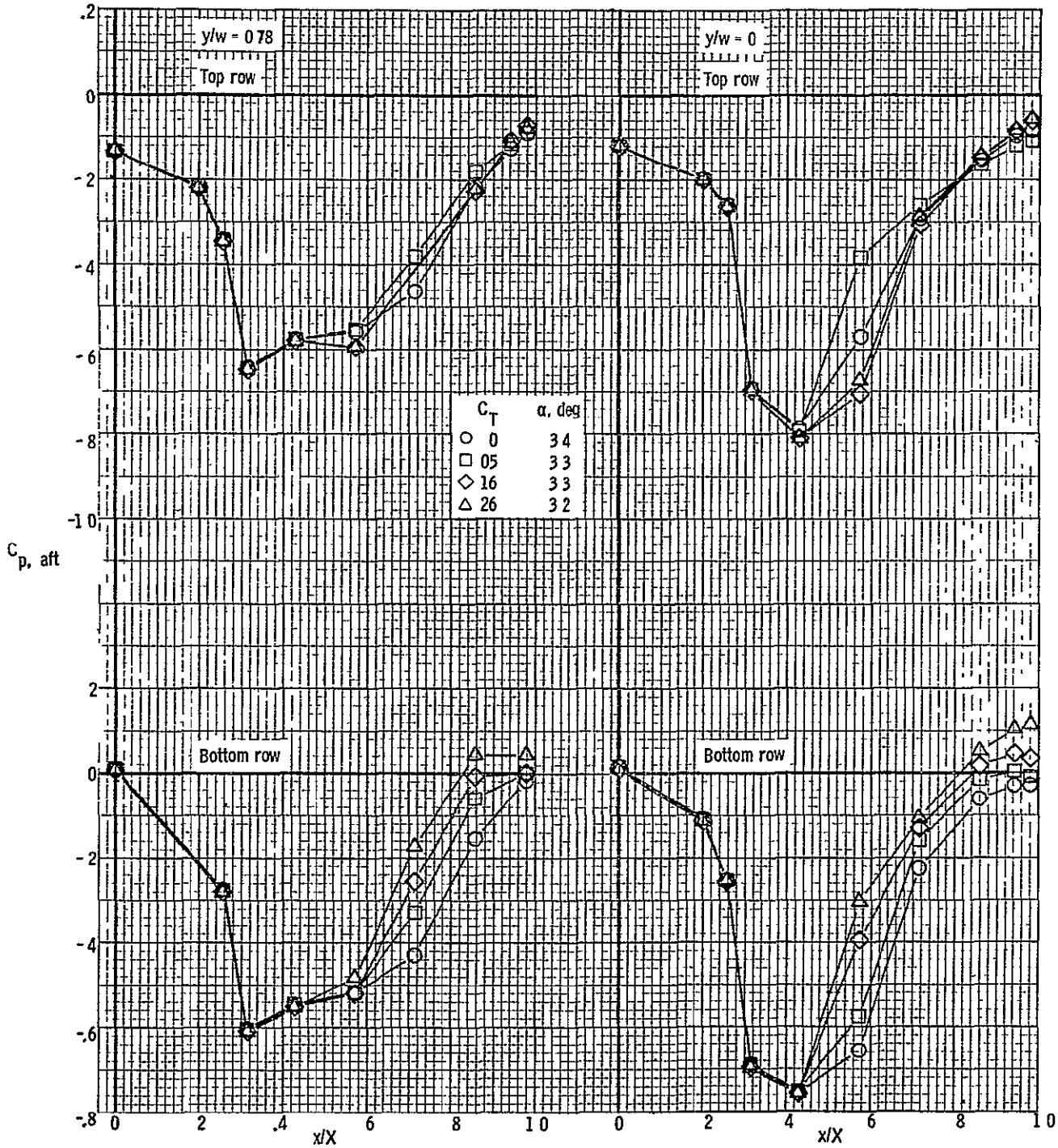

(n) M = 0 95, α ~ 3·3°

Figure 14 - Continued

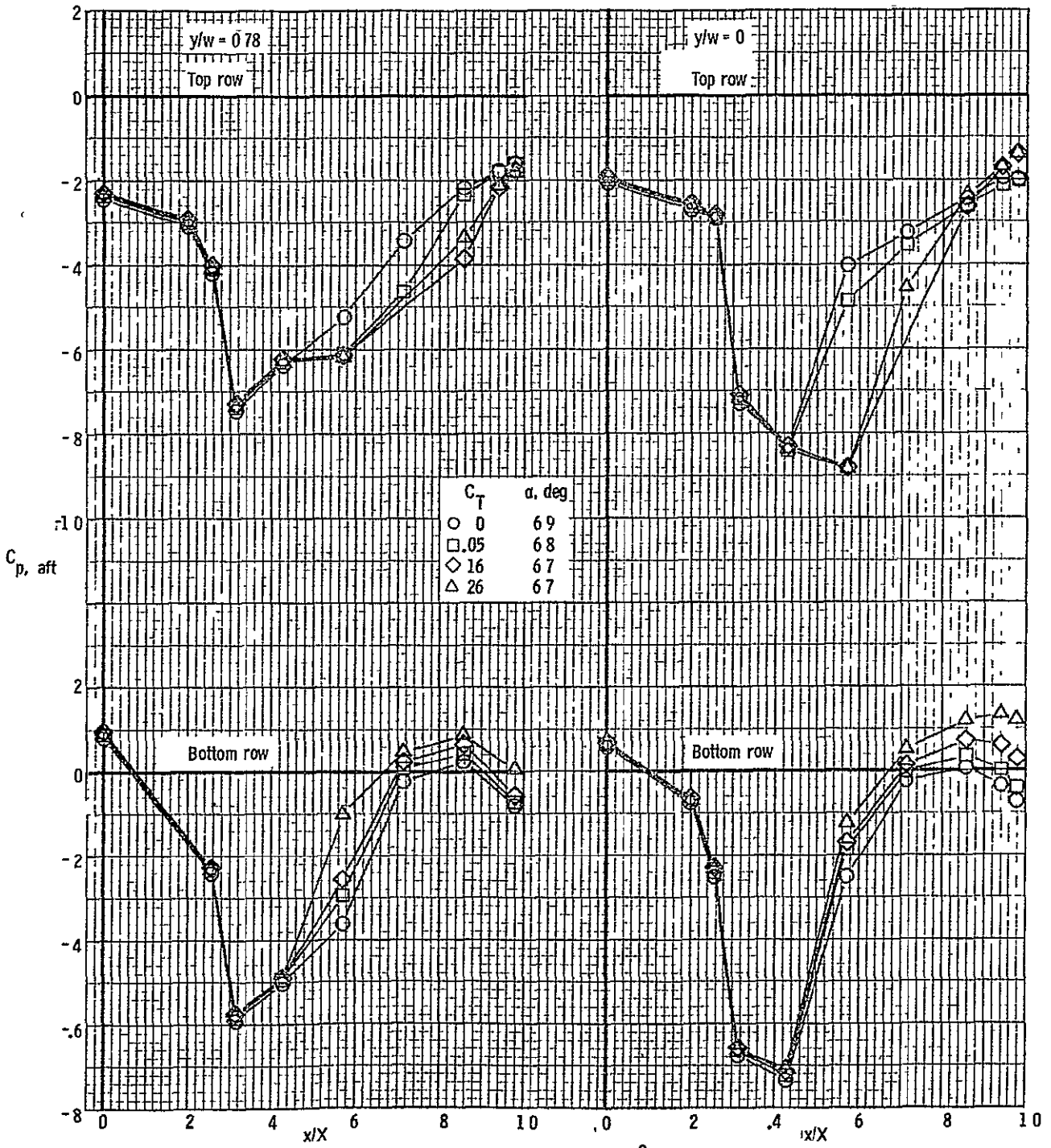

(o) M = 0.95, α ~ 6.8°

Figure 14.- Concluded

ORIGINAL PAGE IS
OF POOR QUALITY

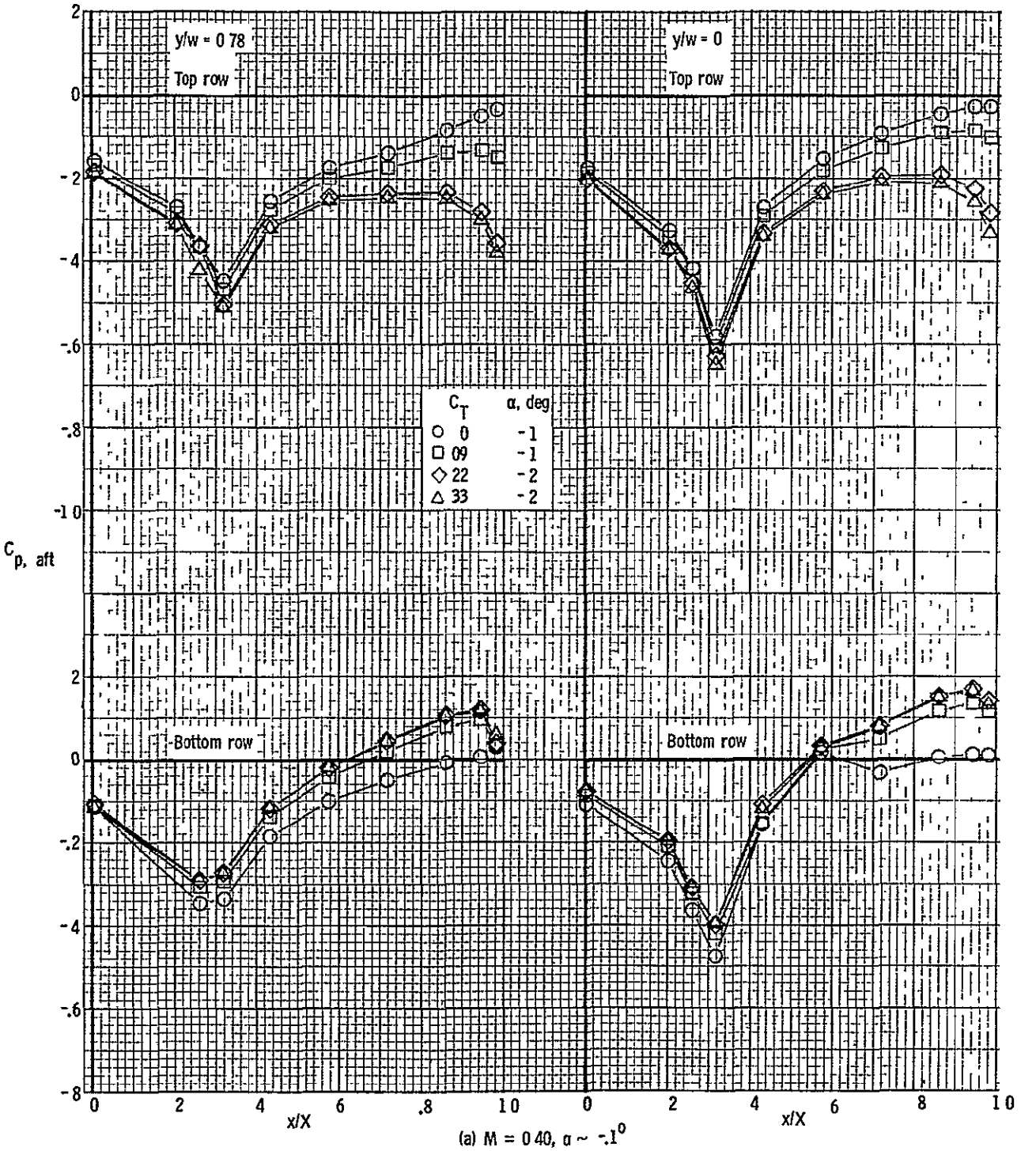

(a) M = 0 40, α ~ -.1°

Figure 15.- Afterbody pressure distributions, $\delta_d = 30^\circ$

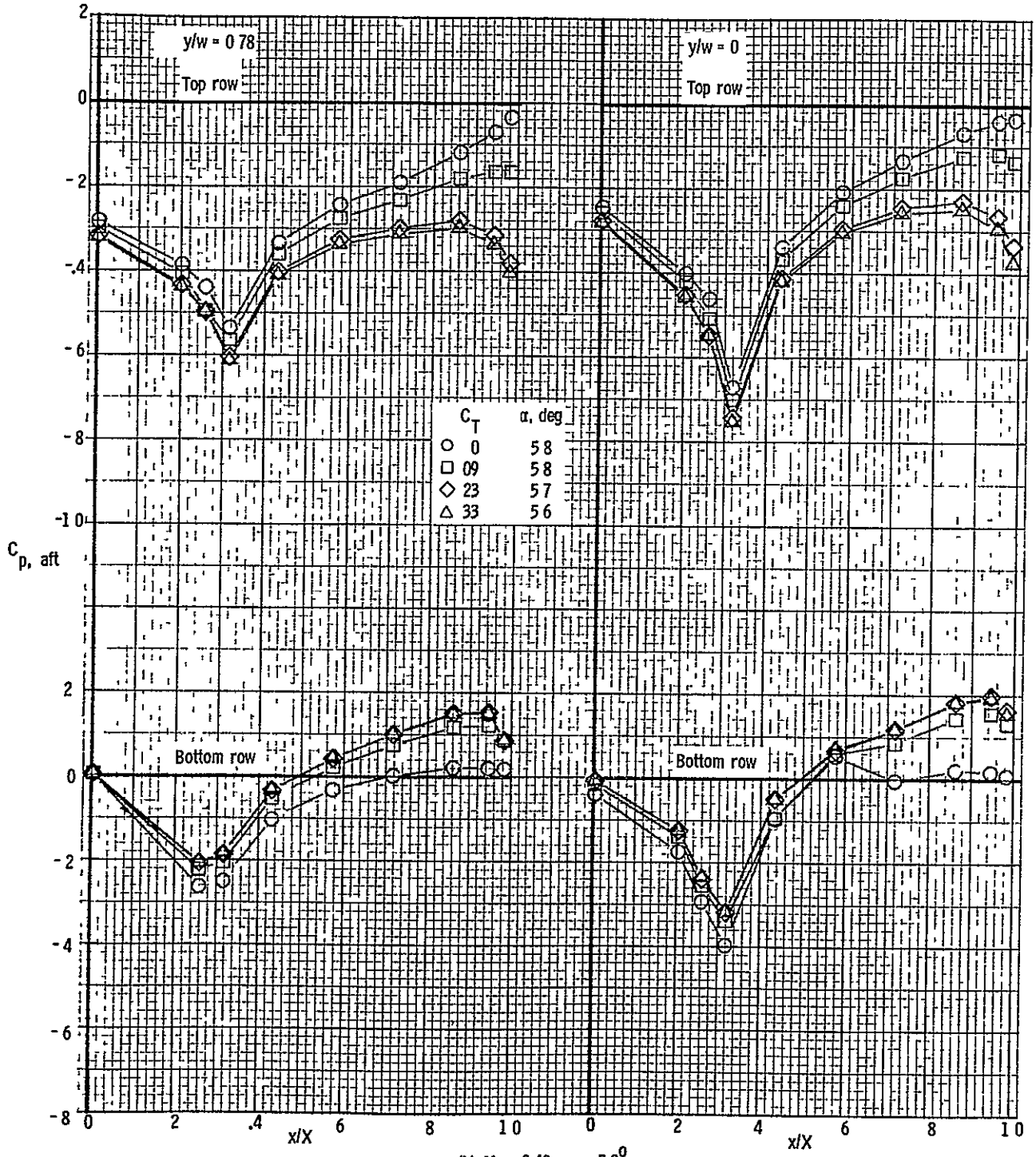

(b) M = 0.40, α ~ 5.8°

Figure 15.- Continued.

ORIGINAL PAGE IS
OF POOR QUALITY

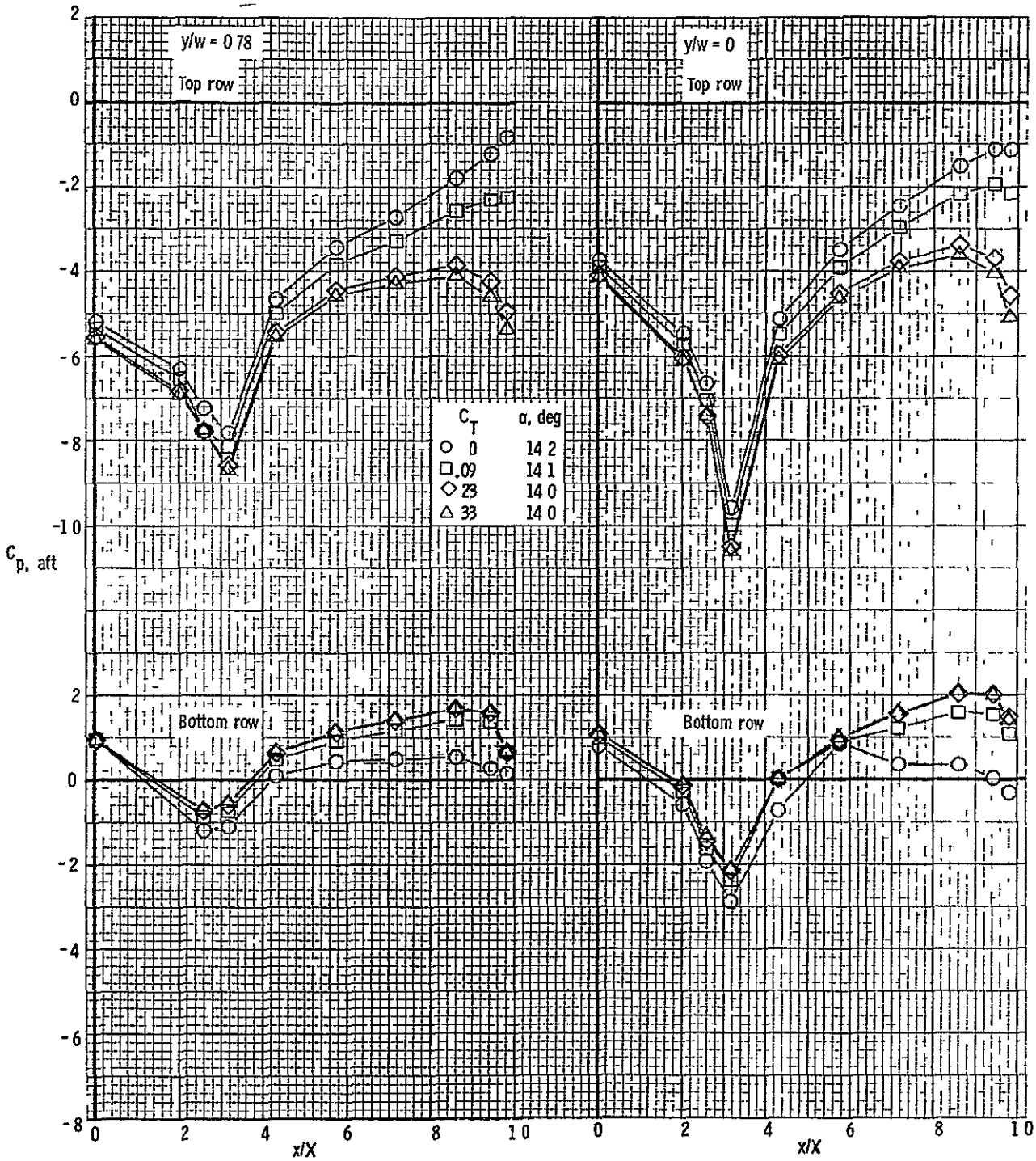

(c) M = 0.40, α ~ 14.1°

Figure 15.- Continued

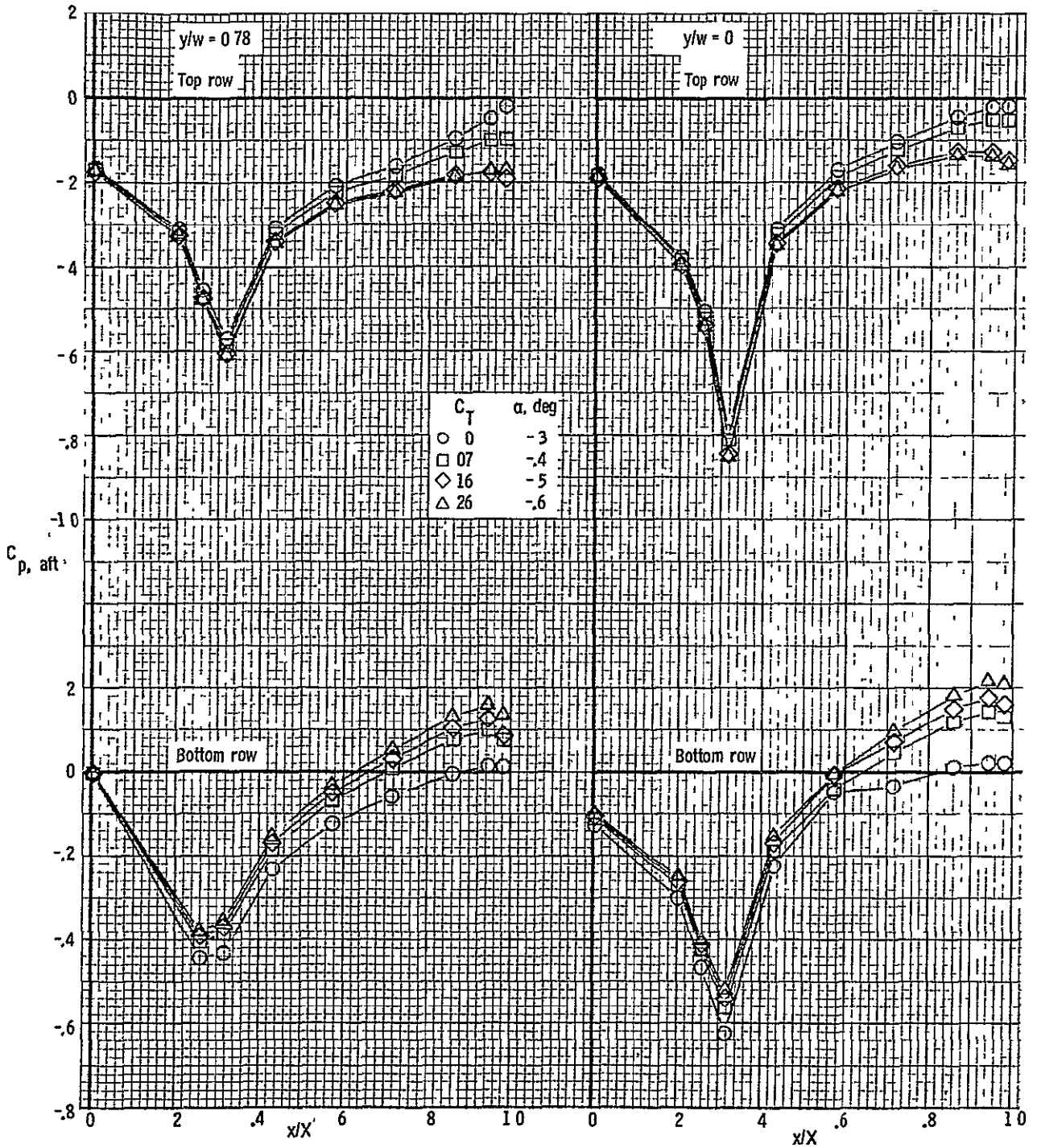

(d) M = 0 70, α ~ -4°

Figure 15 - Continued.

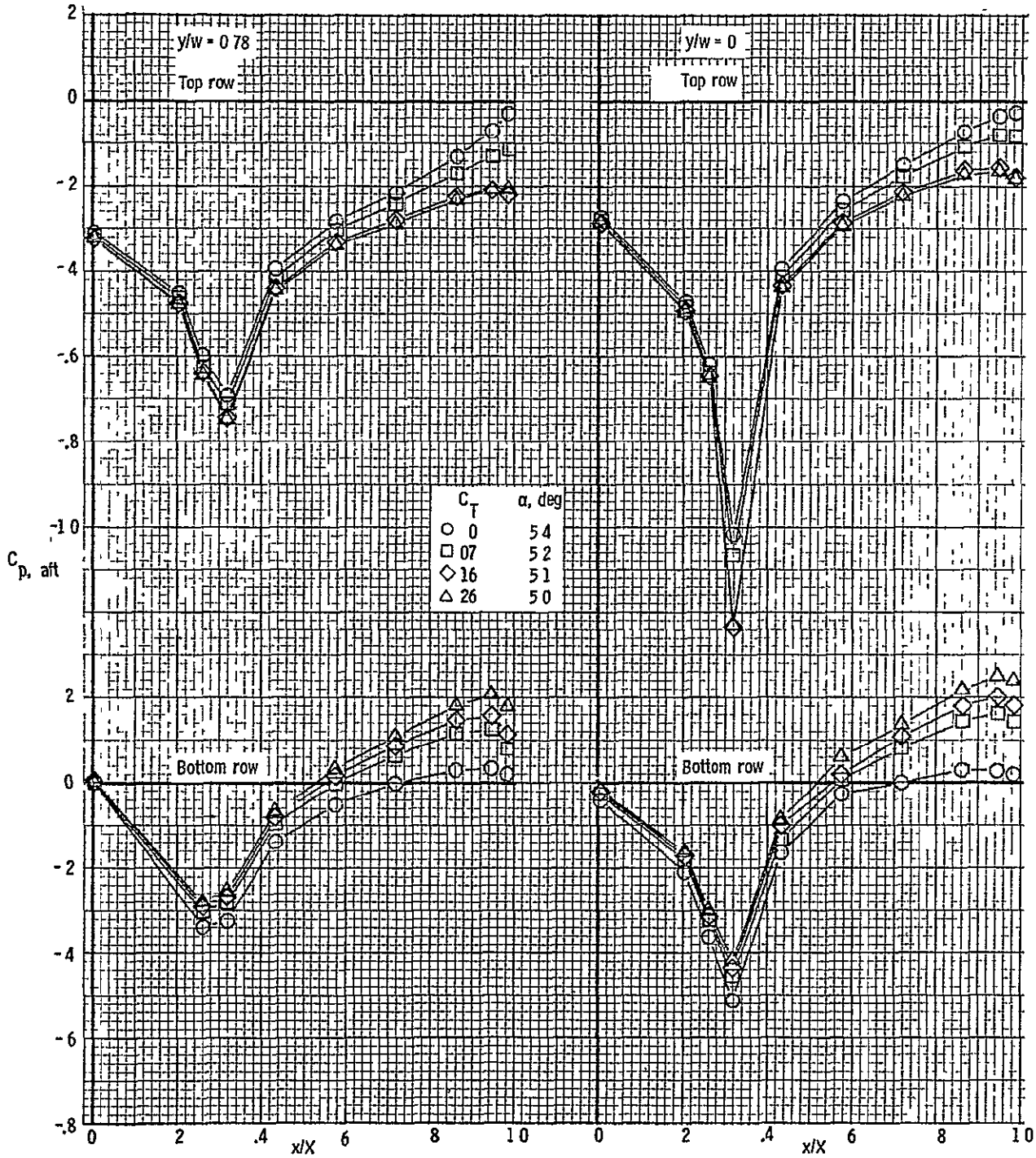

(e) M = 0 70, α ~ 5 2°

Figure 15.- Continued

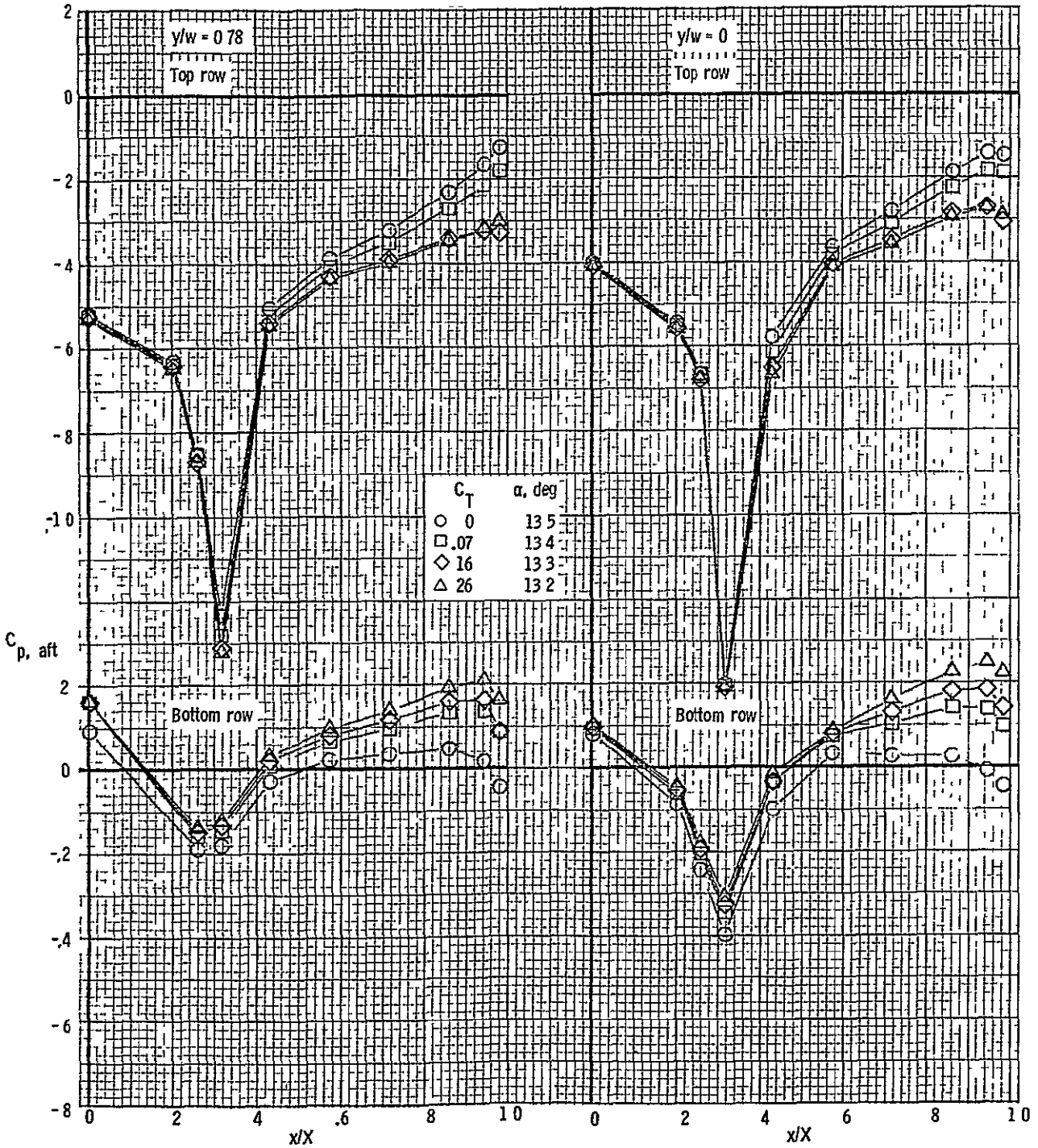

(f) M = 0 70, α ~ 13 2°

Figure 15 - Continued

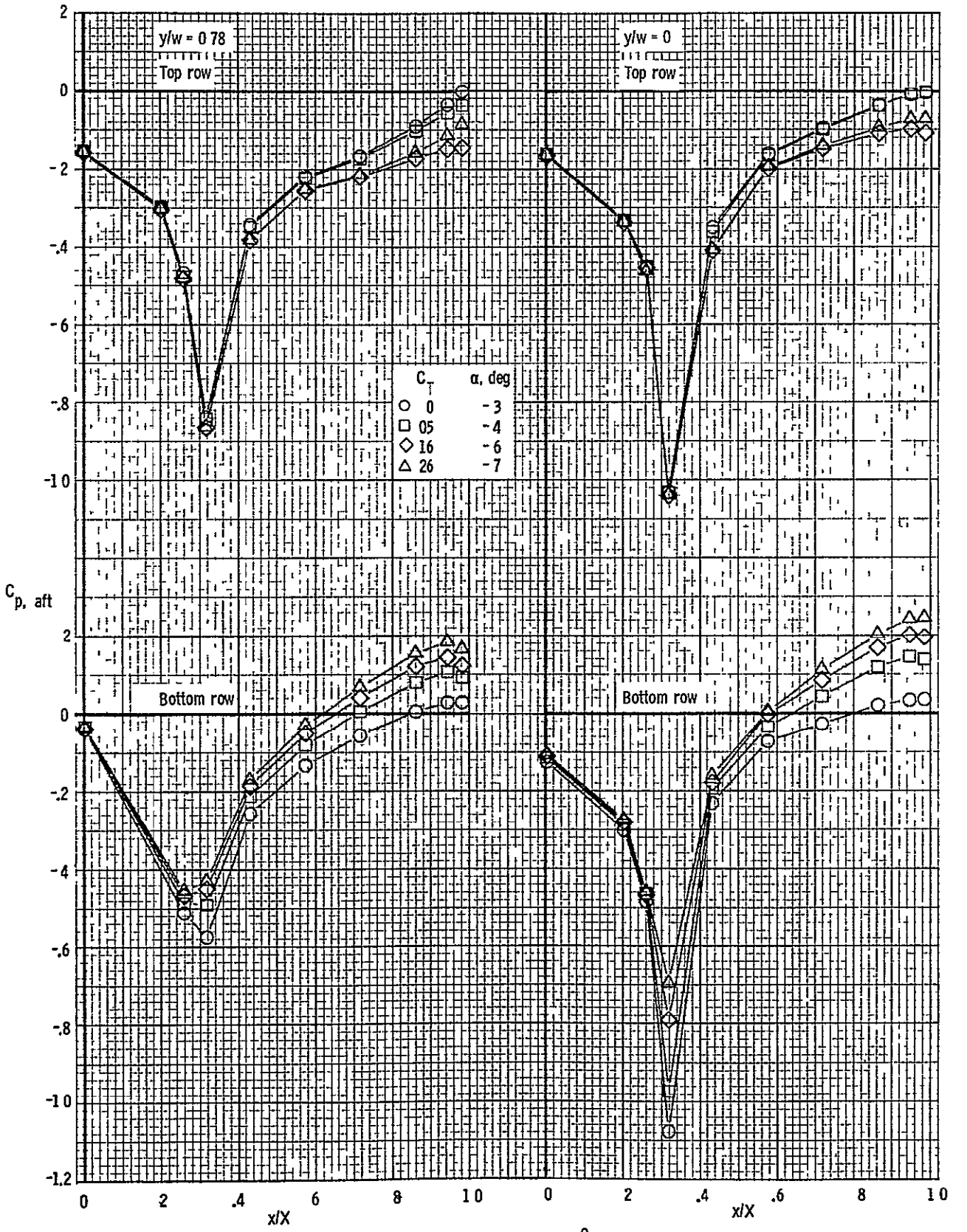

(g) M = 0 80, α ~ -.4°

Figure 15. - Continued

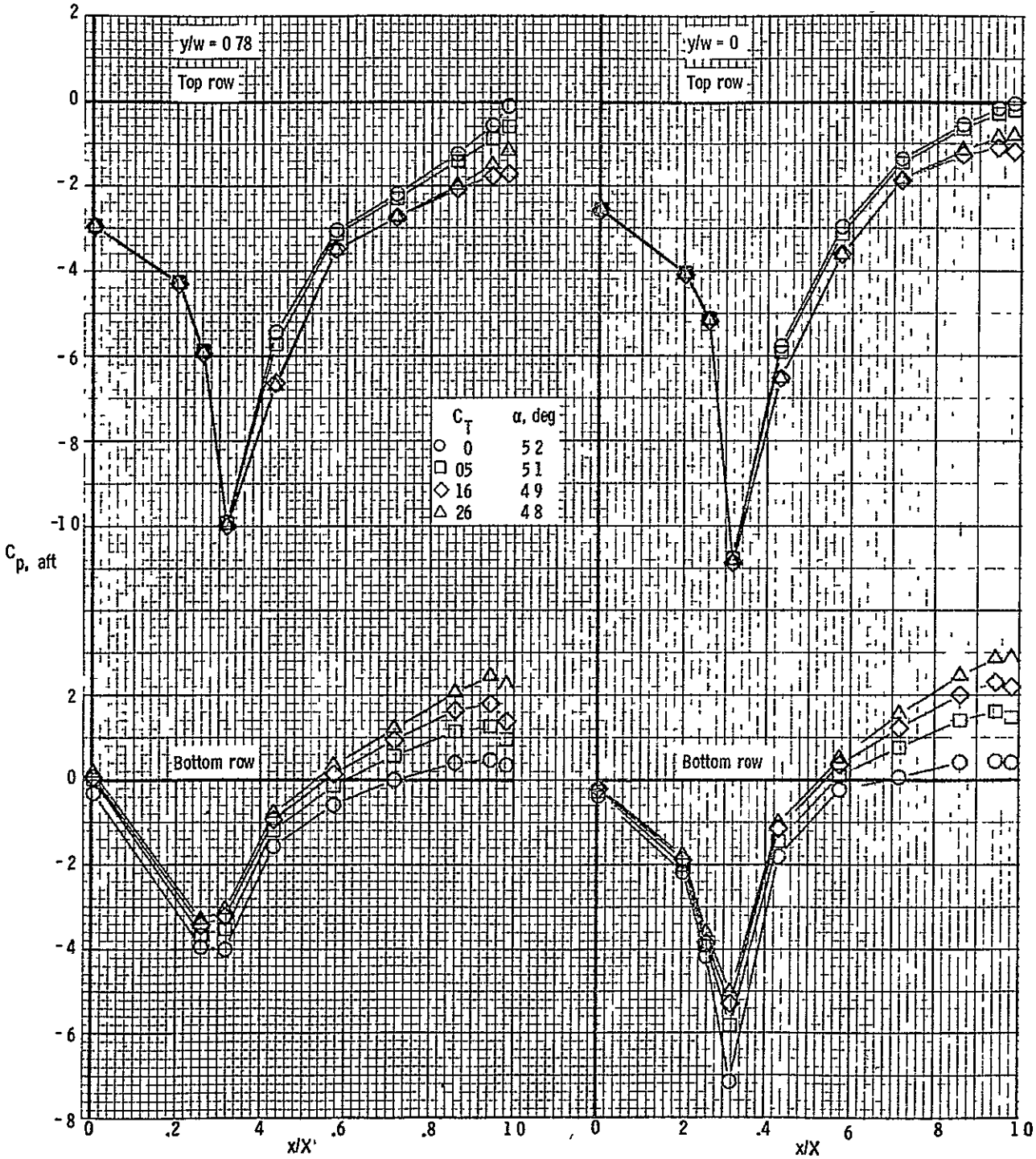

(h) M = 0 80, α ~ 5 1°

Figure 15.- Continued

ORIGINAL PAGE IS
OF POOR QUALITY

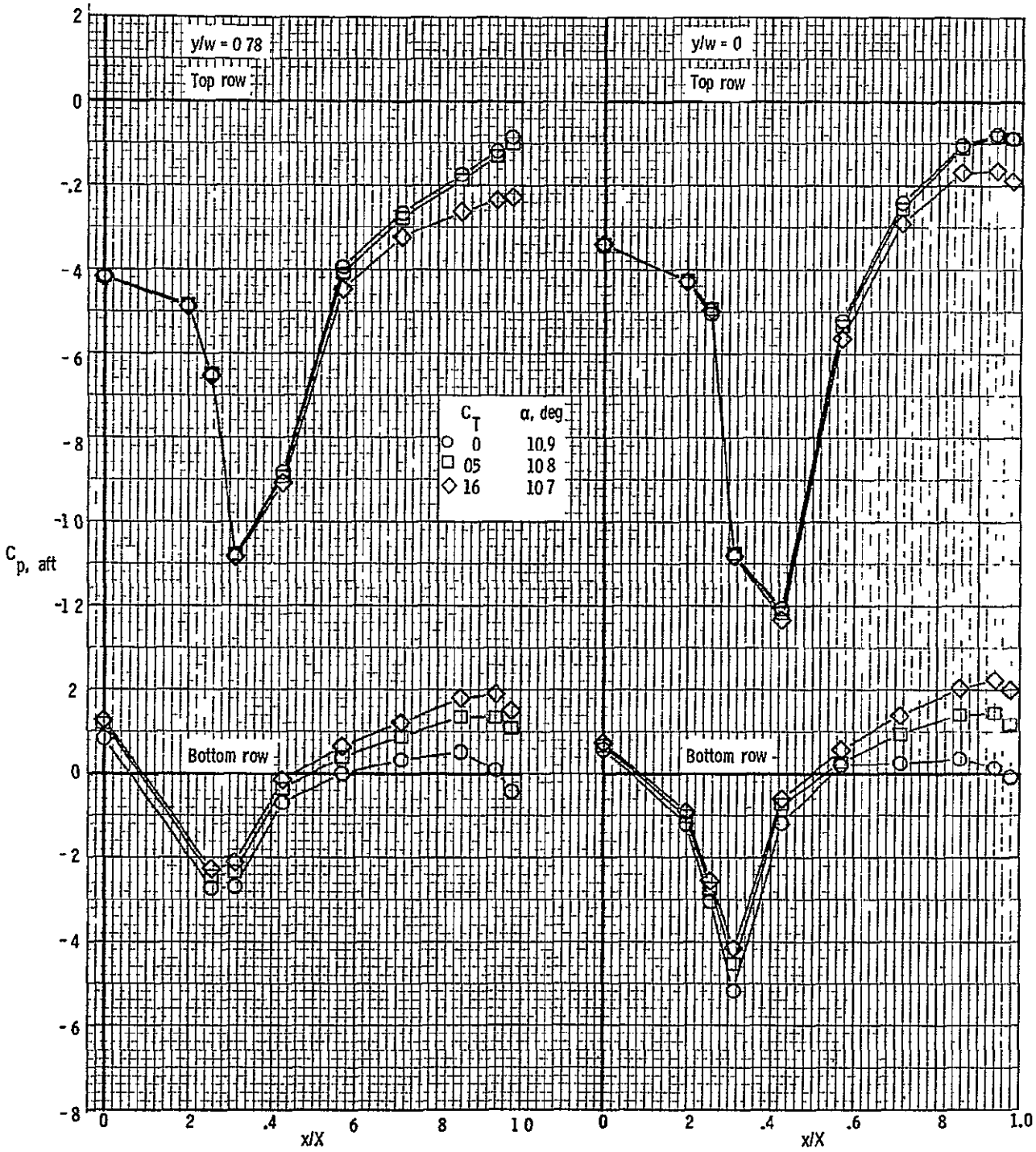

(l) M = 0 80, α ~ 10 8°

Figure 15.- Continued

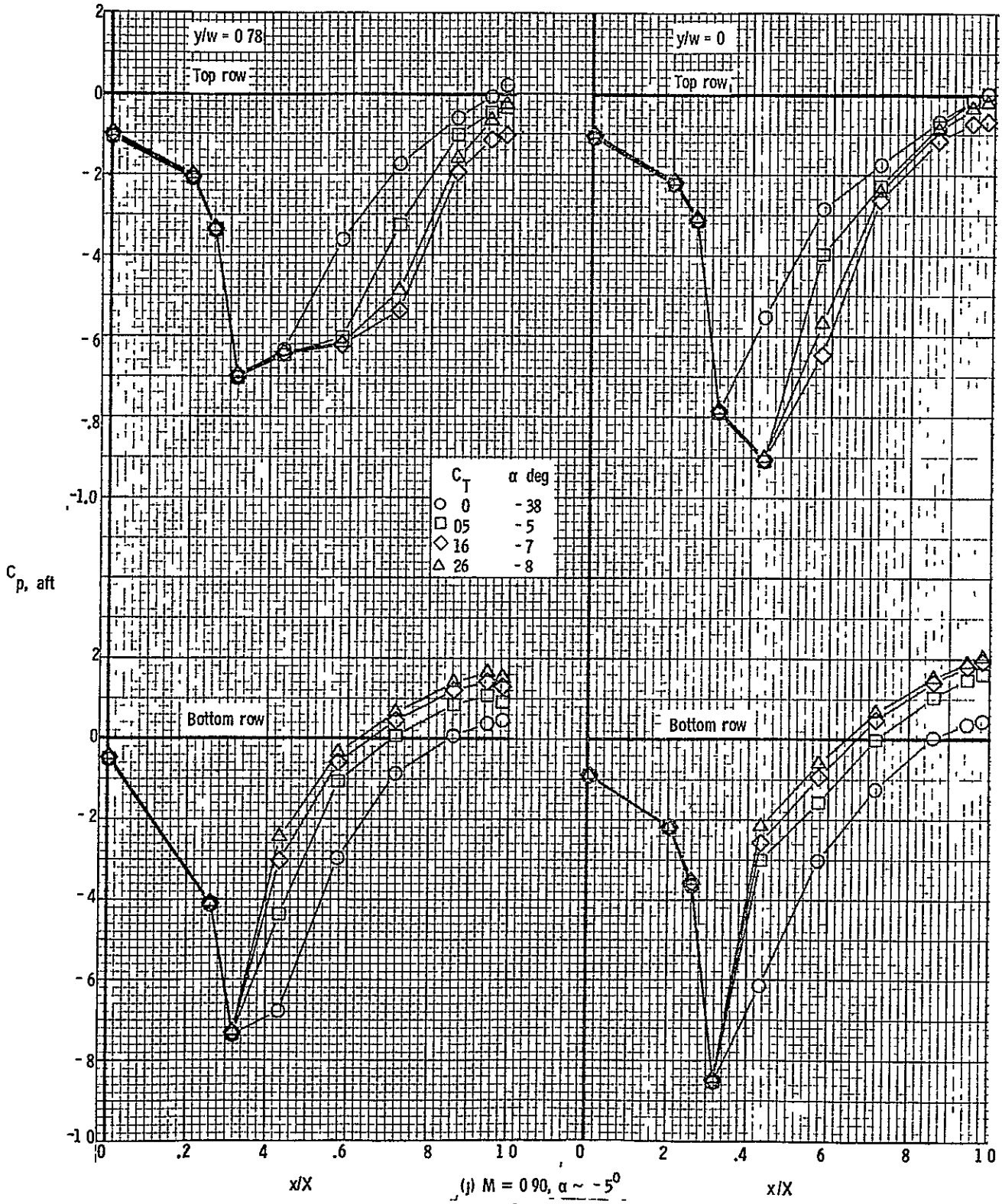

(j) M = 0 90, α ~ -5°

Figure 15.- Continued

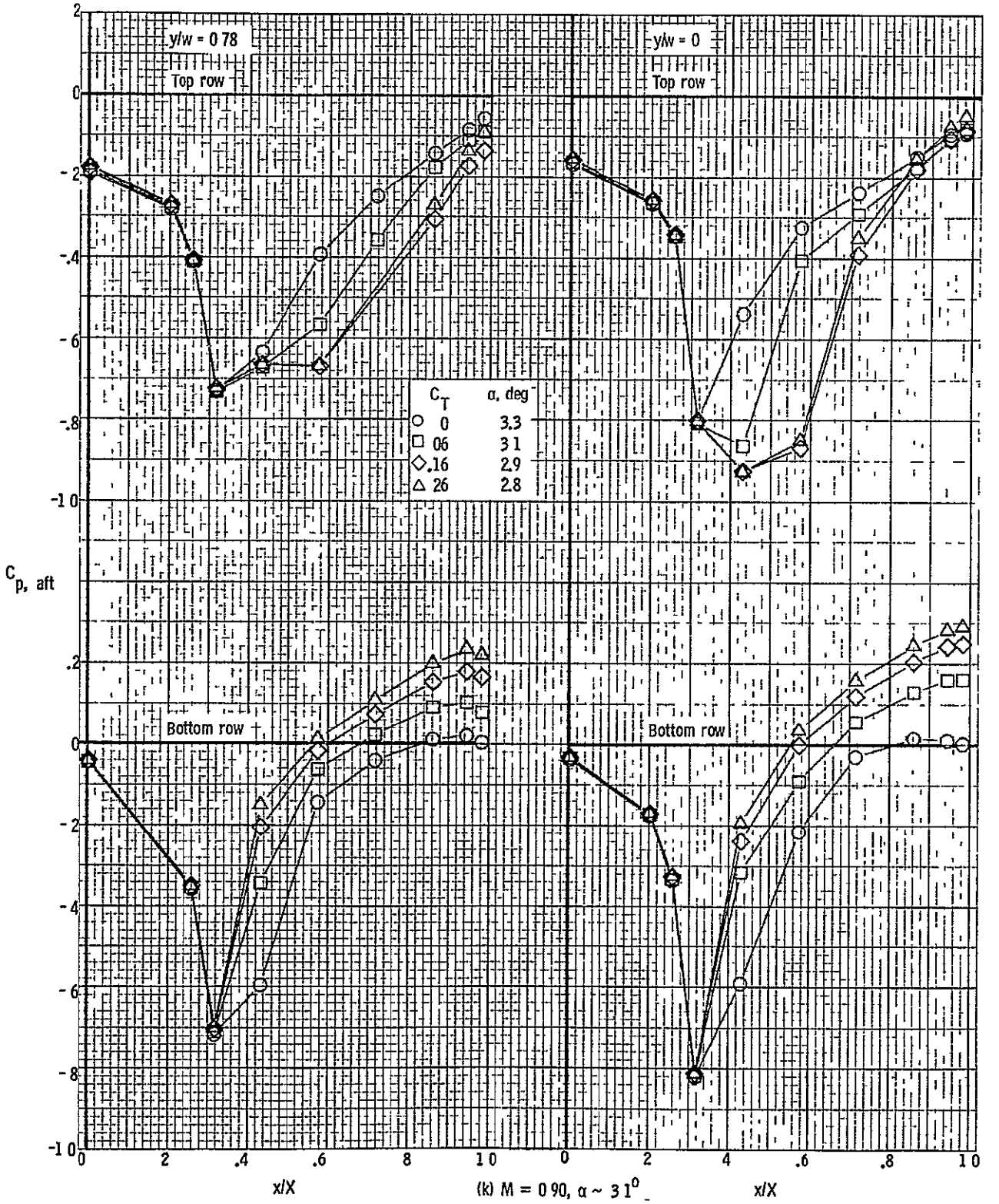

(k) M = 0 90, α ~ 3 1°

Figure 15 - Continued

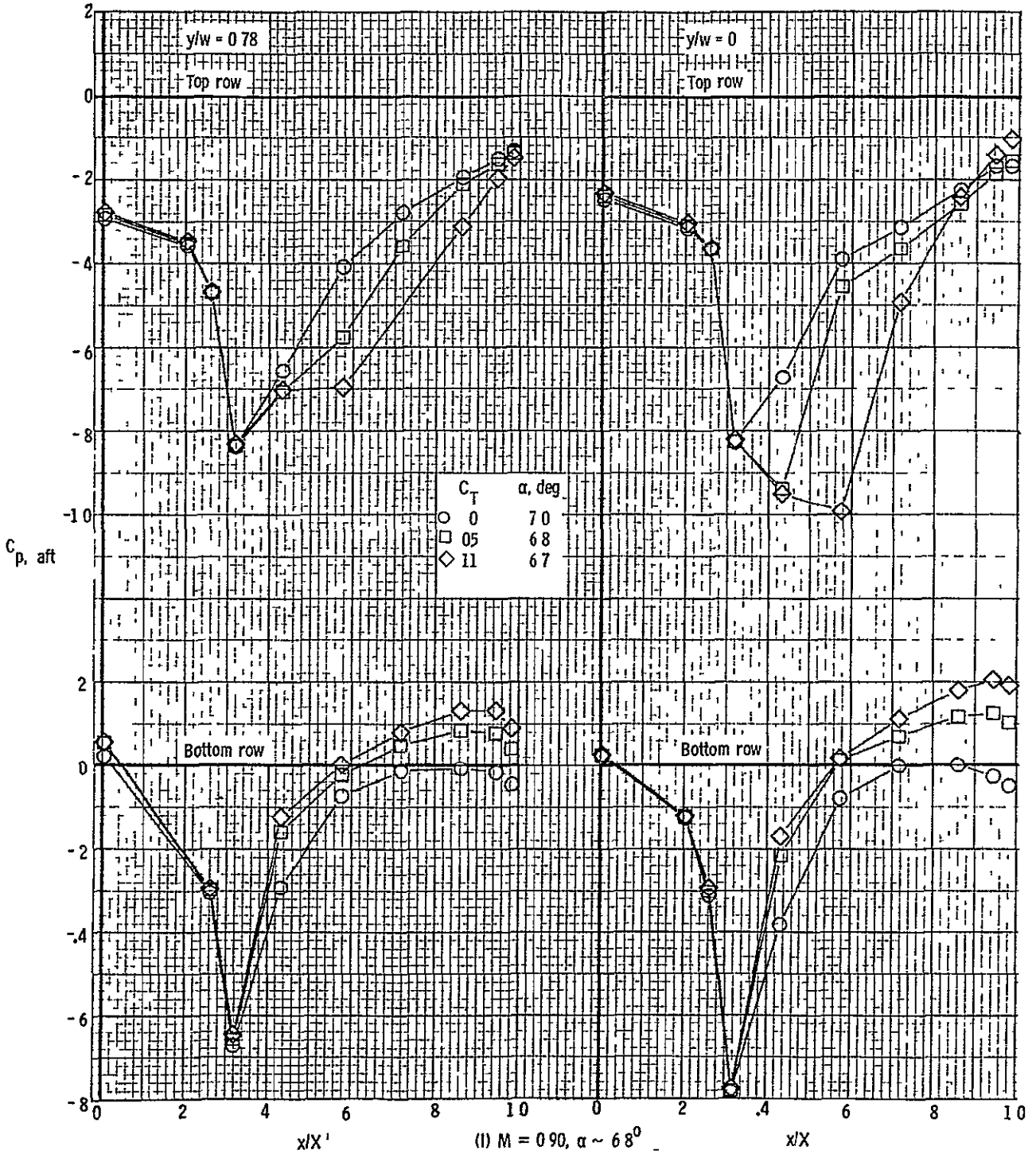

(l) M = 0 90, α ~ 6 8°

Figure 15 - Continued

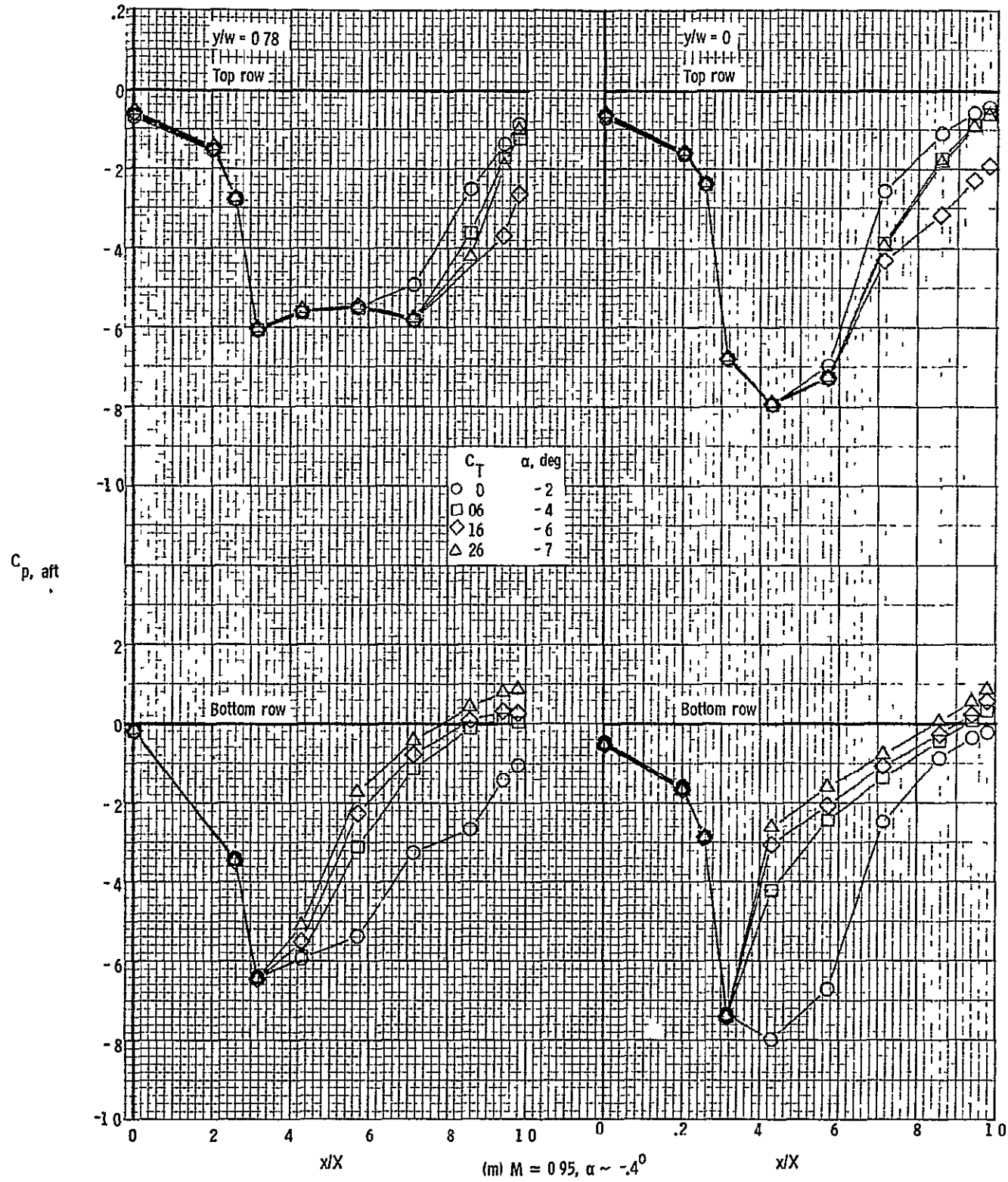

(m) M = 0 95, α ~ -.4°

Figure 15.- Continued

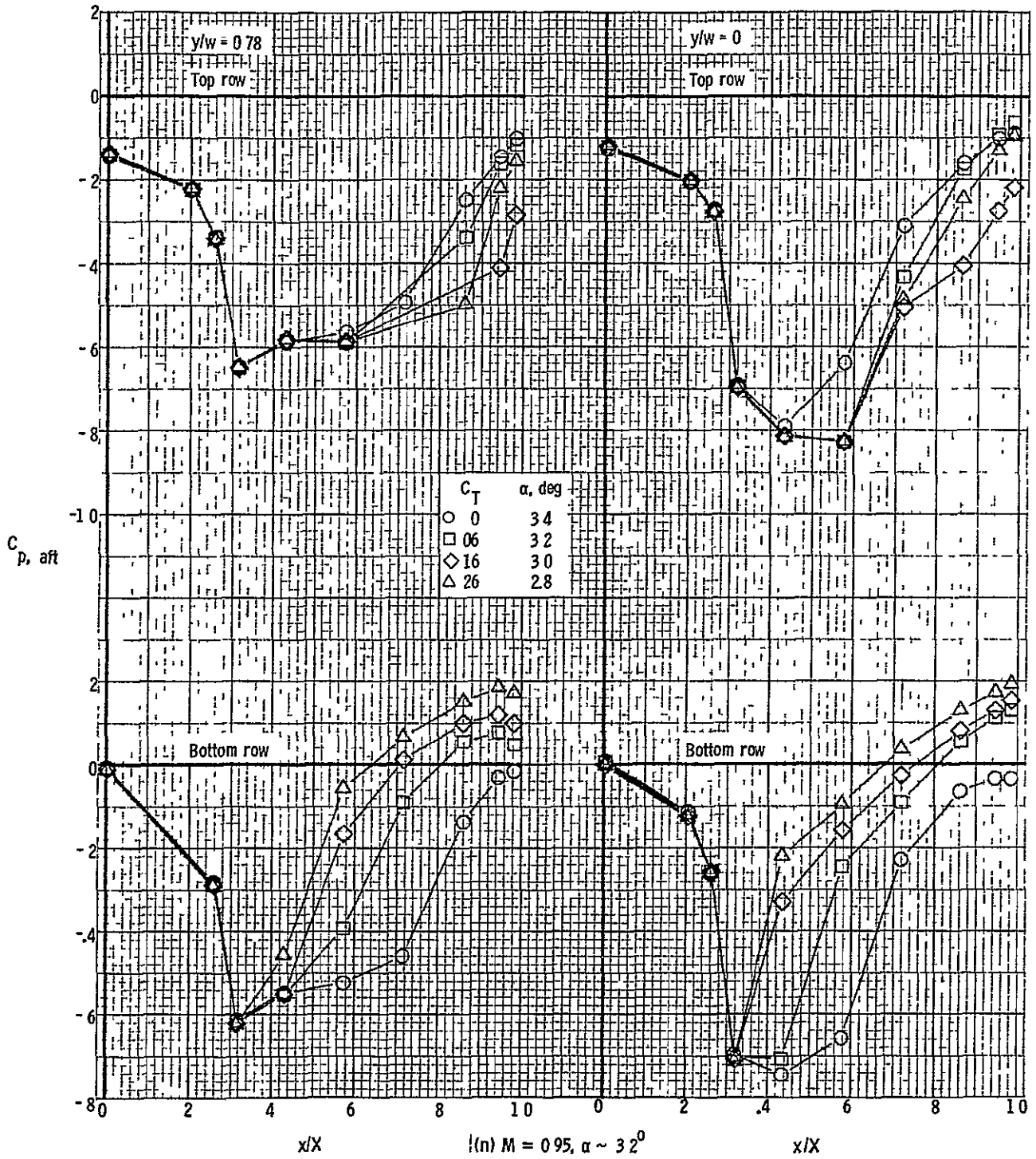

(n) M = 0 95, α ~ 3 2°

Figure 15.- Continued

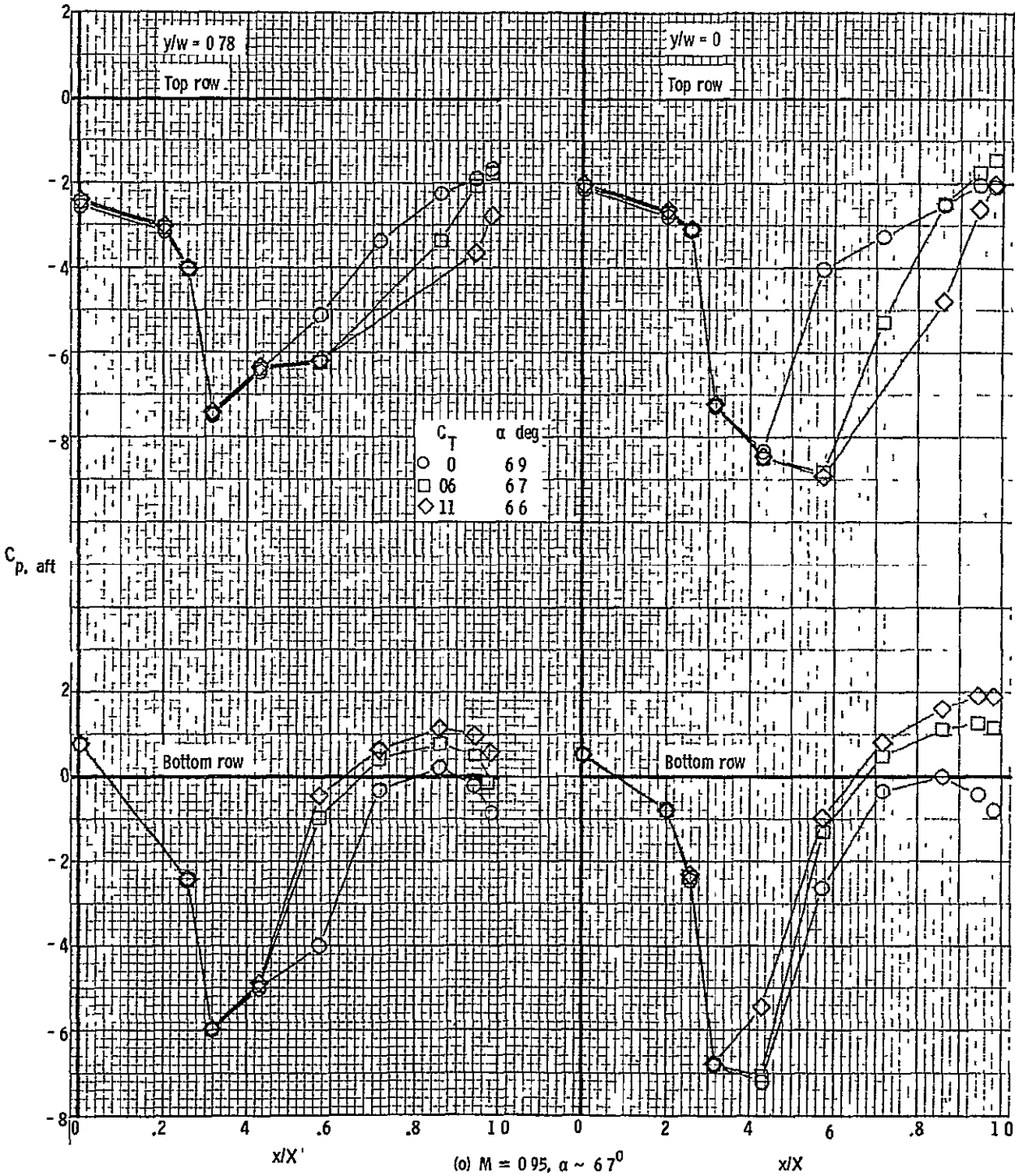

(o) M = 0 95, α ~ 6 7°

Figure 15.- Concluded.

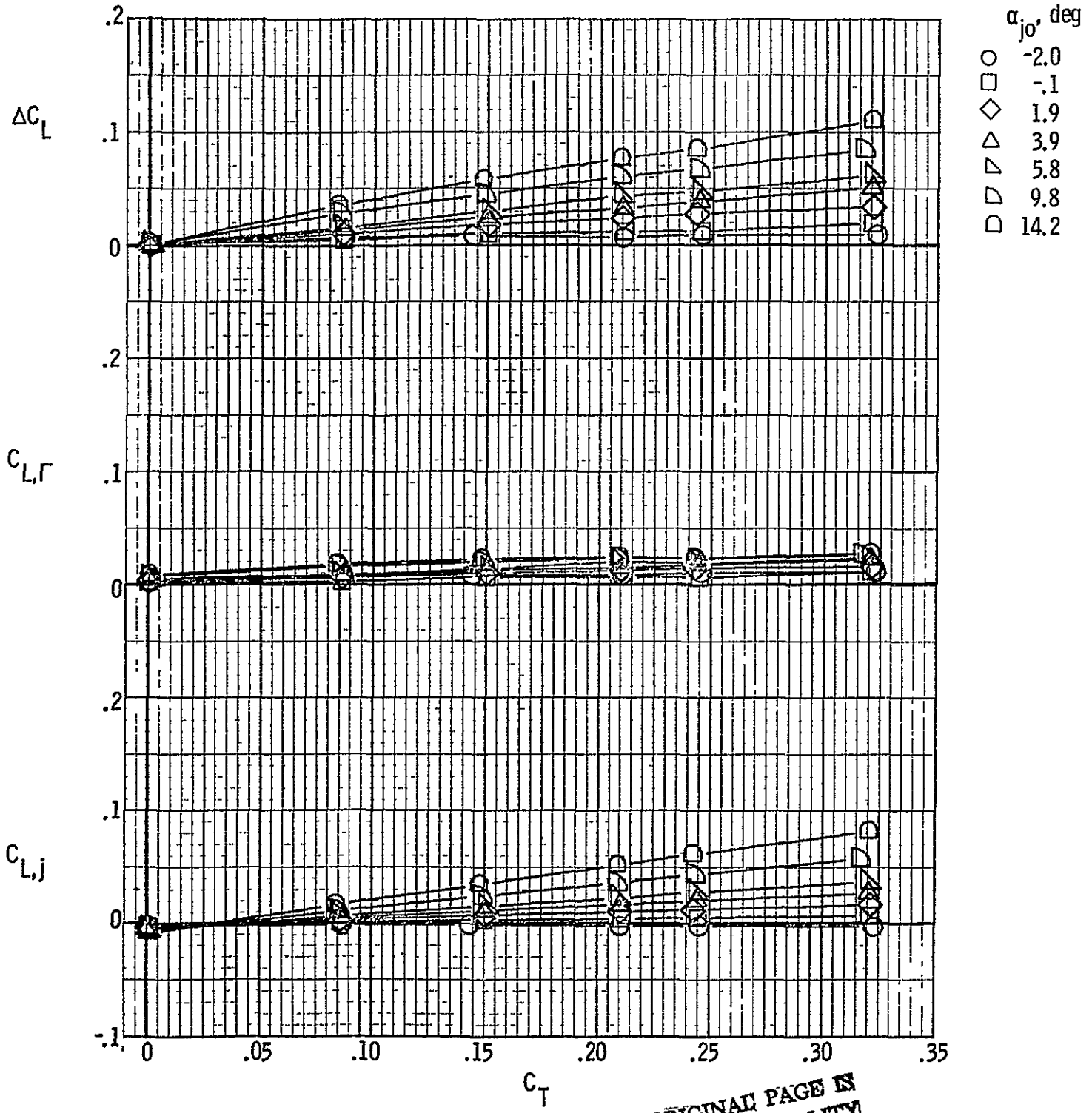

(a) M = 0.40

ORIGINAL PAGE IS
OF POOR QUALITY

Figure 16.- Jet lift, induced lift and incremental lift characteristics, $\delta_d = 0^\circ$.

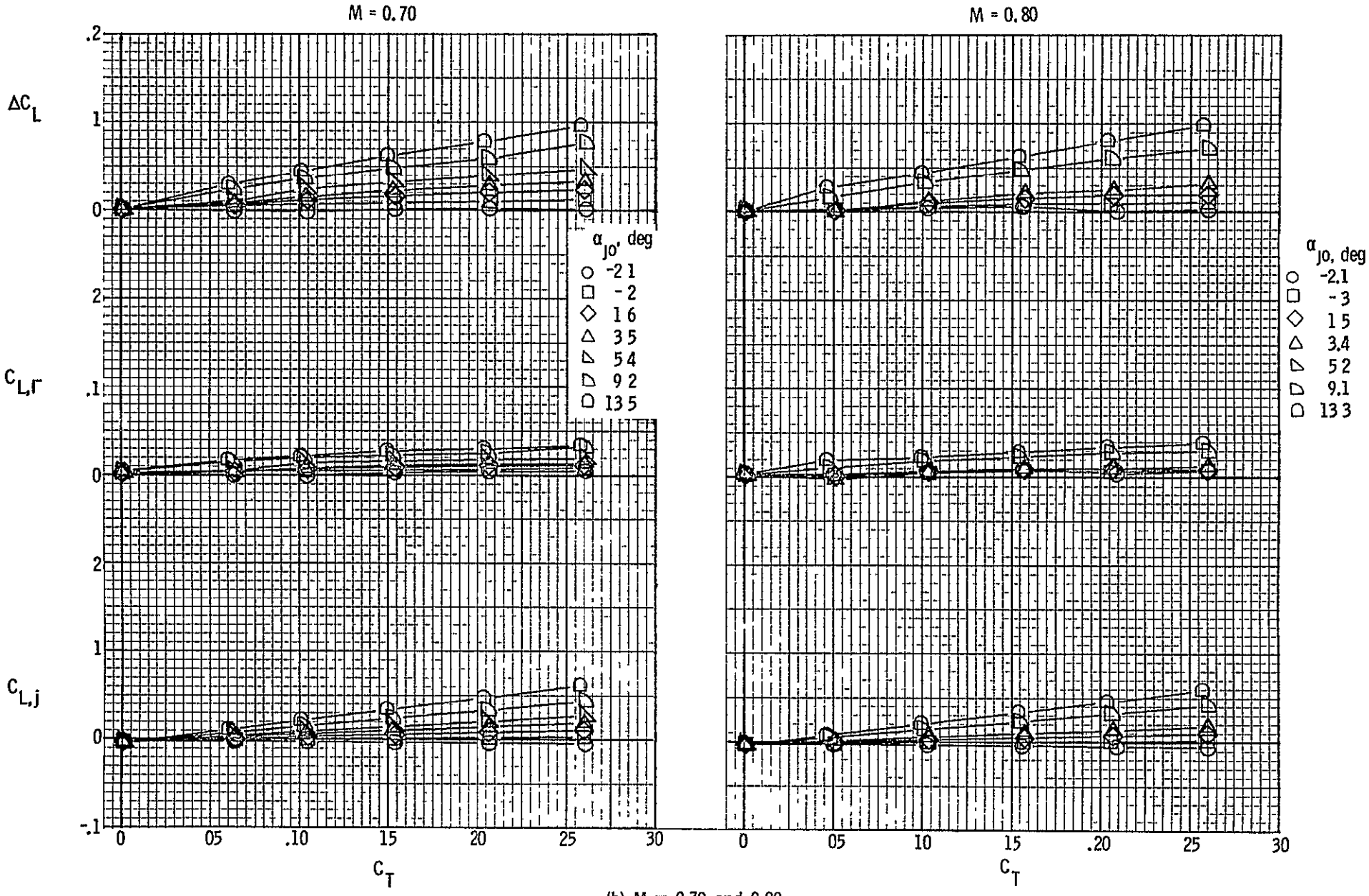

(b) M = 0.70 and 0.80

Figure 16.- Continued

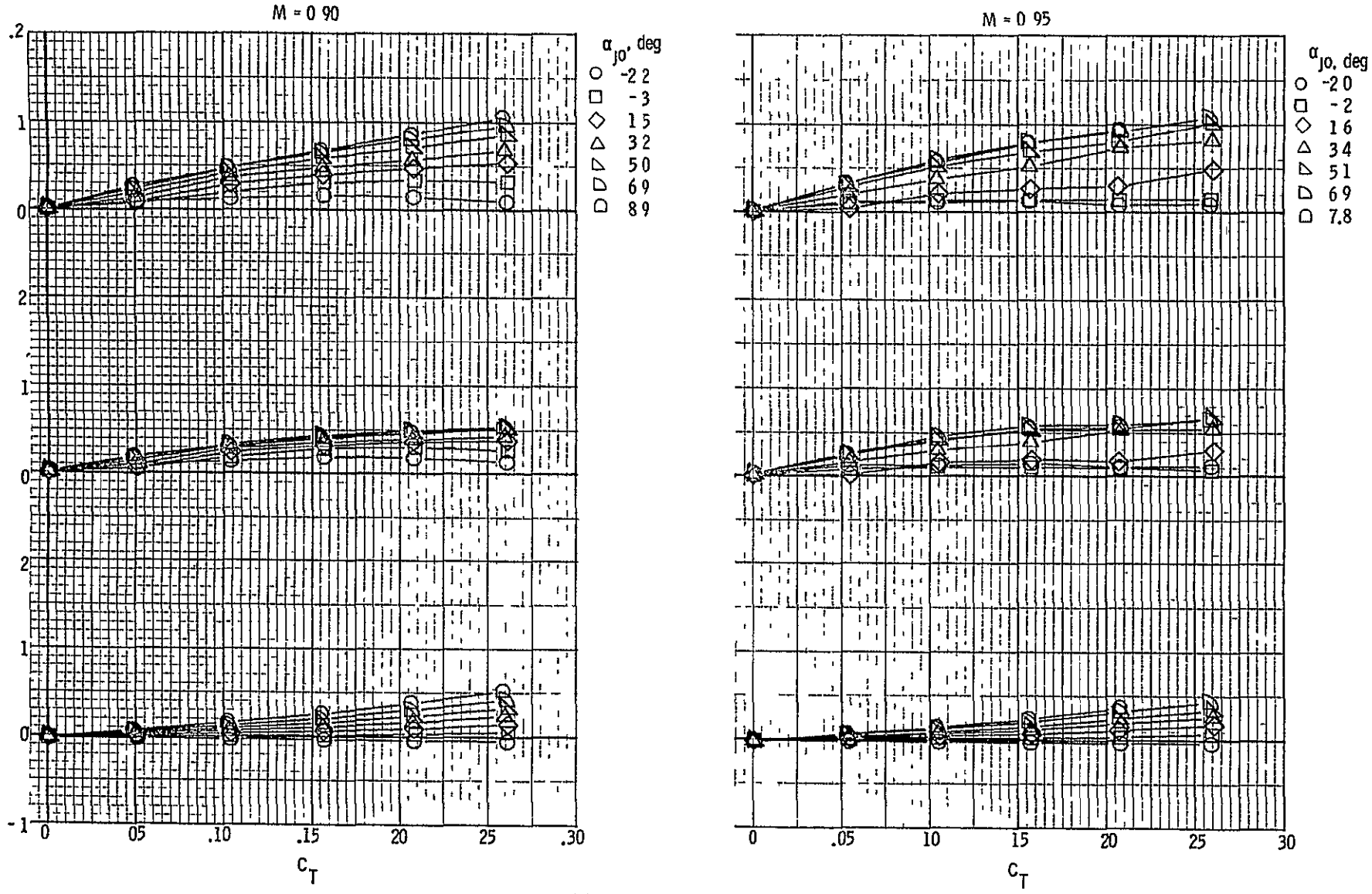

(c) M = 0 90 and 0 95

Figure 16 - Concluded

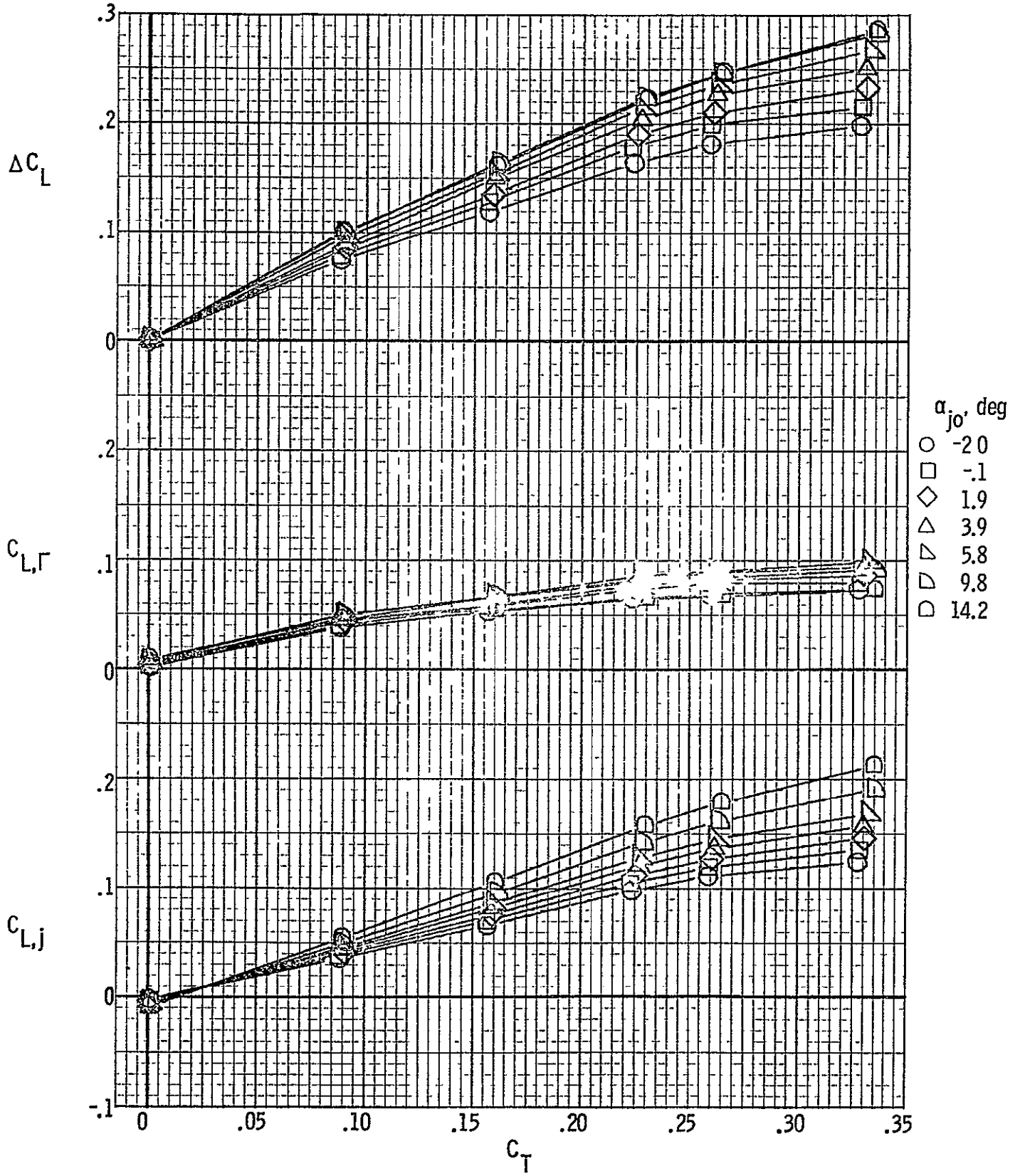

(a) M = 0.40

Figure 17.- Jet lift, induced lift and incremental lift characteristics, $\delta_d = 30^\circ$.

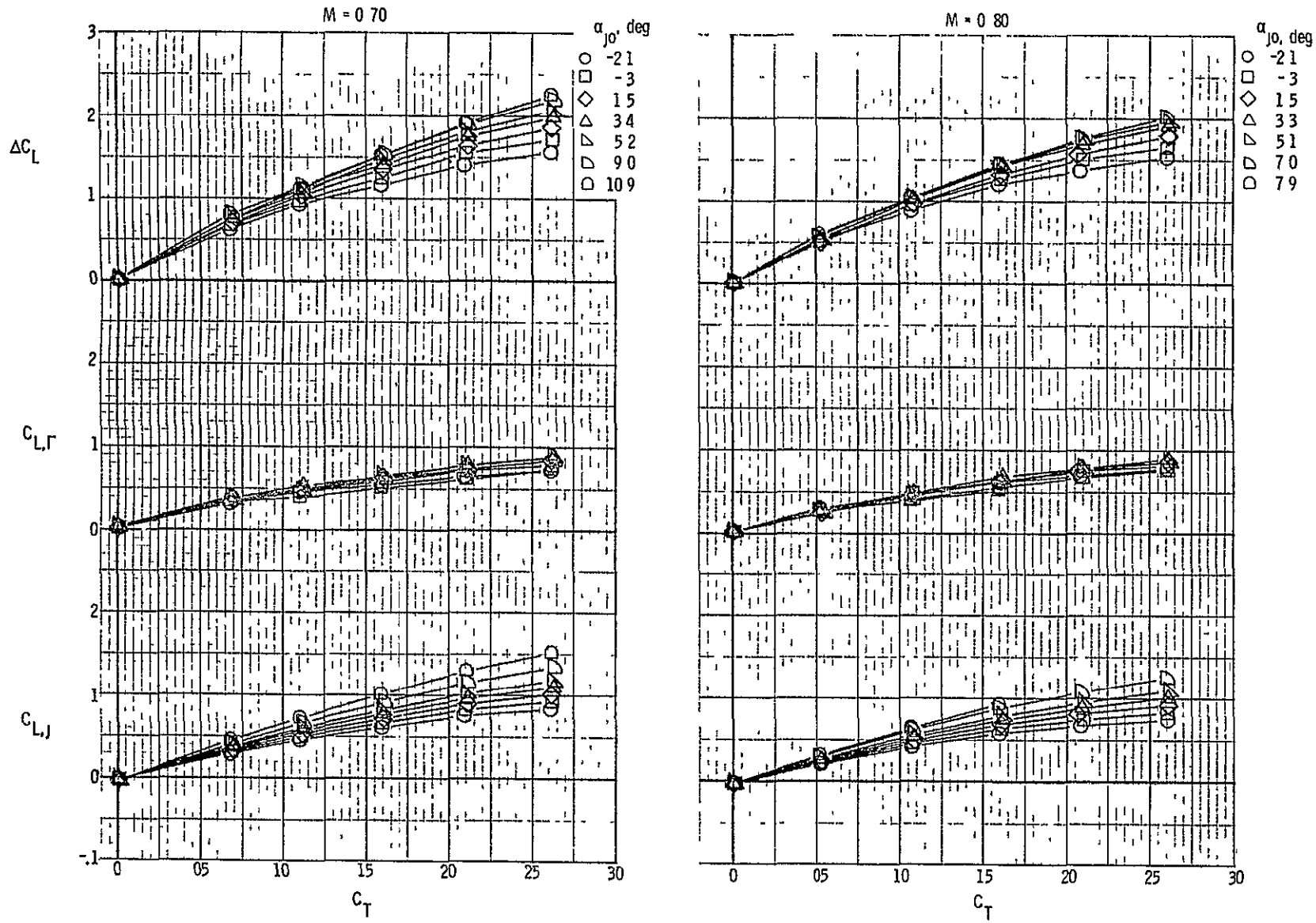

(b) M = 0 70 and 0 80

Figure 17 - Continued

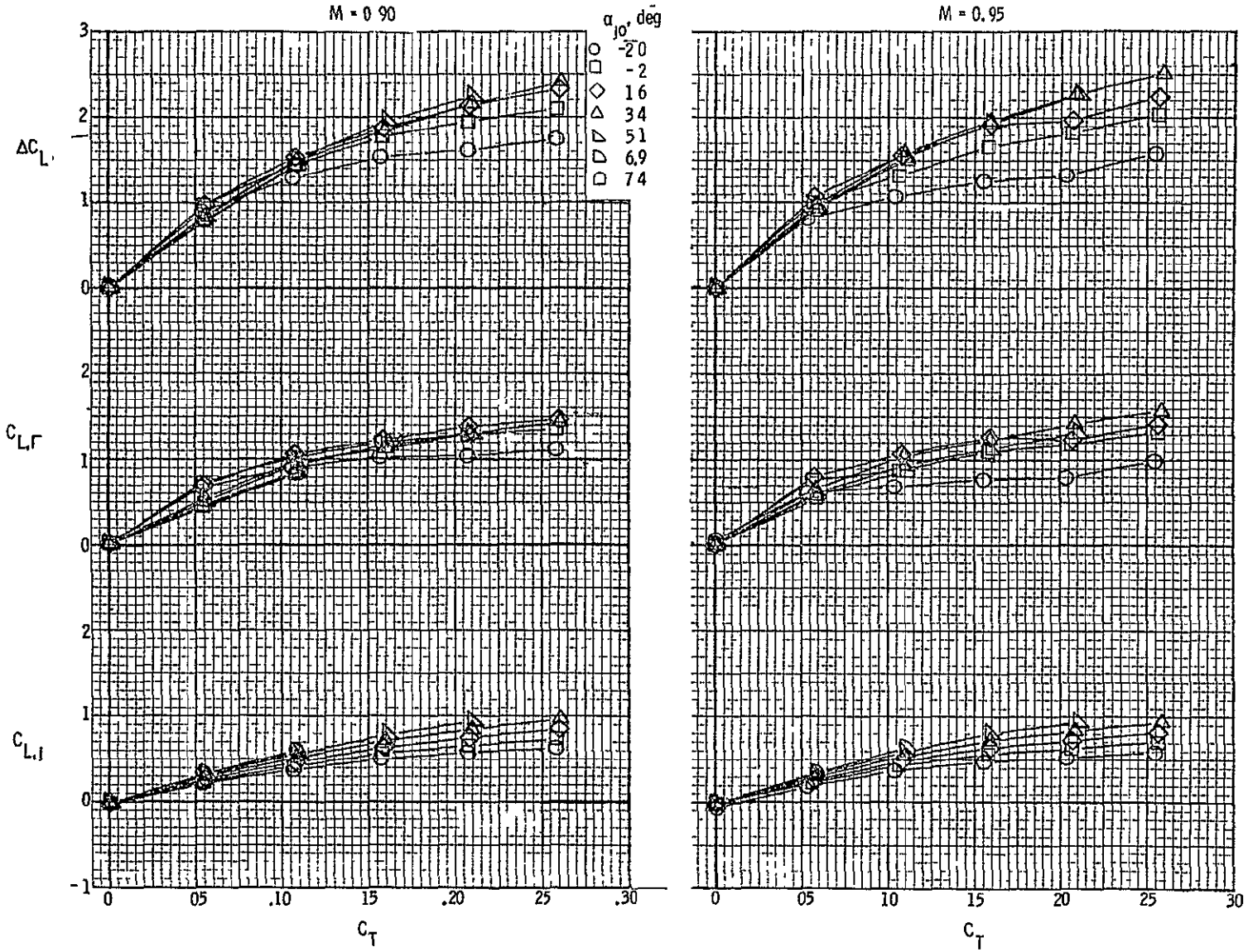

(c) M = 0.90 and 0.95

Figure 17 - Concluded

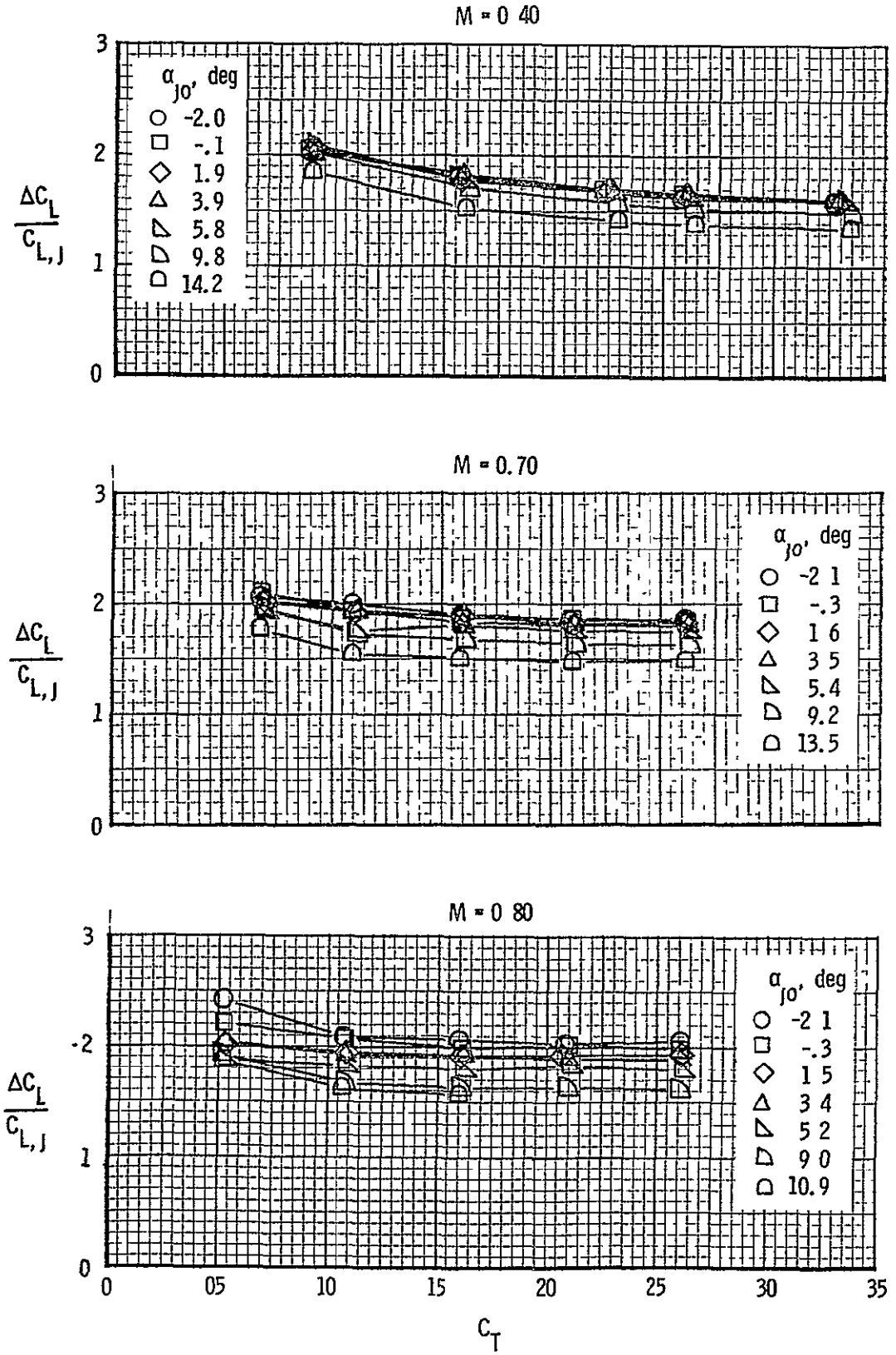

(a) M = 0.40 to 0.80.

Figure 18. - Variation of gain factor with thrust coefficient, $\delta_d = 30°$.

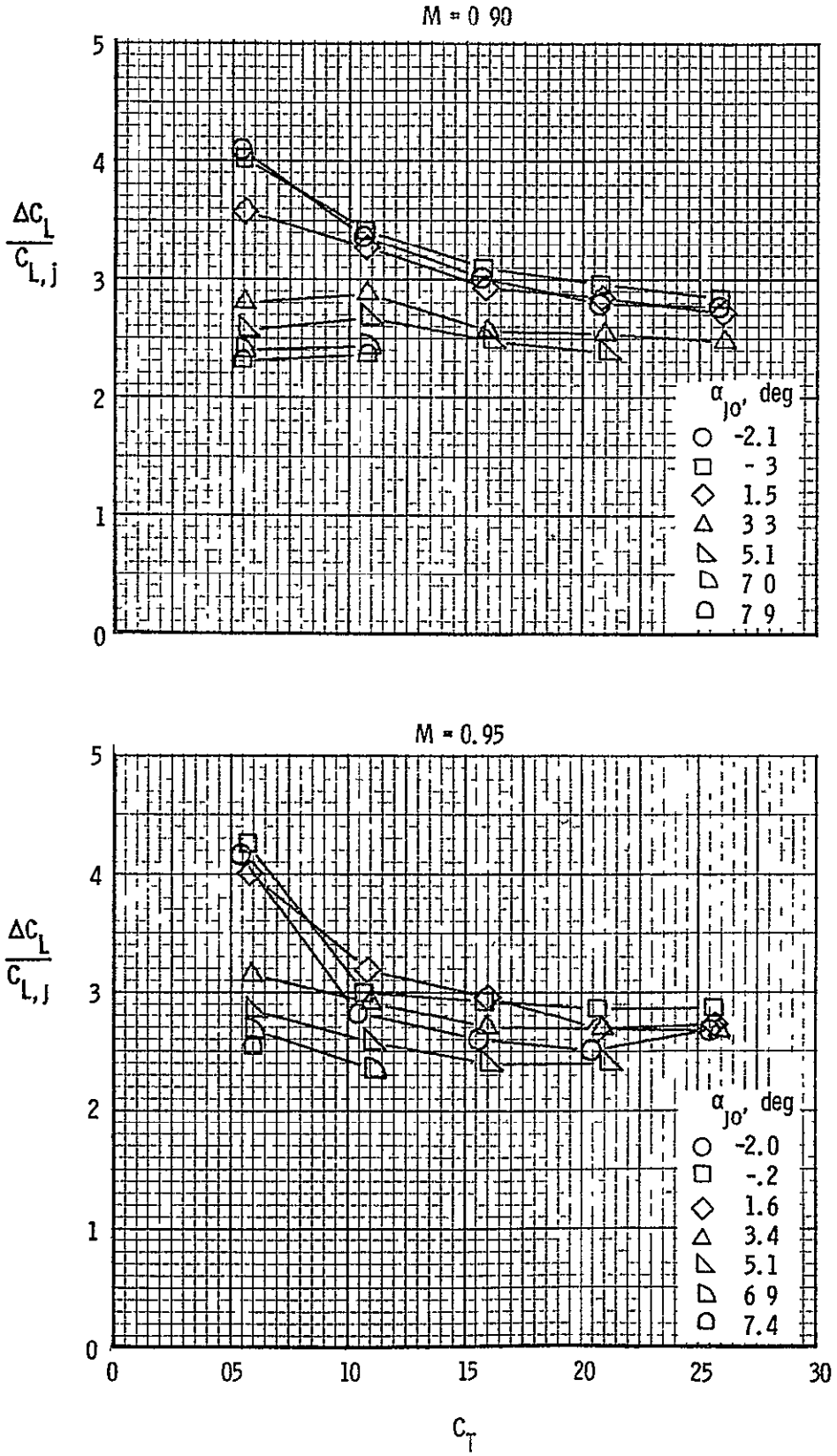

(b) M = 0.90 amd 0 95.
Figure 18. - Concluded.

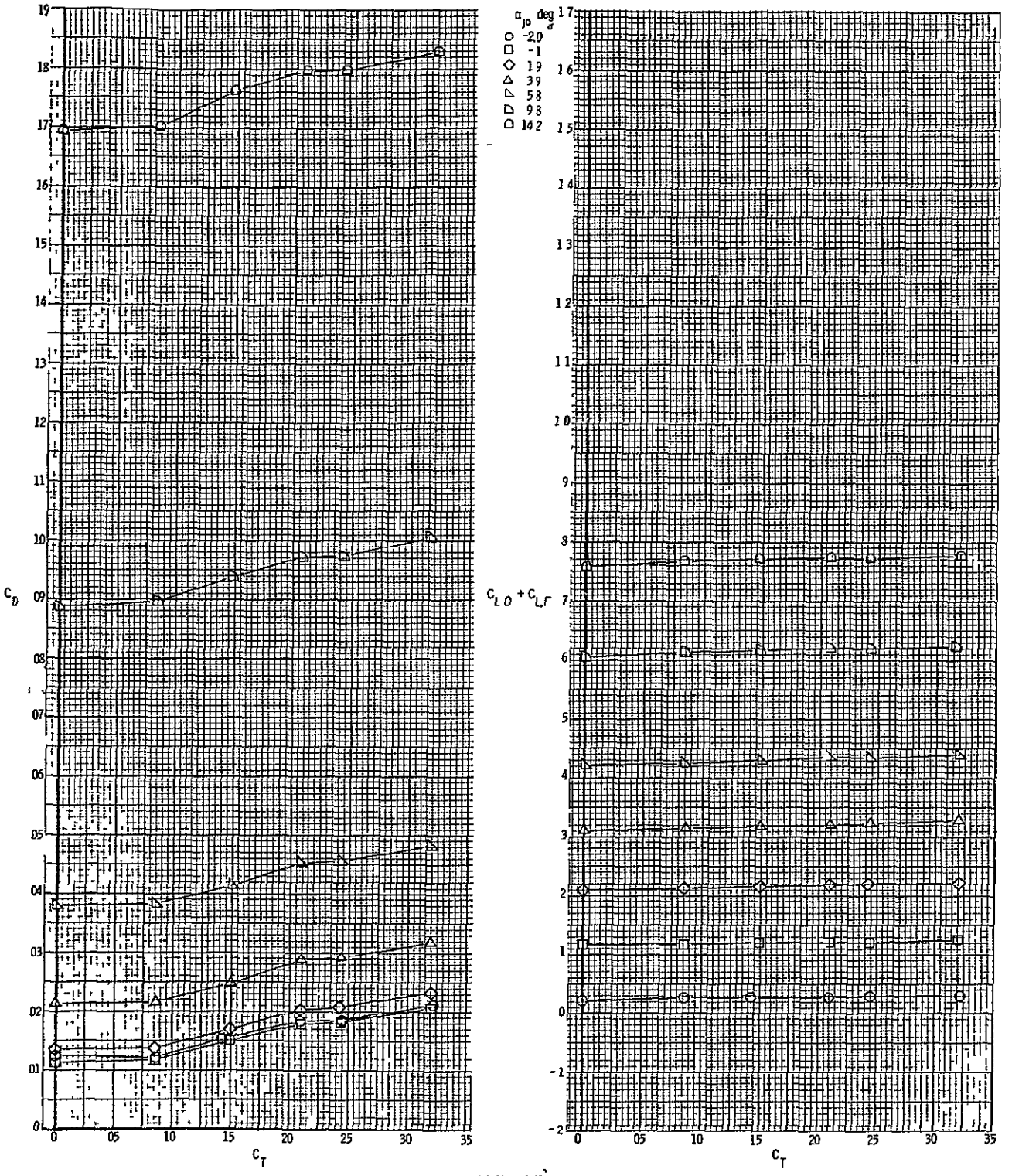

(a) M = 0.40

Figure 19 - Drag and lift characteristics $\delta_d = 0^\circ$

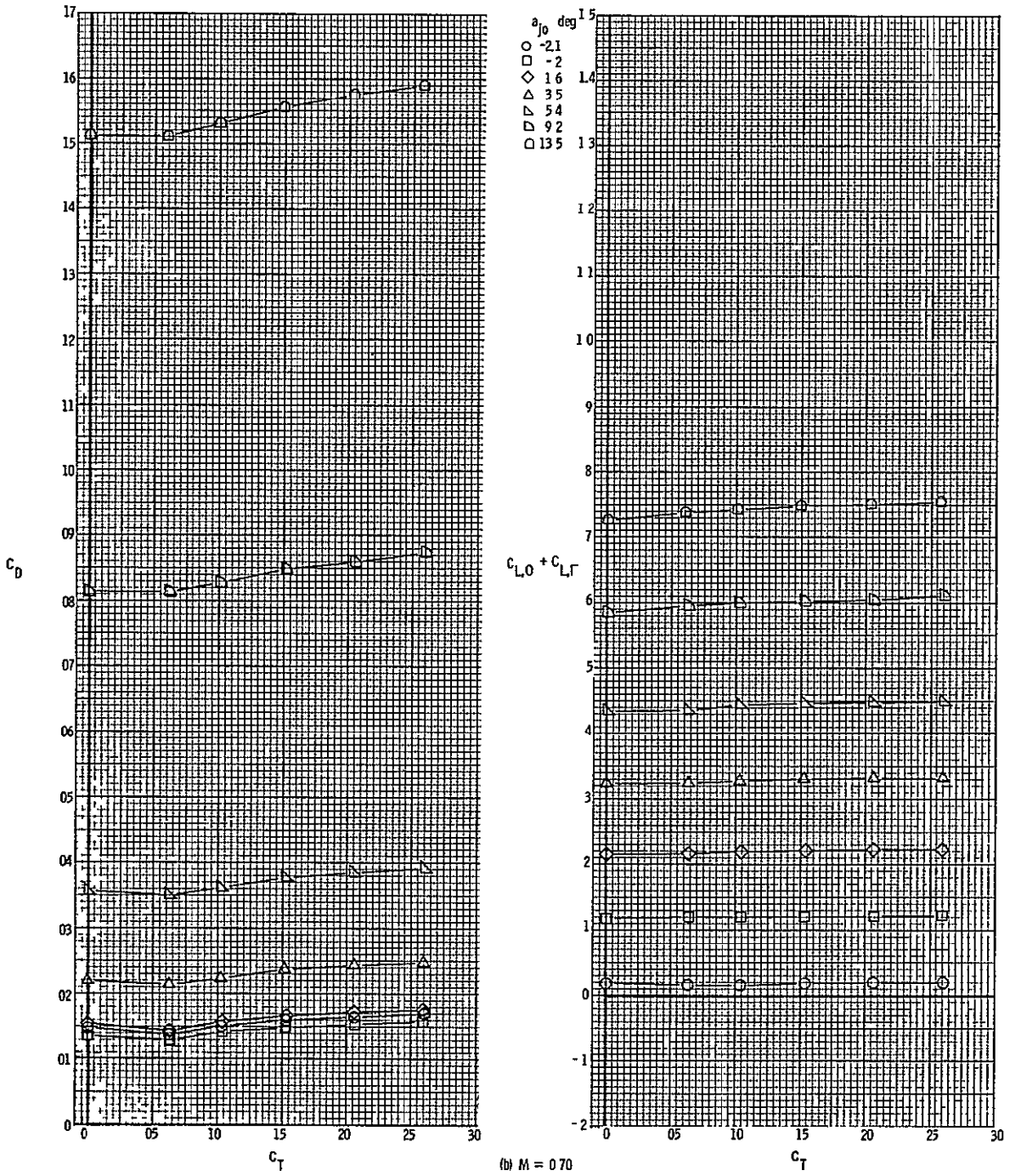

(b) M = 0.70

Figure 19 - Continued

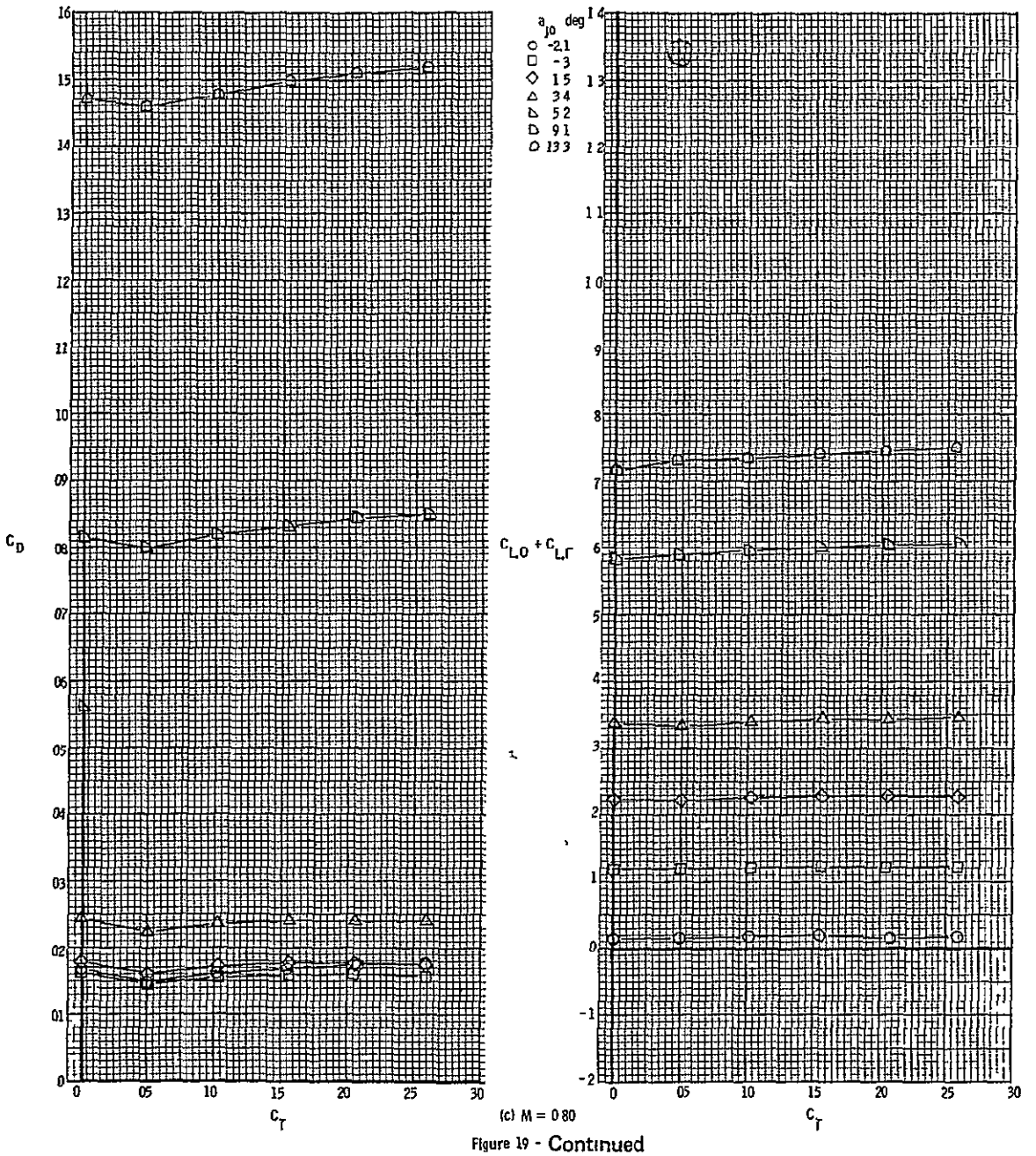

(c) M = 0.80

Figure 19 - Continued

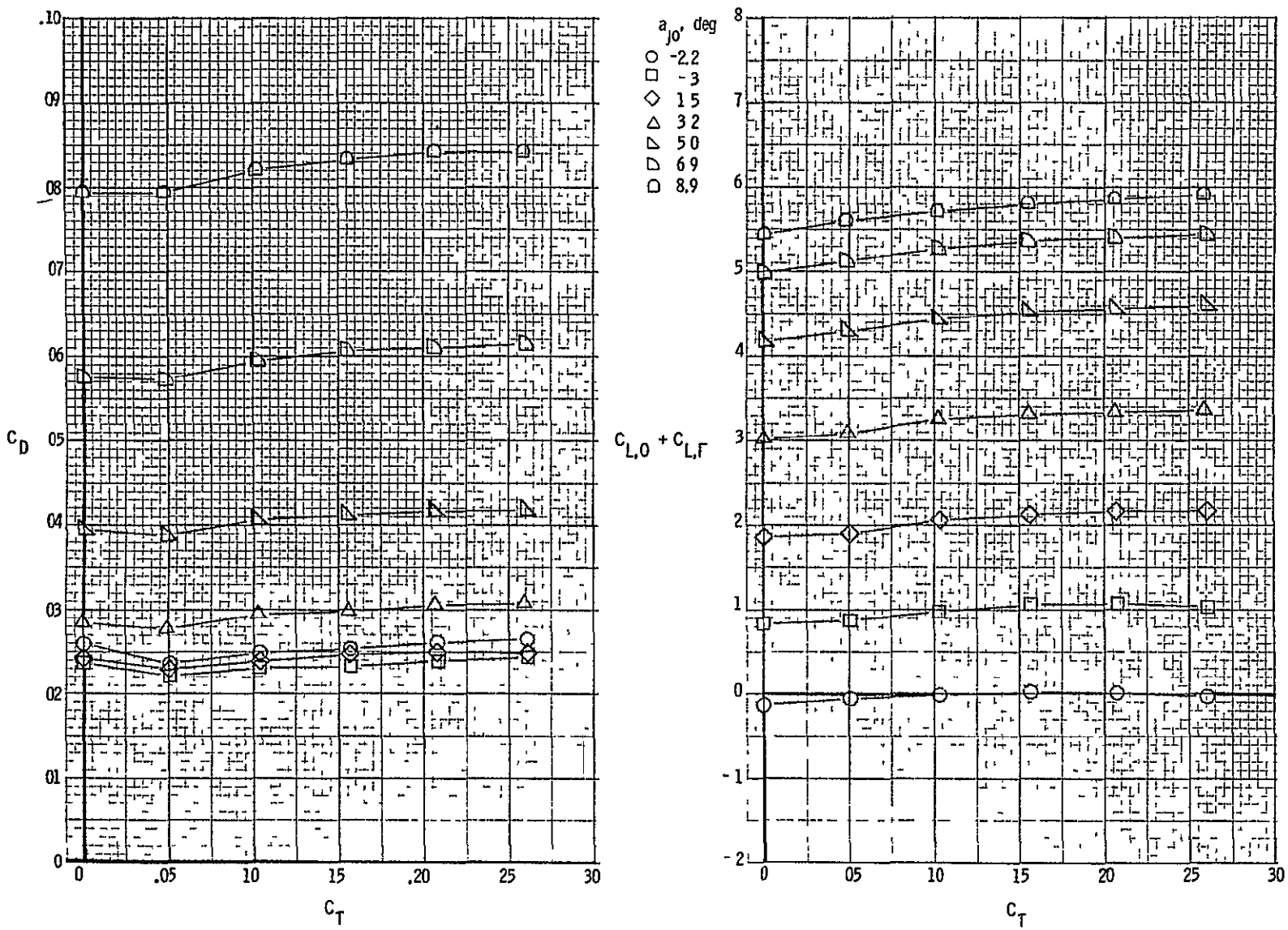

(d) M = 0.90

Figure 19 - Continued

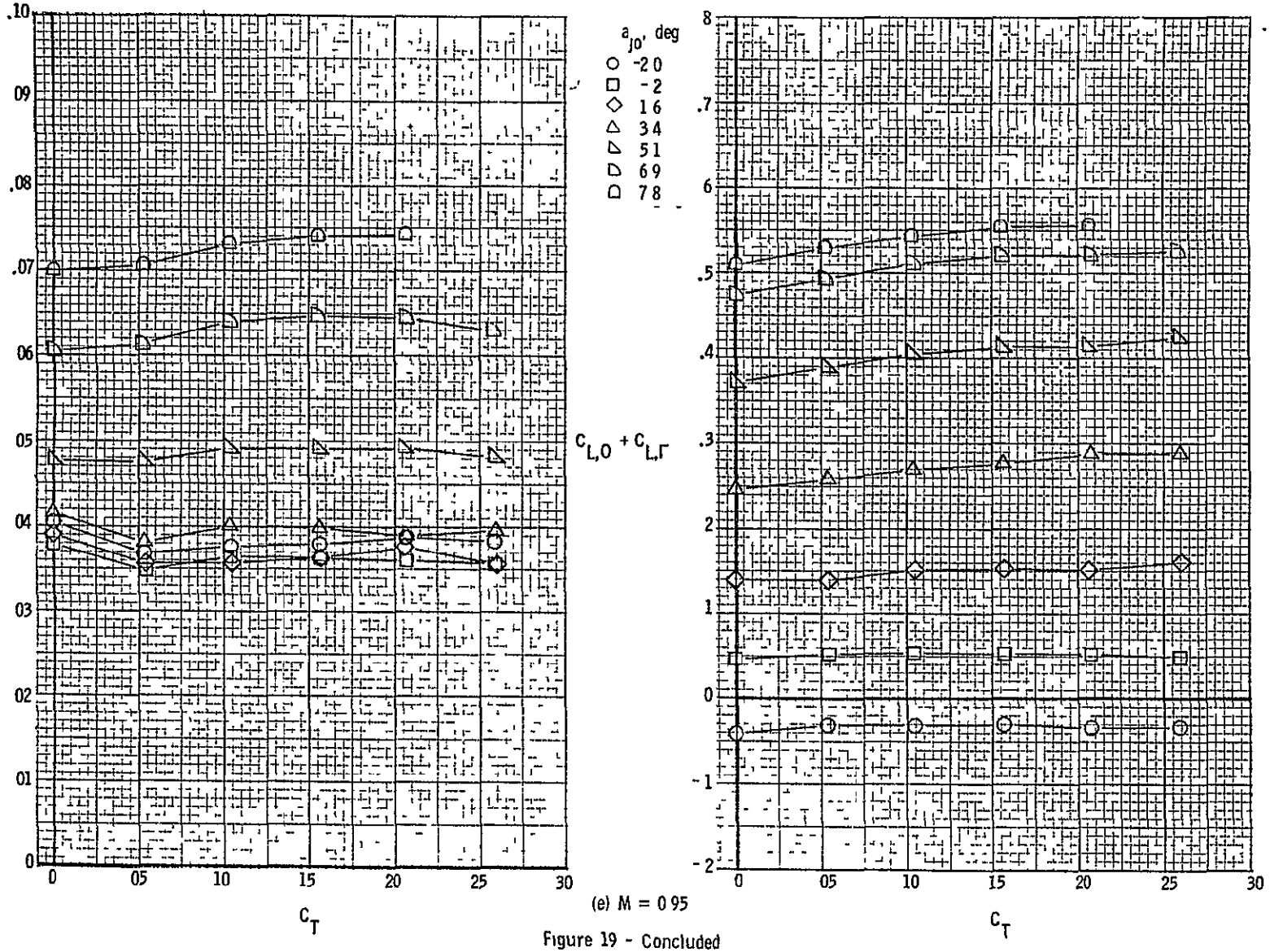

(e) M = 0 95

Figure 19 - Concluded

ORIGINAL PAGE IS
OF POOR QUALITY

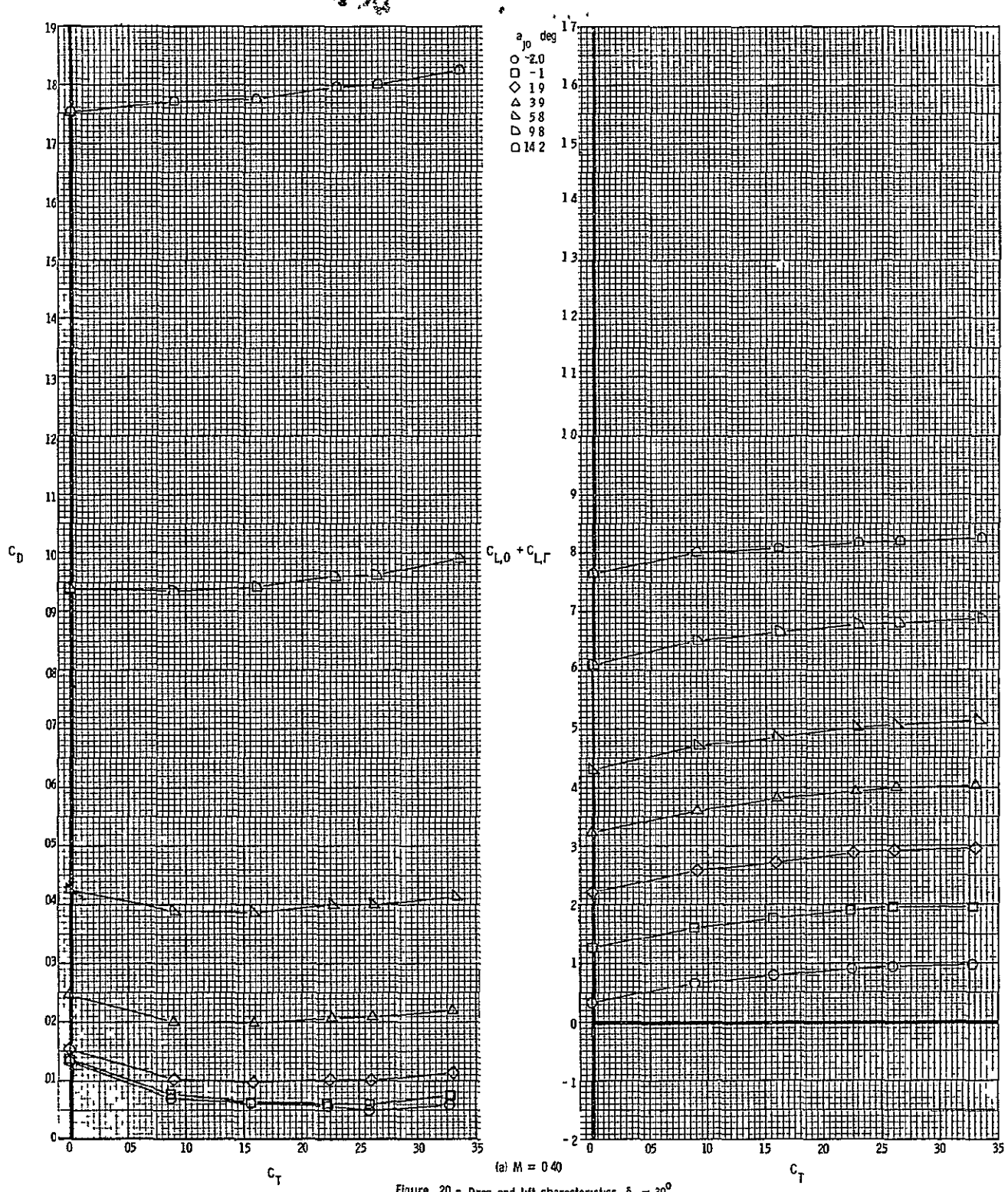

(a) M = 0.40

Figure 20 - Drag and lift characteristics $\delta_d = 30^\circ$

ORIGINAL PAGE IS
OF POOR QUALITY

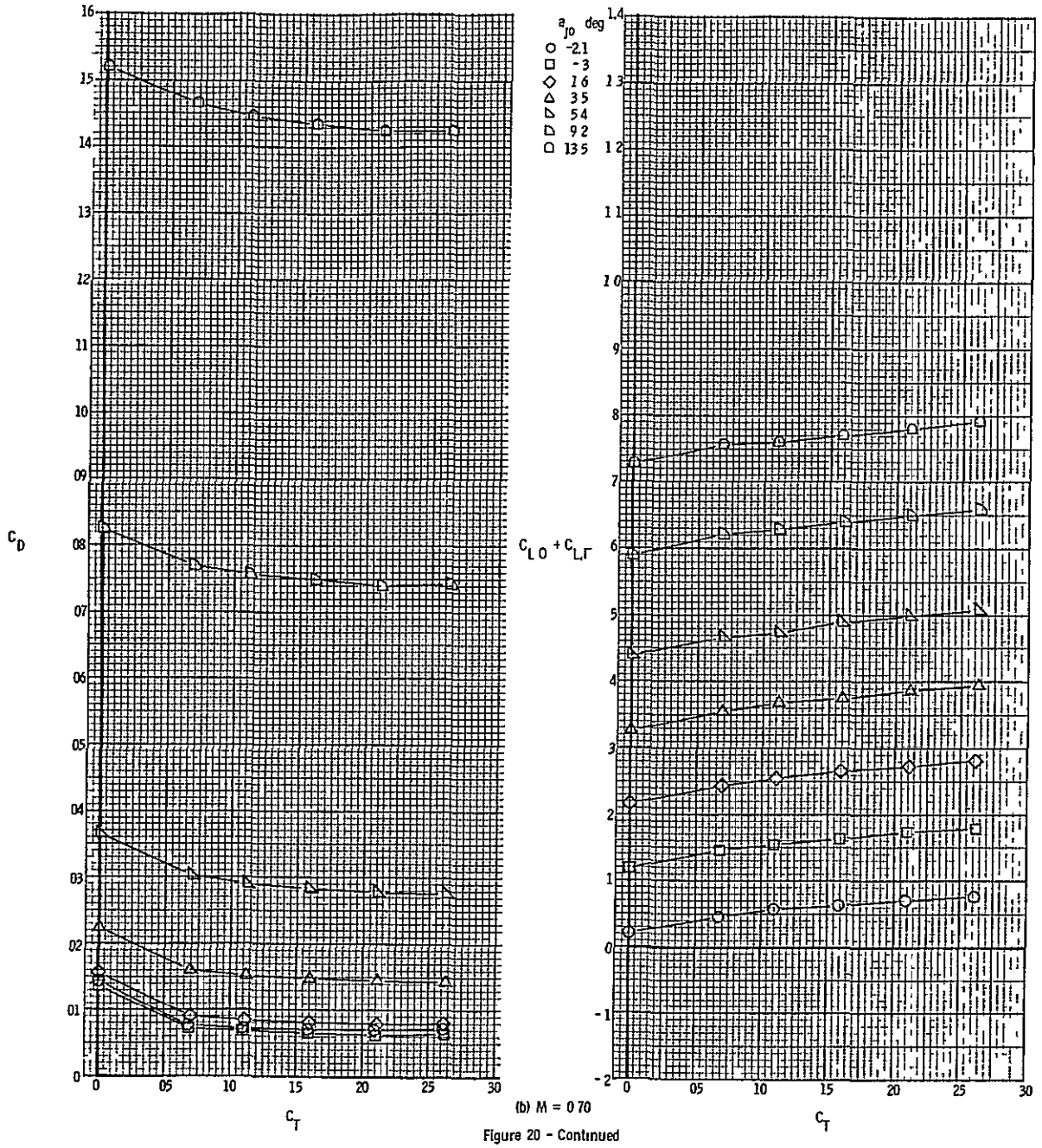

(b) M = 0.70

Figure 20 - Continued

C-2

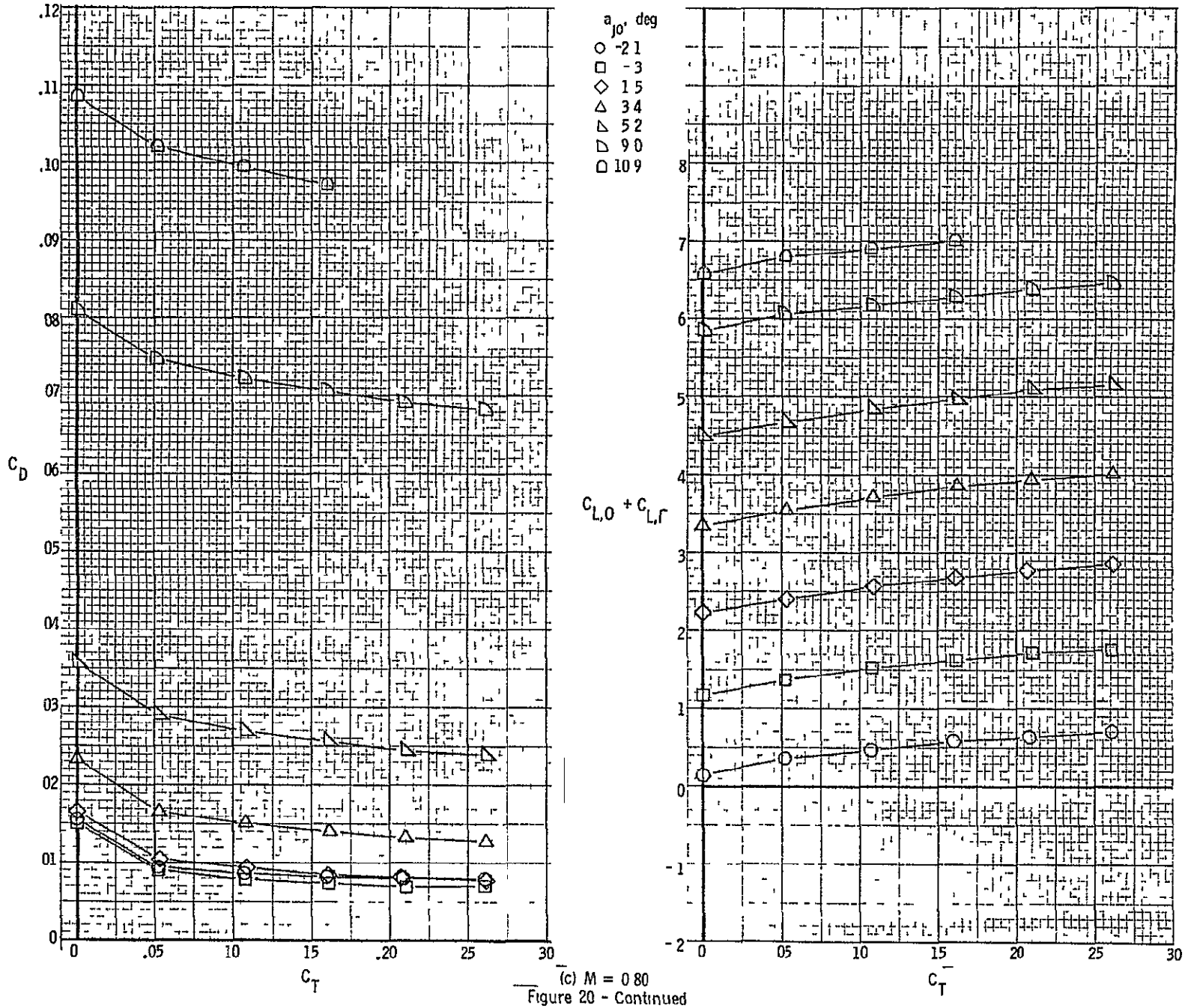

(c) M = 0 80

Figure 20 - Continued

ORIGINAL PAGE IS
OF POOR QUALITY

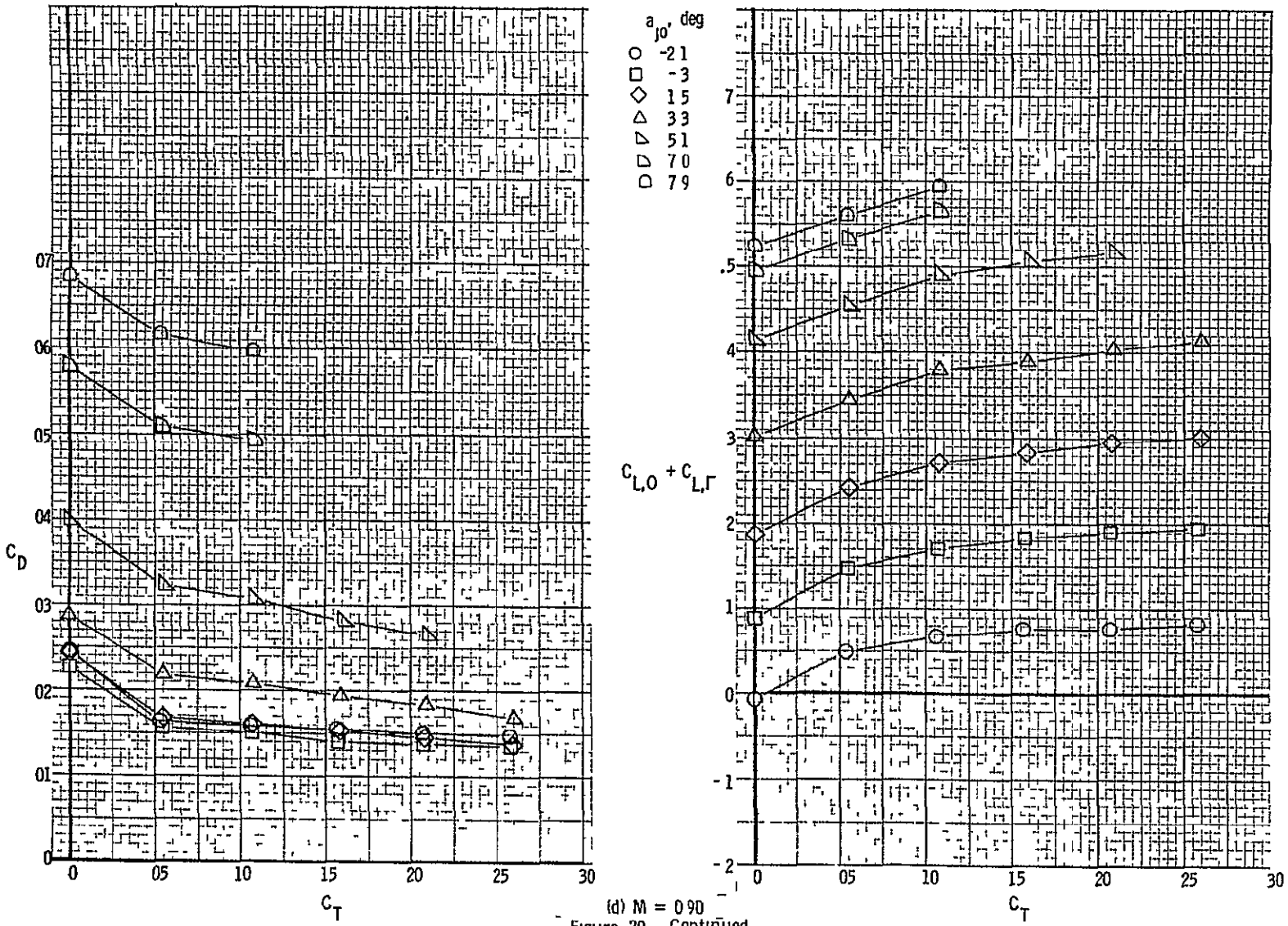

(d) M = 0.90

Figure 20 - Continued

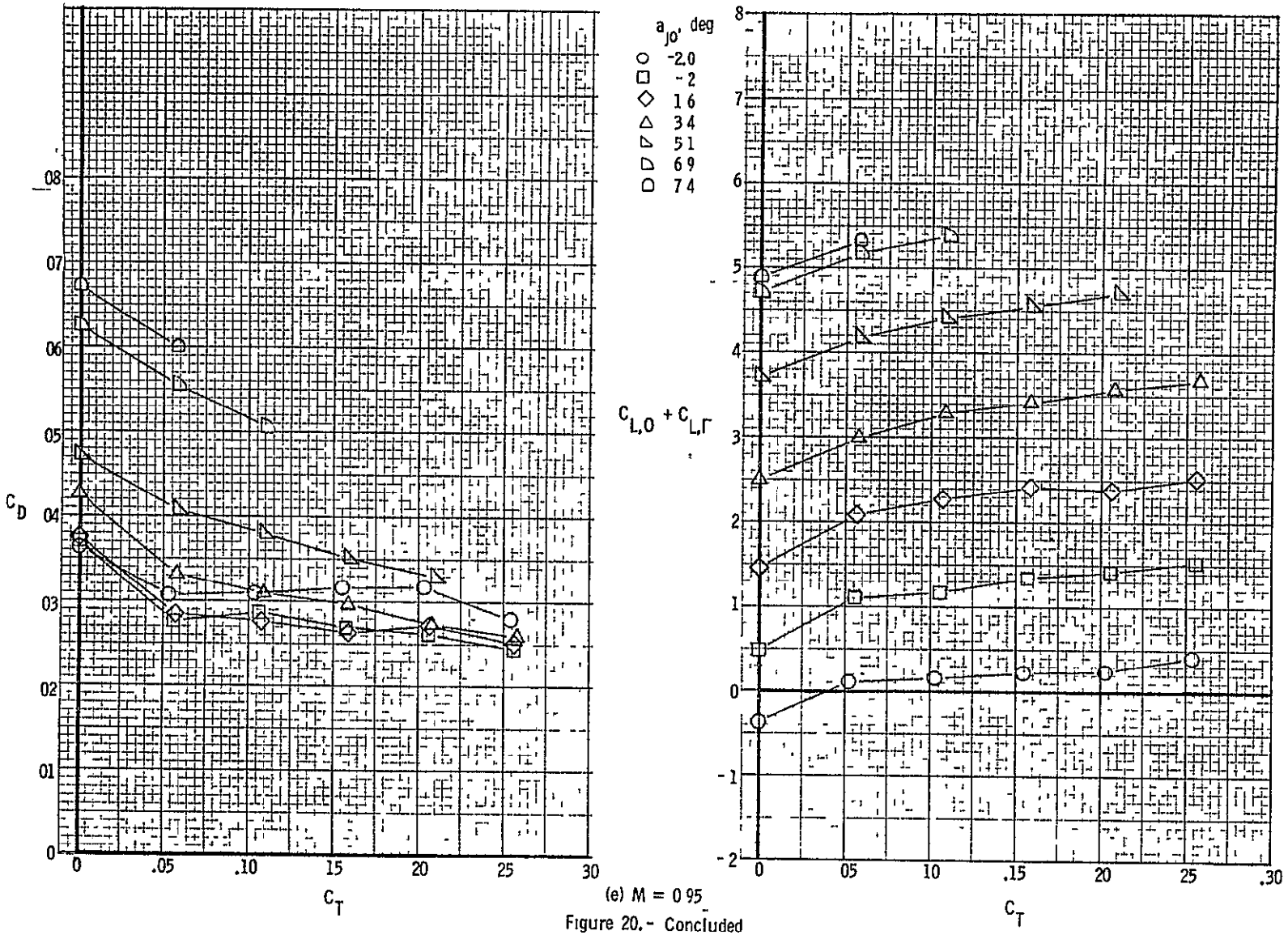

(e) M = 0 95

Figure 20.- Concluded

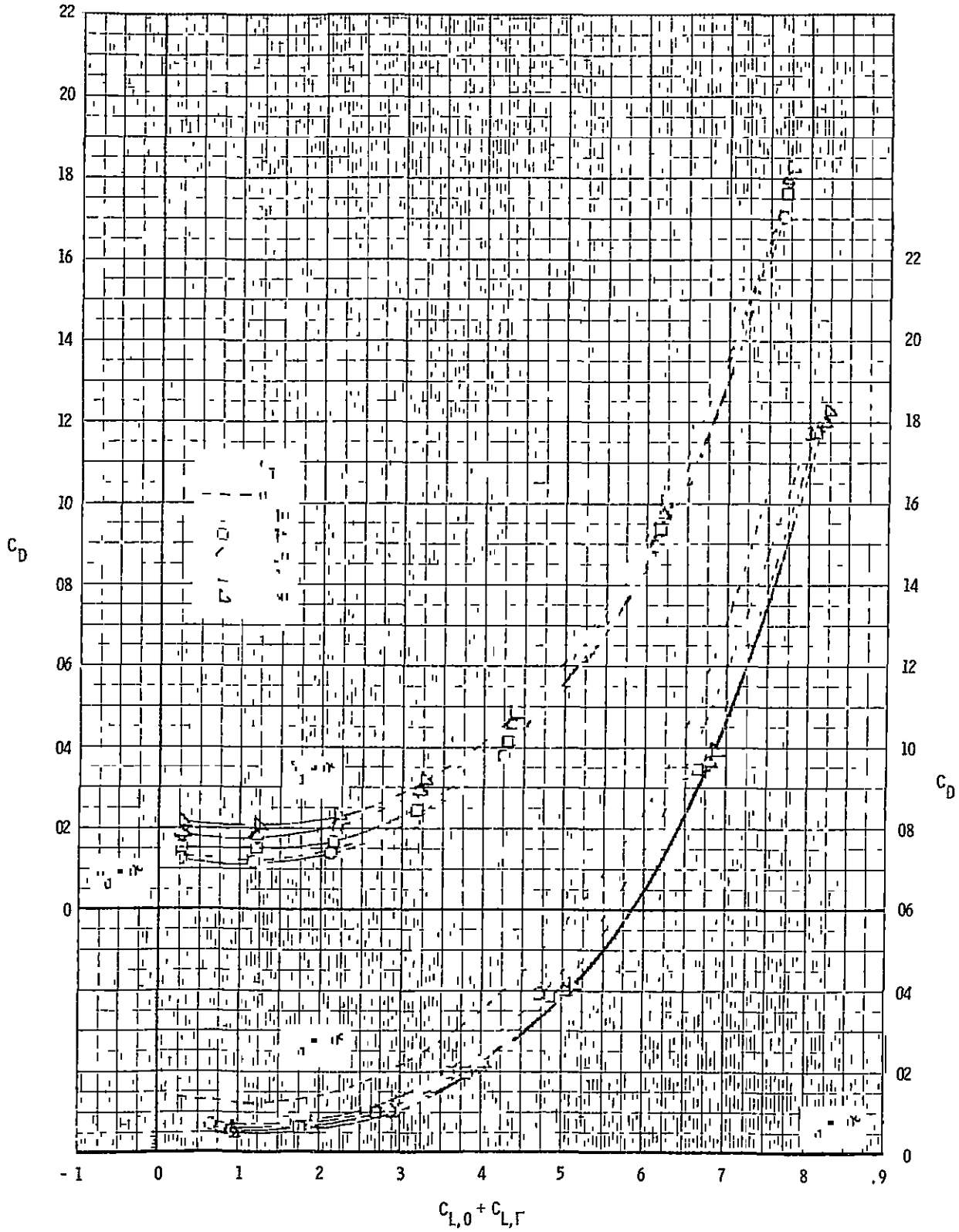

(a) M = 0 40

Figure 21. - Variation of drag coefficient with jet-off lift plus induced lift at constant thrust coefficient

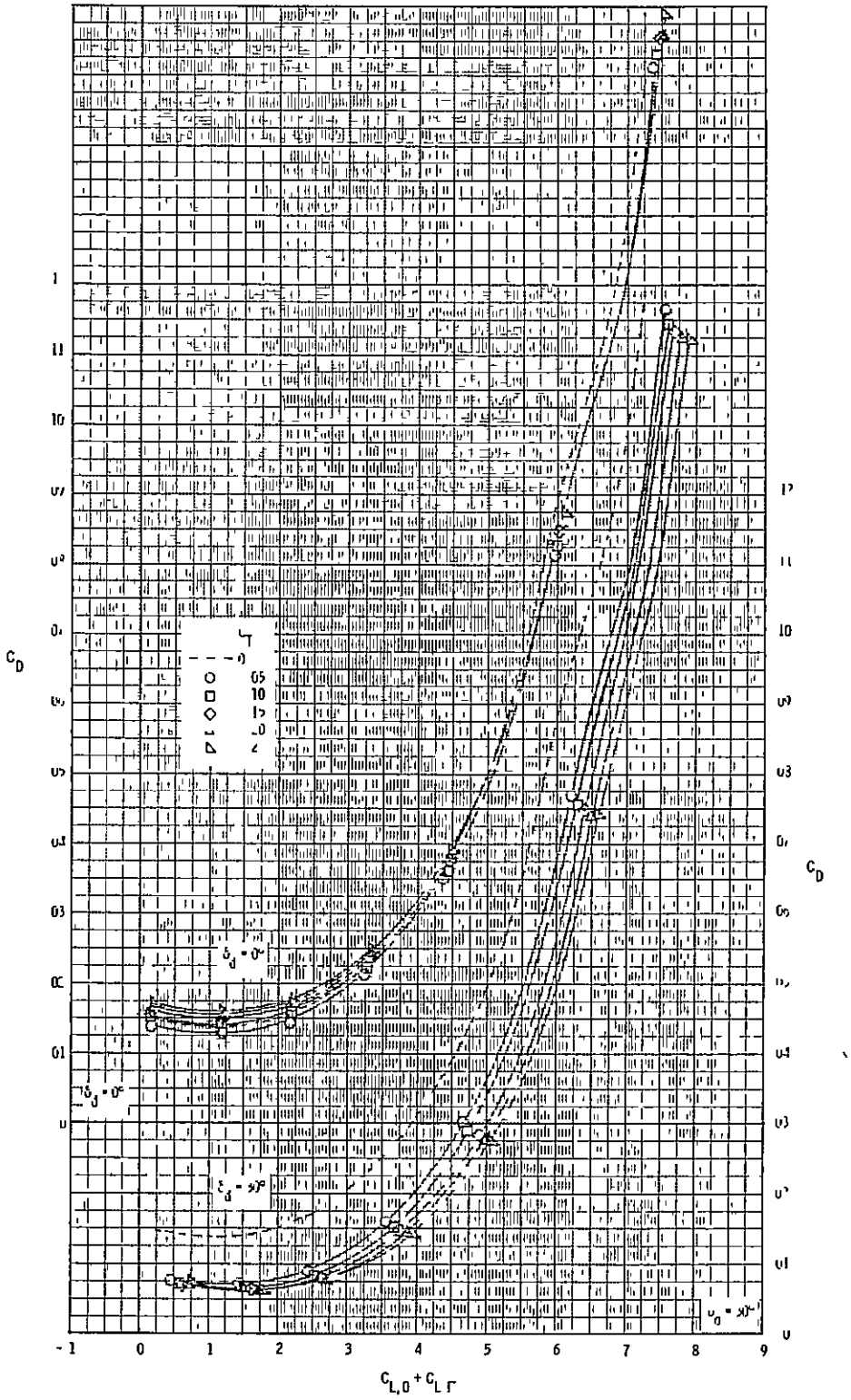

(b) M = 0.70
Figure 21 - Continued

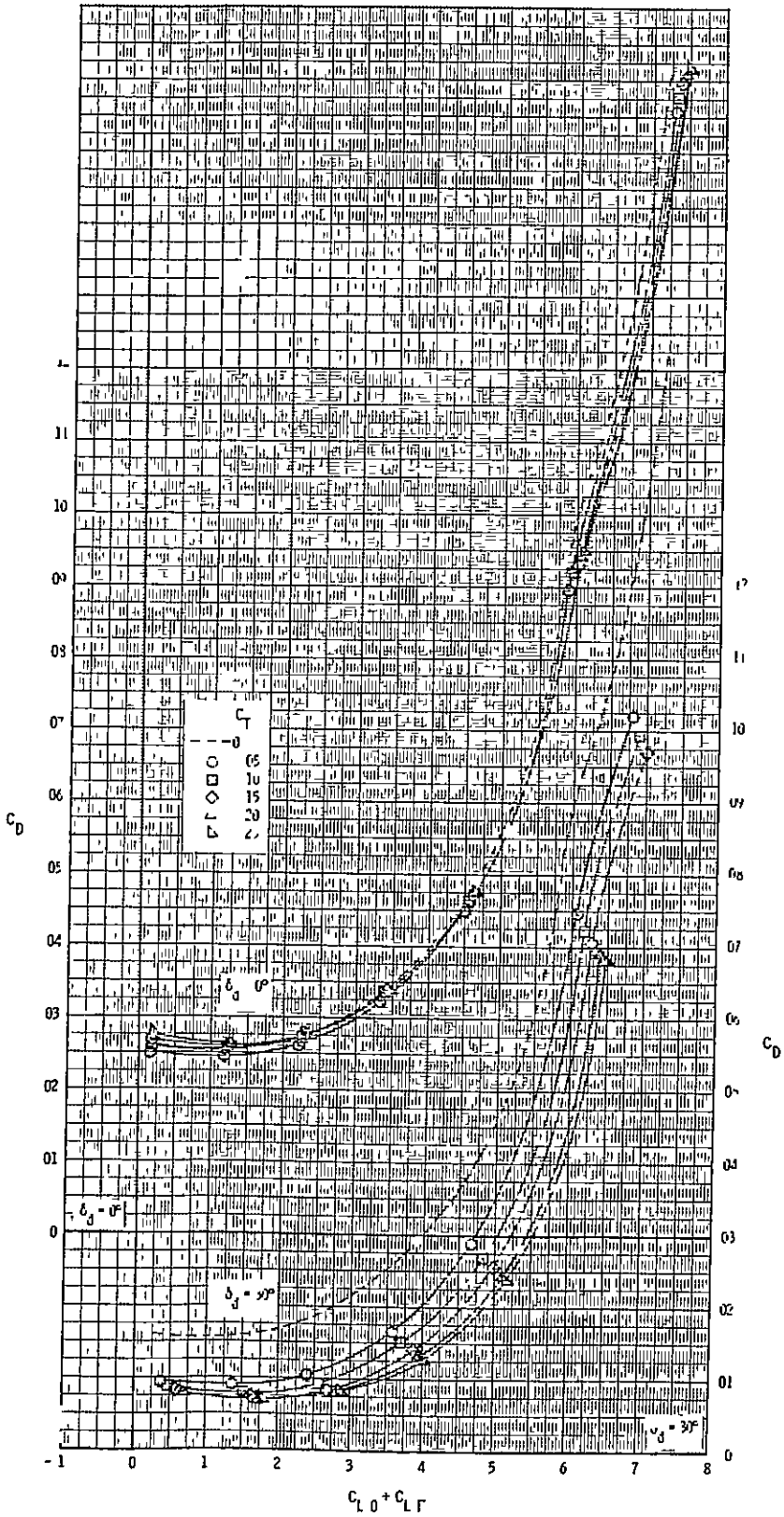

(c) M = 0.80

Figure 21 - Continued

ORIGINAL PAGE IS
OF POOR QUALITY

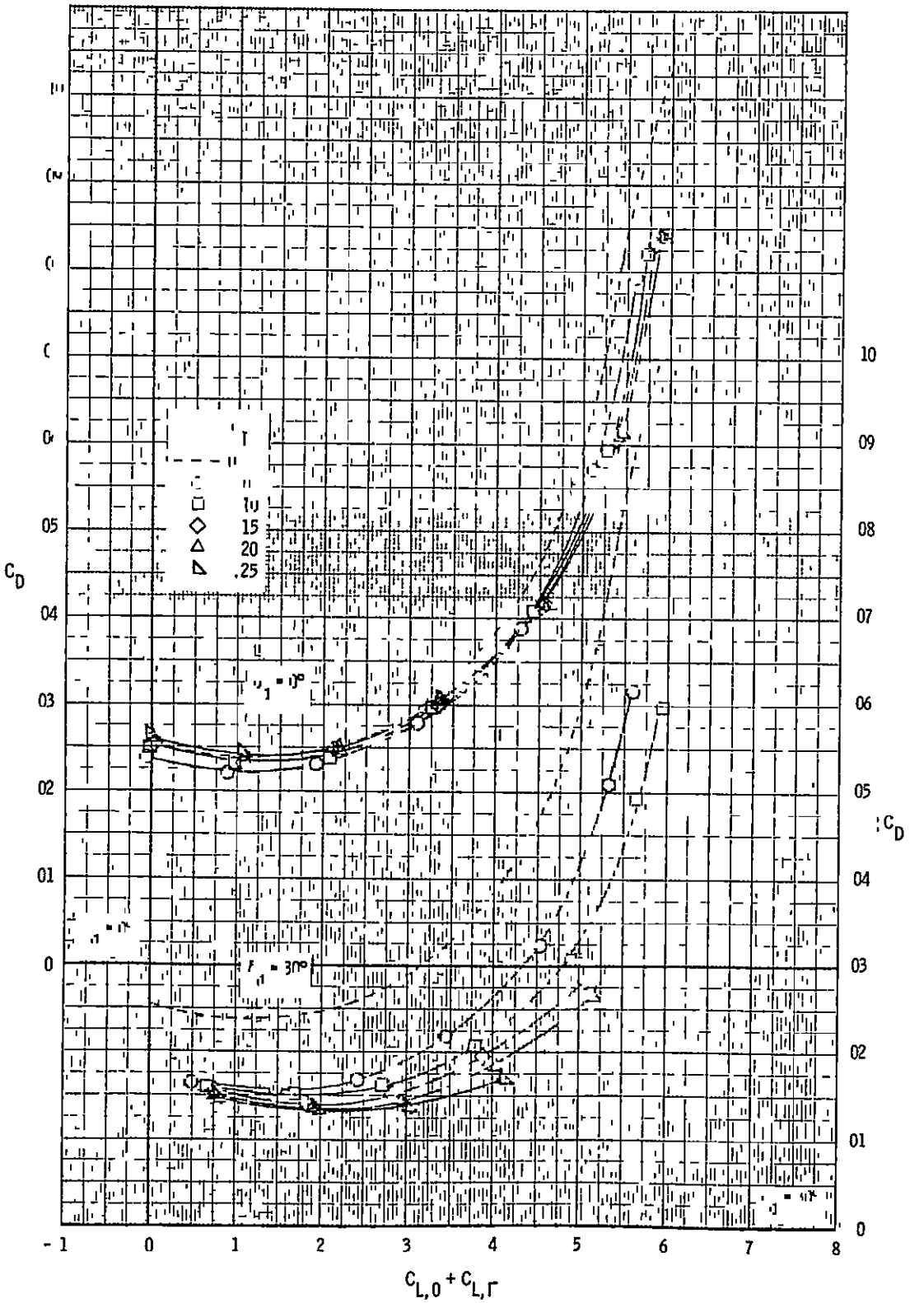

(d) M = 0.90.
Figure 21.- Continued.

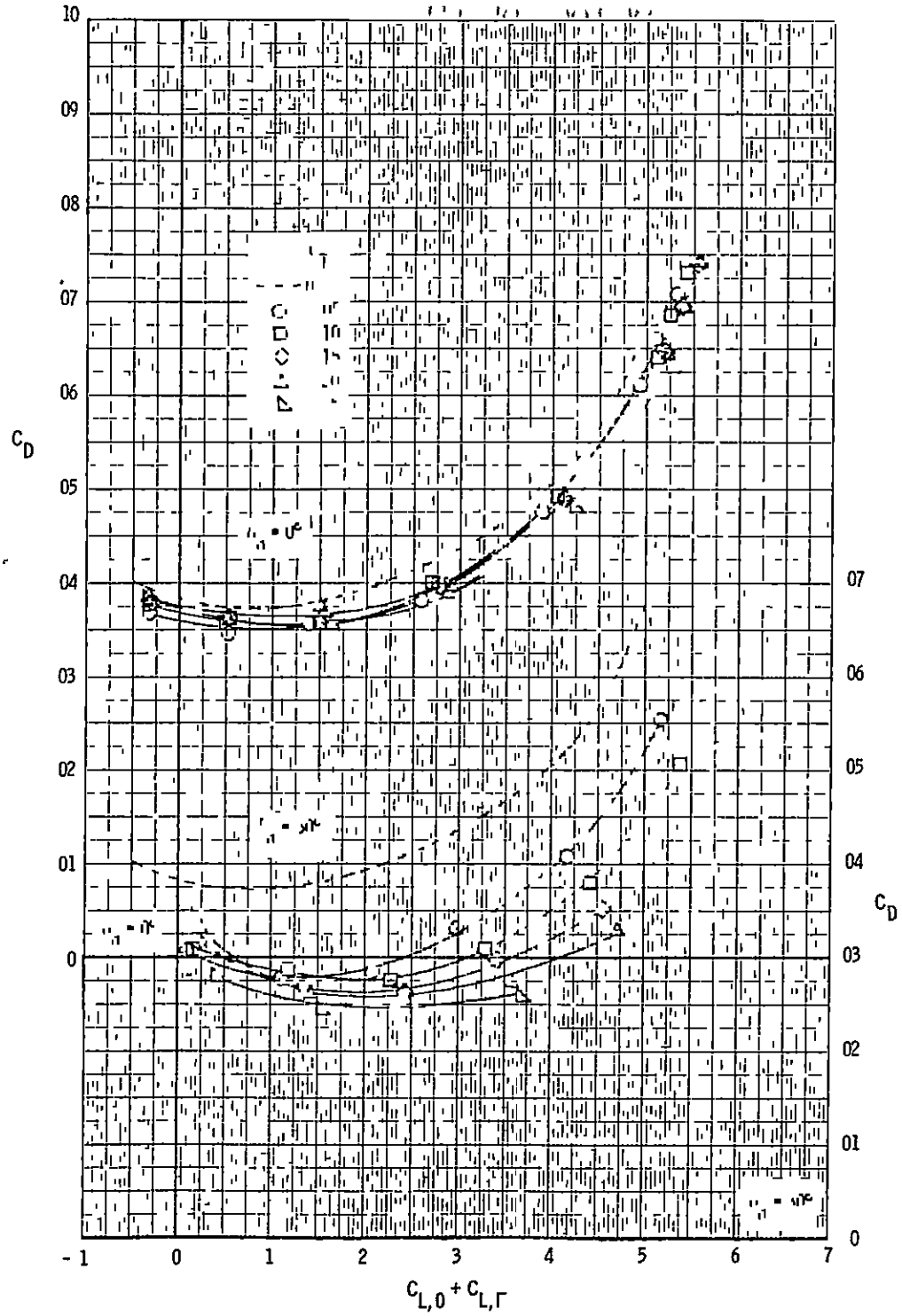

(e) M = 0 95

Figure 21. - Concluded

ORIGINAL PAGE IS
OF POOR QUALITY

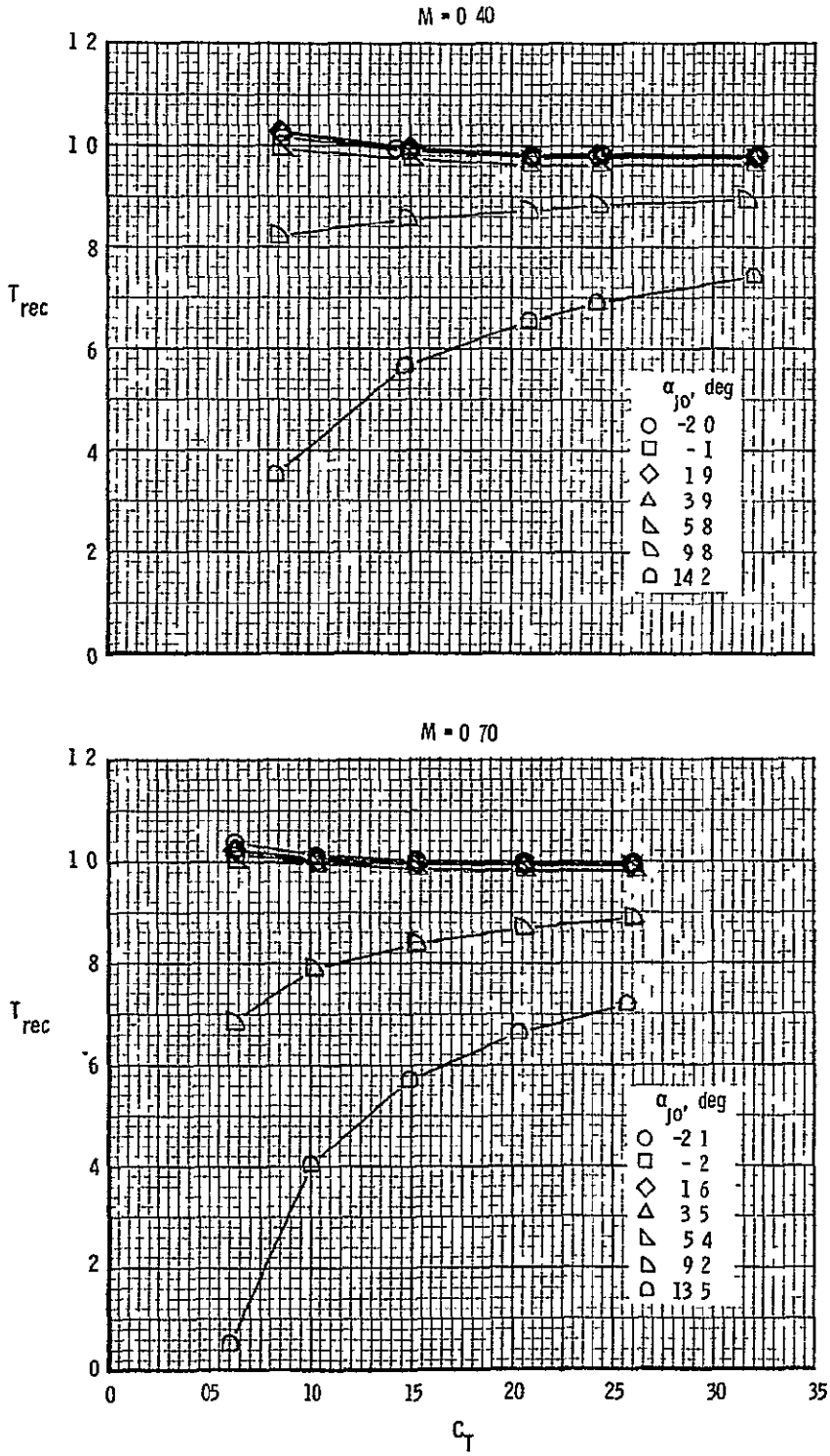

(a) M = 0 40 and 0 70

Figure 22. - Variation of thrust recovery with thrust coefficient, $\delta_d = 0°$

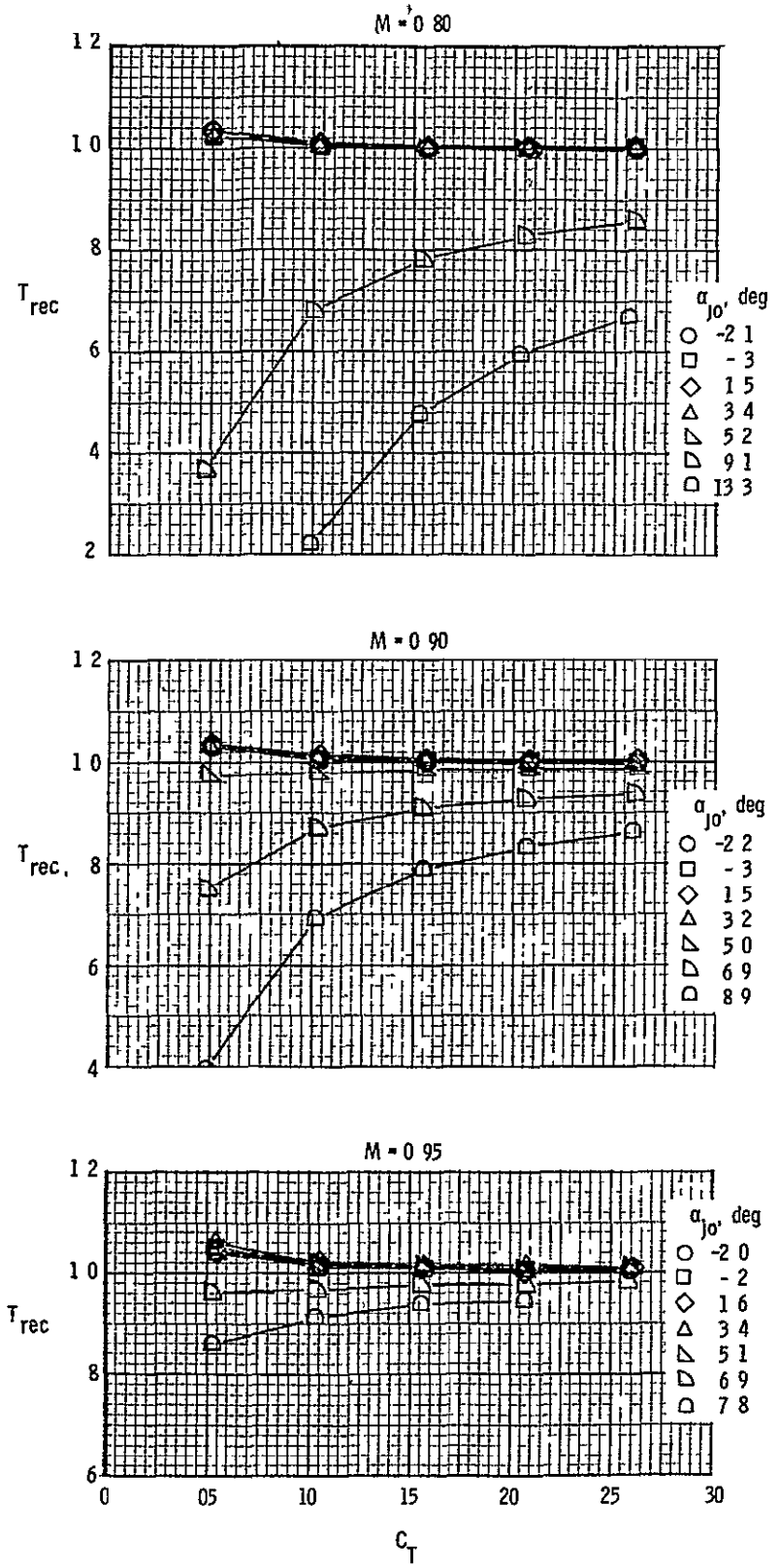

(b) M = 0 80 to 0 95
Figure 22 - Concluded

ORIGINAL PAGE IS
OF POOR QUALITY

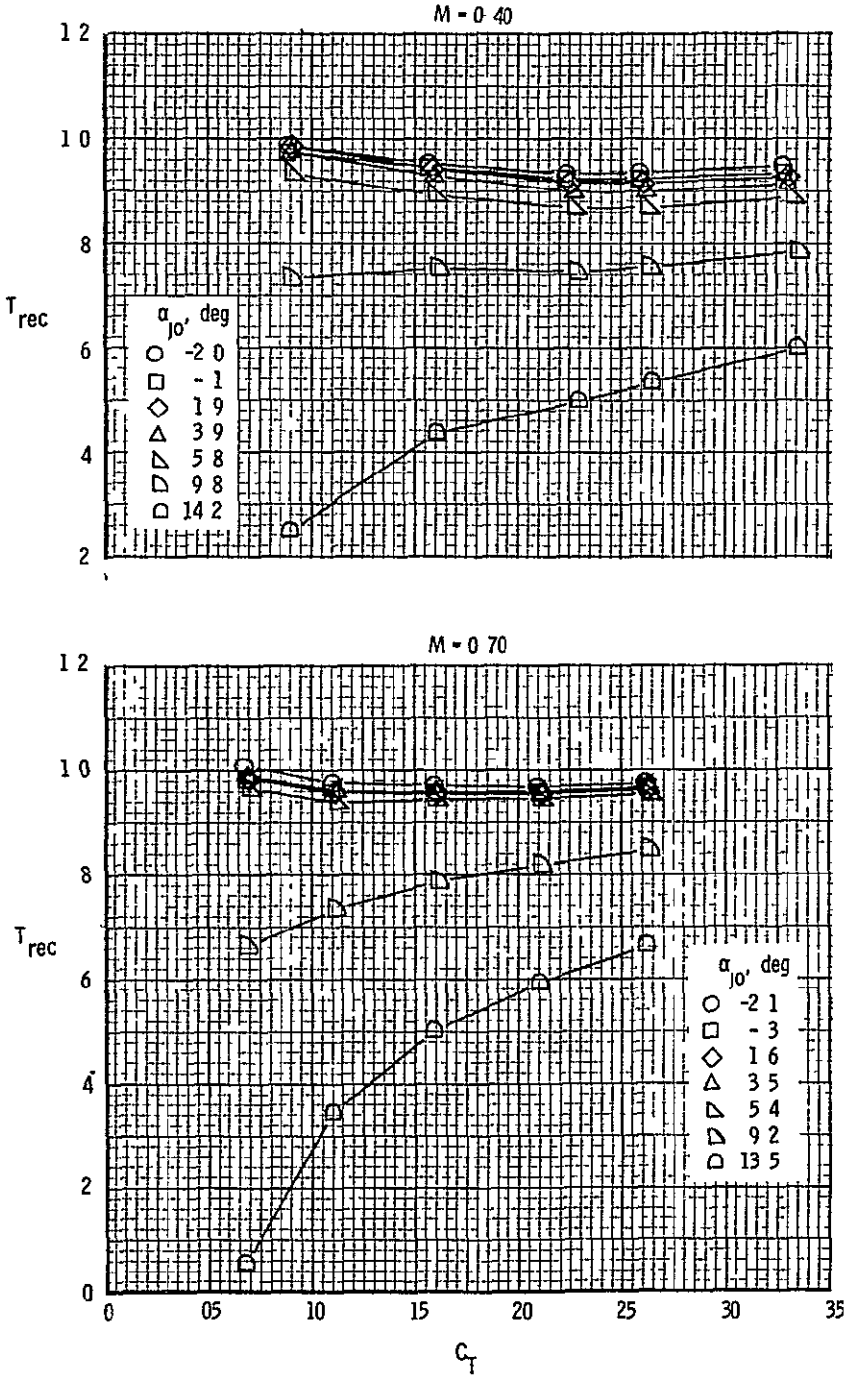

(a) M = 0 40 and 0,70

Figure 23 - Variation of thrust recovery with thrust coefficient, $\delta_d = 30°$

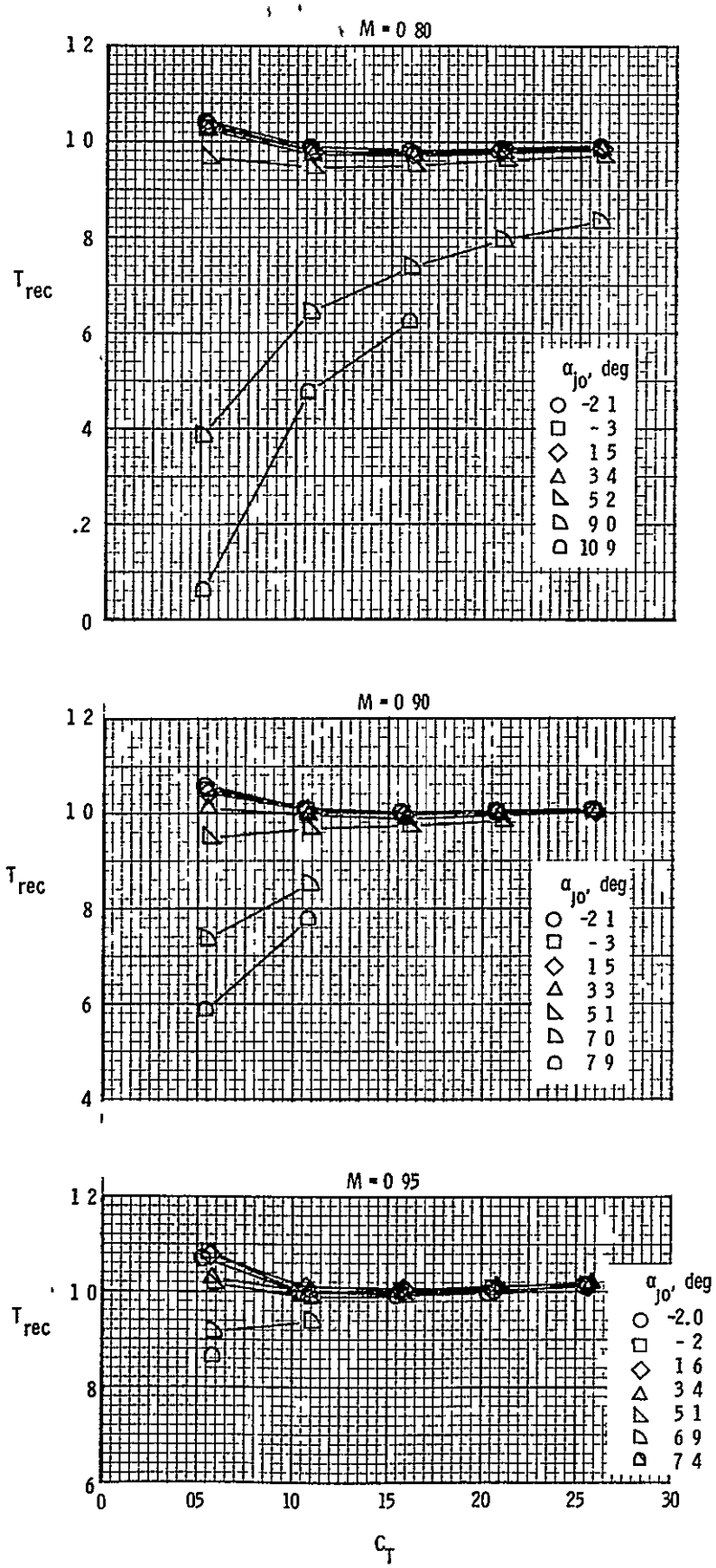

(b) M = 0 80 to 0 95
Figure 23 - Concluded

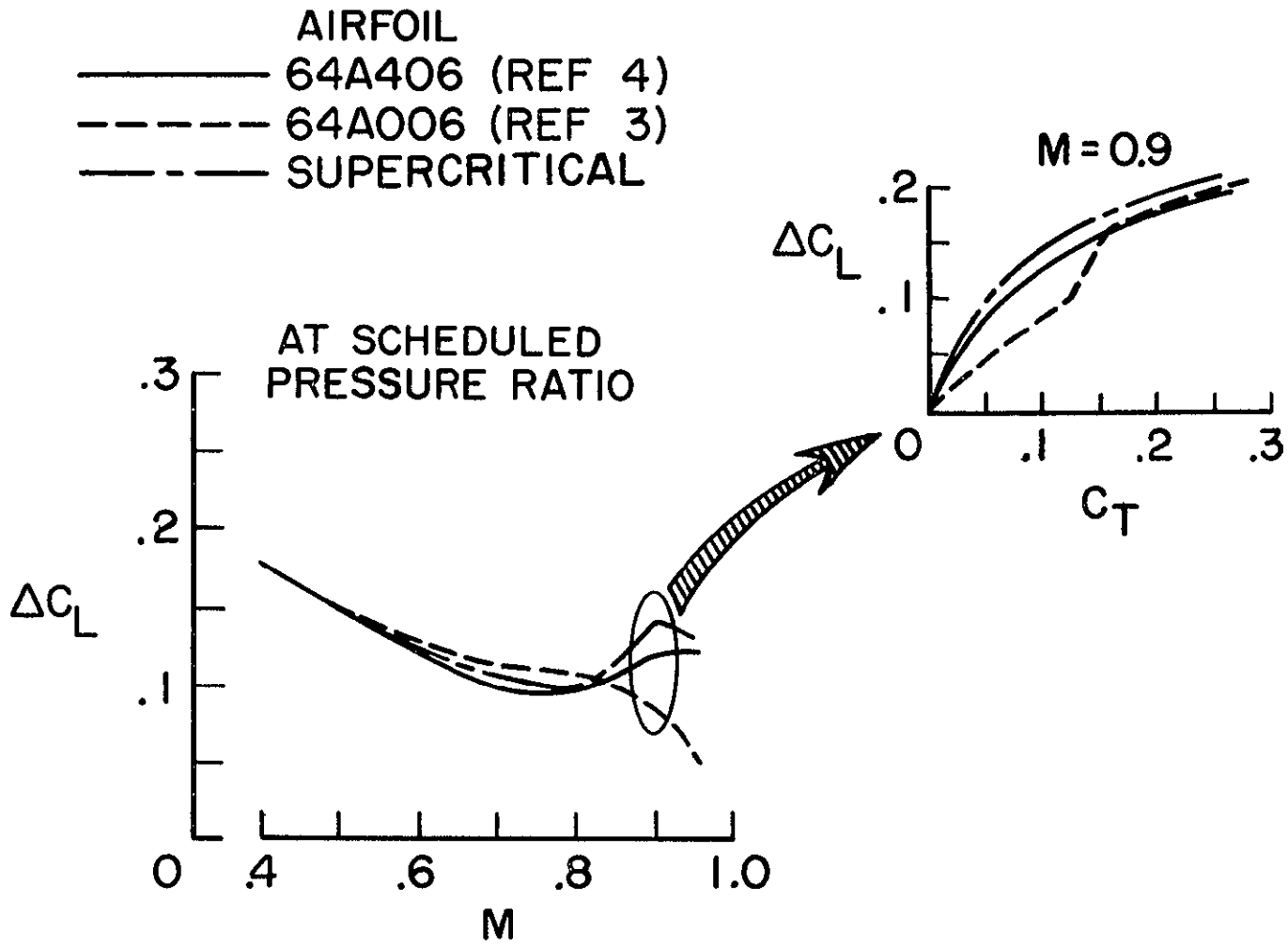

Figure 24.- Effect of airfoil variation on incremental lift, $\delta_d = 30°$, $\alpha = 0°$.

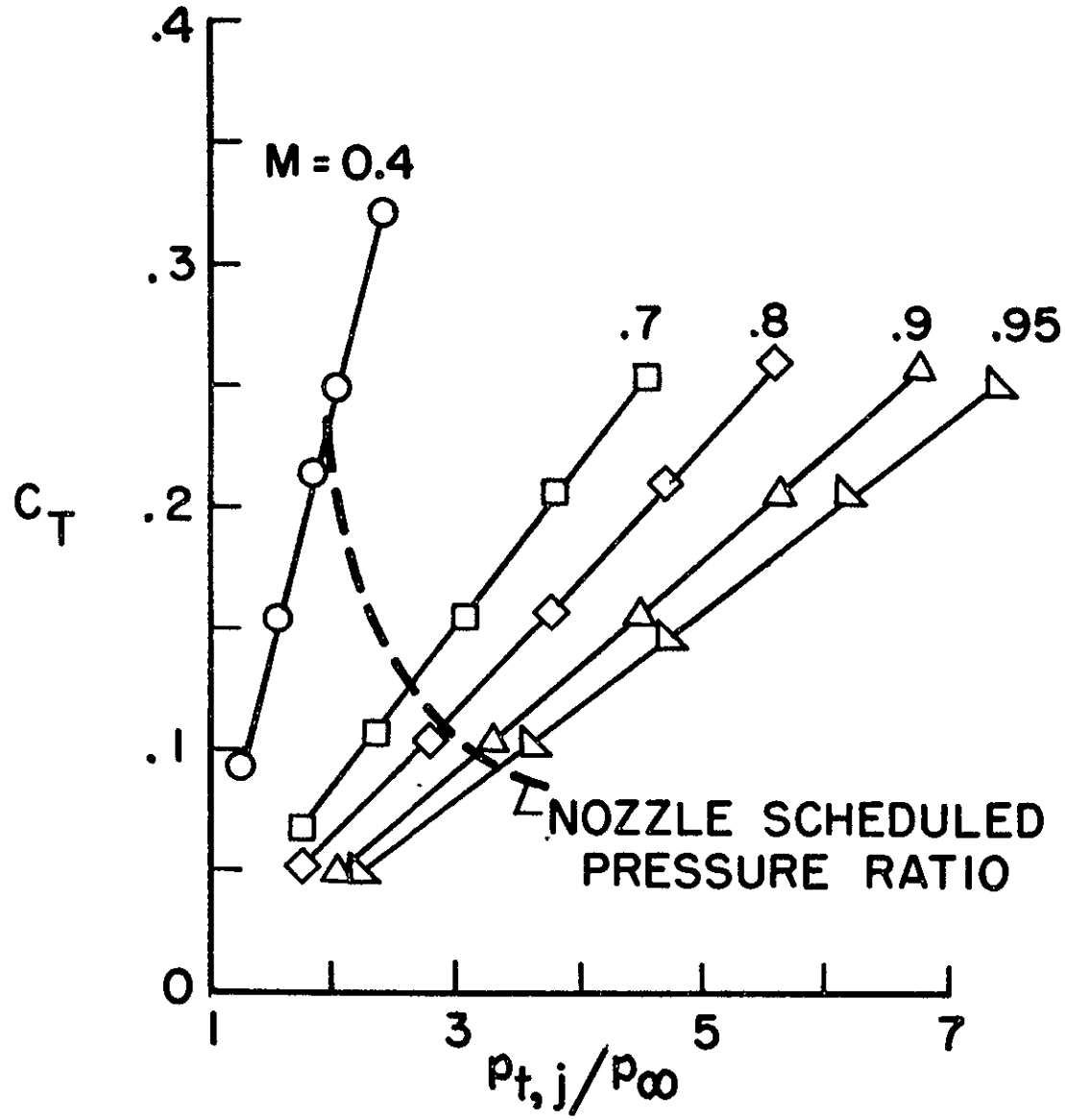

Figure 25.-Variation of gross thrust coefficient with nozzle pressure ratio.

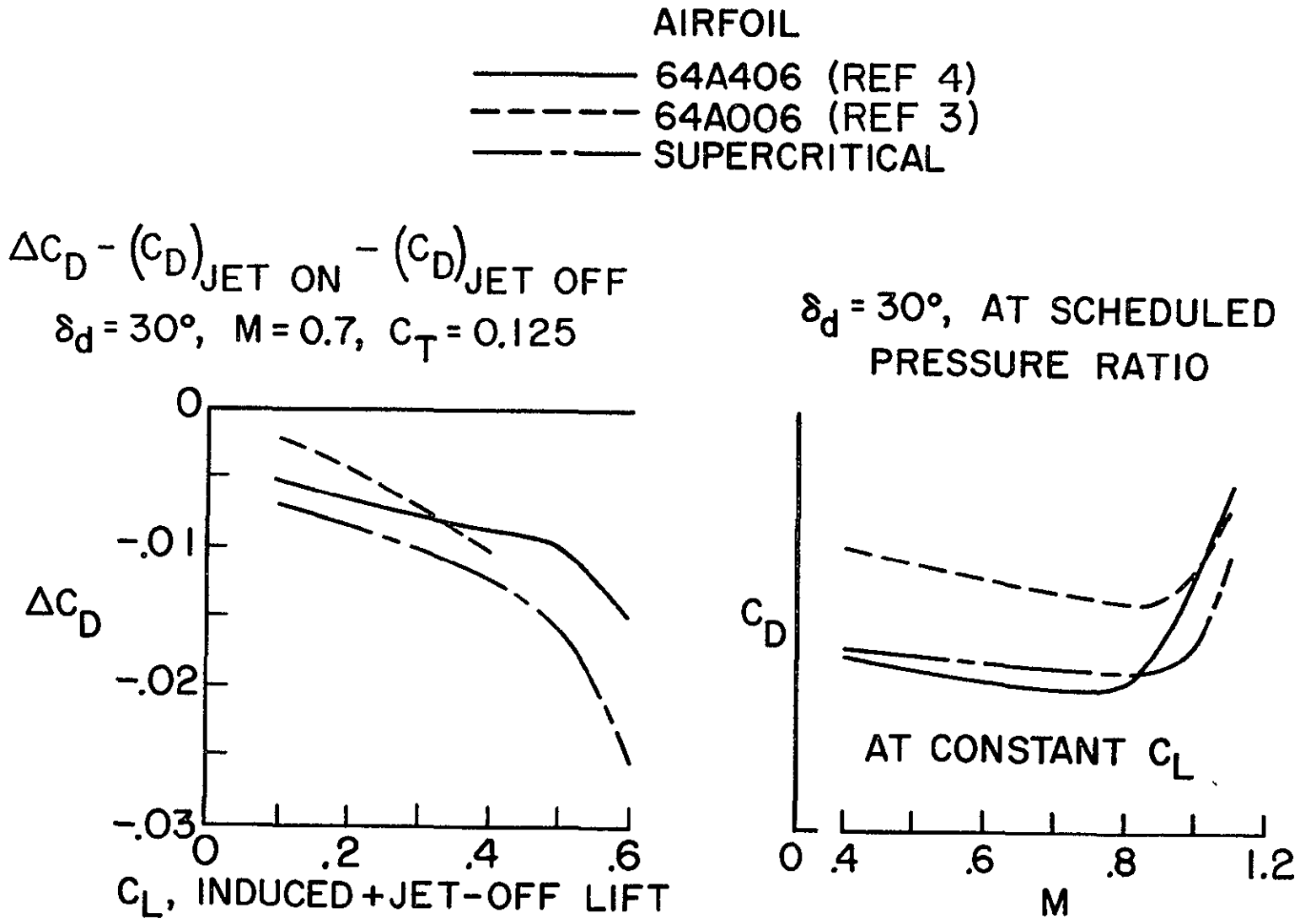

Figure 26. - Effect of airfoil variation on drag.

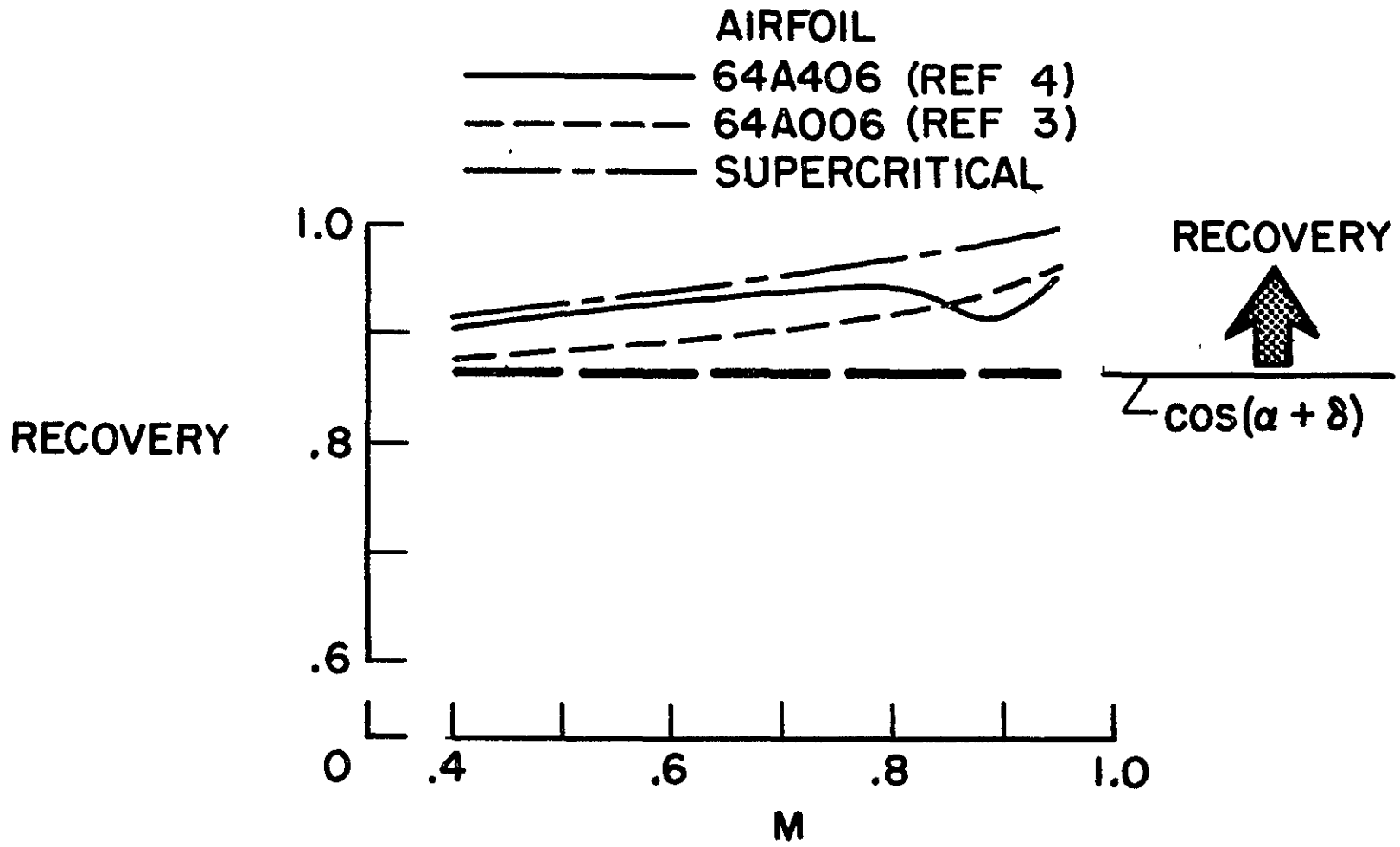

Figure 27.- Effect of Mach number and airfoil variation on thrust recovery, $\delta_d = 30°$, $(\alpha+\delta) = 30°$, at scheduled pressure ratio.

1 Report No	2 Government Accession No	3 Recipient's Catalog No
NASA TM-78746		

4 Title and Subtitle	5 Report Date
AERODYNAMIC CHARACTERISTICS INDUCED ON A SUPERCRITICAL WING DUE TO VECTORING TWIN NOZZLES AT MACH NUMBERS FROM 0.40 TO 0.95	August 1978
	6 Performing Organization Code 3760
7 Author(s) FRANCIS J. CAPONE	8 Performing Organization Report No
9 Performing Organization Name and Address NASA Langley Research Center Hampton, Virginia 23665	10 Work Unit No 505-11-23-06
	11 Contract or Grant No
12 Sponsoring Agency Name and Address National Aeronautics and Space Administration Washington, DC 20546	13 Type of Report and Period Covered Technical Memorandum
	14 Sponsoring Agency Code

15 Supplementary Notes

16 Abstract

An investigation has been conducted in the Langley 16-foot transonic tunnel to determine the induced lift characteristics of a vectored-thrust concept in which jet-exhaust nozzles were located in the fuselage at the wing trailing edge. The wing had a supercritical airfoil section. The investigation was conducted at Mach numbers from 0.4 to 0.95, angles of attack up to 14°, and thrust coefficients up to 0.35, and nozzle deflection angles of 0° and 30°. Separate force balances were used to determine both total aerodynamic and thrust forces and thrust forces alone which allowed for a direct measurement of jet turning angle at forward speeds. The Reynolds number per meter varied from 8.20×10^{6} to 12.80×10^{6}.

The results of this investigation show the configuration with the supercritical wing to generally have better performance with respect to both lift augmentation and drag reduction than the same configuration with a 64 series airfoil.

17 Key Words (Suggested by Author(s))	18 Distribution Statement
Vectored thrust Induced lift Supercritical airfoil Rectangular nozzle	Subject Category - 02 Unclassified - Unlimited

19 Security Classif (of this report)	20 Security Classif (of this page)	21 No of Pages	22 Price*
Unclassified	Unclassified	114	$6.50

* For sale by the National Technical Information Service Springfield Virginia 22161